NOVA SCHOOL OF SCIENCE & TECHNOLOGY

DEPARTMENT OF PHYSICS

DUARTE ANTÓNIO DO ESPÍRITO SANTO BERNARDO

Bachelor of Science in Biomedical Engineering

CHARACTERIZATION OF STRUCTURAL CHANGES IN SPINAL VERTEBRAE BASED ON PERTURBATIONS TO AN ADAPTIVE MODEL

MASTER IN BIOMEDICAL ENGINEERING

NOVA University Lisbon
September, 2022

NOVA SCHOOL OF SCIENCE & TECHNOLOGY

DEPARTMENT OF PHYSICS

CHARACTERIZATION OF STRUCTURAL CHANGES IN SPINAL VERTEBRAE BASED ON PERTURBATIONS TO AN ADAPTIVE MODEL

DUARTE ANTÓNIO DO ESPÍRITO SANTO BERNARDO

Bachelor of Science in Biomedical Engineering

Adviser: Prof.Dr.Ricardo Nuno Vigário
Associate Professor, FCT-UNL

Co-adviser: Prof.Dr.Ana Rodrigues
Associate Professor. FCM-UNL

Examination Committee

Chair: Prof.Dr.Hugo Gamboa
Associate Professor, FCT-UNL

Rapporteur: Prof.Dr.Ana Teresa Gabriel
Invited Assistant Professor, FCT-UNL

Member: Prof.Dr.Ricardo Vigário
Associate Professor, FCT-UNL

MASTER IN BIOMEDICAL ENGINEERING

NOVA University Lisbon
September, 2022

Characterization of structural changes in spinal vertebrae based on perturbations to an adaptive model

This document was created with the (pdf/Xe/Lua)LaTeX processor and the NOVAthesis template (v6.10.5) [1].

Acknowledgements

Firstly, I would like to say thanks to the professors who helped me during this six months of hard work:Profº Ricardo Vigário, Profª Ana Rodrigues, Profº Carla Quintão, Profº Cláudia Quaresma. Their insight and help was very important for this work to be concluded.

Secondly, I would like to say thanks to my family who always stood there to support me during the good and,specially, the bad times. Without them, this work and this degree would not be possible. Specially, I would like to highlight the role of my mother who always wanted me to get a degree and always worked hard so that I could achieved it.

Lastly, I would like to say thanks to all my colleagues and friends who, during this five years, supported and helped me whenever I needed. Their help was very important to overcome the challenges of this course.

"There are no secrets to success.It is the result of preparation, hard work and learning from failure."
(Colin Powel)

Abstract

Diffuse Idiopathic Skeletal Hyperostosis, or DISH, is a disease characterized by ossification of the entheses and the anterior longitudinal ligament. The diagnosis is made by visual analysis of an X-ray by a professional using the Resnick Criterion. The different experience among professionals and the fact that this criterion is only suitable in advanced stages of the disease make diagnosis difficult. Therefore, this work aims to contribute to the development of an auxiliary diagnostic tool for this disease.

For this, a semi-automatic vertebral segmentation algorithm based on active morphological contours was proposed, comparing it with previous work and with segmentations made by experts on two radiographic images. Next, the corners of the vertebrae, where the disease manifests itself, were analyzed in order to characterize images with DISH. To accomplish this, it was assumed symmetry of the vertebrae and a Gaussian distribution of the histograms of those corners to analyze them and calculate two ratios: Left upper corner mean value / Right upper corner mean value (LS/RS) and Left lower corner mean value / Right lower corner mean value (LI/RI), in order to find a differentiating metric between vertebrae with pathology and those without.

The results achieved by the algorithm were clearly superior to the previous work and similar to that of the experts. The analysis of pathologic vertebrae revealed a difference in the shift of the distributions of pathologic corners relative to non-pathologic ones, which is not seen in vertebrae without apparent pathology. Regarding the ratios, the LI/RI proved to be particularly effective in differentiating, being closer to 1 when pathology is not present.

Keywords: DISH, X-ray, Image processing, Segmentation, Morphological Active contours

Resumo

A Hiperostose Esquelética Idiopática Difusa, ou DISH, é uma doença caracterizada pela ossificação das entéses e do ligamento longitudinal anterior. O diagnóstico é realizado pela análise visual de um raio-X, por um profissional, utilizando o Critério de Resnick. A diferente experiência entre profissionais e o facto de este critério só ser adequado em fases avançadas da doença tornam o diagnóstico difícil. Por isso, este trabalho visa contribuir para o desenvolvimento de um instrumento auxiliar de diagnóstico desta doença.

Para isso, foi proposto um algoritmo de segmentação de vertebras, semi-automático, baseado em contornos morfológicos ativos, comparando-o com o trabalho anterior e com as segmentações feitas por especialistas em duas imagens radiográficas. De seguida, foram analisadas as extremidades das vértebras, onde a doença se manifesta, com o objetivo de identificar imagens com DISH. Para tal, assumiu-se a simetria das vértebras e uma distribuição Gaussiana dos histogramas das extremidades para analisar as mesmas e calcular dois rácios: Valor médio do canto superior esquerdo / Valor médio do canto superior direito(LS/RS) e valor médio do canto inferior esquerdo /Valor médio do canto inferior direito(LI/RI), a fim de encontrar uma métrica diferenciadora das vértebras com patologia das não patológicas.

Os resultados conseguidos pelo algoritmo foram claramente superiores ao do trabalho anterior e semelhantes ao dos peritos. A análise das vértebras patológicas revelou uma diferença na deslocação das distribuições dos cantos patológicos relativamente aos não patológicos, o que não se verifica em vértebras sem patologia aparente. Relativamente aos rácios, o LI/RI mostrou ser particularmente eficaz na diferenciação, estando mais próximo de 1 quando a patologia não está presente.

Palavras-chave: Hiperostose Esquelética Idiopática Difusa, Raios-X, Processamento de Imagem, Segmentação, Contornos Ativos Morfológicos

Contents

List of Figures

List of Tables

Acronyms

AAL Anterior Longitudinal Ligament *(p. 10)*
AS Ankylosis Spondylitis *(p. 3)*

CT Computed Tomography *(pp. 3, 12)*

DC Dice Coefficient *(p. 38)*
DISH Diffuse Idiopathic Skeletal Hyperostosis *(p. 1)*

GVF Gradient Vector Flow *(p. 31)*

HD Hausdorff Distance *(p. 38)*

LI Left inferior corner average intensity value *(p. 55)*
LS Left superior corner average intensity value *(p. 55)*

MRI Magnetic Ressonance Imaging *(pp. 3, 12)*

PDE Partial Differential Equations *(p. 35)*

RI Right inferior corner average intensity value *(p. 55)*
RS Right superior corner average intensity value *(p. 55)*

1

Introduction

This chapter provides a brief description of the motivation and context this work. Also, the objectives and questions to be answered are described here.

1.1 Motivation

Diffuse Idiopathic Skeletal Hyperostosis (DISH) is a non-inflammatory and systemic disease, which is characterized by a continuous bone formation on ligaments and entheses, which are the connective tissues between the tendons or ligaments and the bone.

The disease can appear in the cervical, thoracic and lumbar spine, but normally manifests in the thoracic section. Also, it frequently manifests as flowing mantles of ossifications in the anterior longitudinal ligament [2]. According to [3], the ossifications in the thoracic spine are usually found on the right side of spine and it is thought that this occurs due to the protective function provided by the arterial distribution, such as the descending aorta. Beyond this structures, the ossifications can be present in the ligaments connecting the laminae, in the spinal and transverse processes. Also, the posterior longitudinal ligament can also be proned to this disease, specially in the cervical spine [2]. Figure 1.1 shows an example of a sagitall X-ray image of the spine ,showing, with white arrows, the ossification of the anterior longitudinal ligament.

As consequence of this disease, there are some complications associated, such as: dysphagia or difficulty to swallow[5], vocal cord paresis[3], a rare complication of DISH, and airway obstruction[6]. Dysphagia can results of compression of esophagus by ossifications in the cervical spine[7]. Concerning the vocal cord paresis, a possible mechanism is the compression by ossification in the cervical spine of the laryngeal nerve, which innervate the vocal folds, and is responsible for production of sound [7]. The latter complication is caused by bone formation in cervical spine which can cause pressure over the trachea, deviating it from the normal position, and limiting the air flow[8]. A Sagitall X-ray of the spine of a patient with DISH and dysphagia(Left image) and a Sagitall X-ray of the Spine of another patient without DISH(Right image) can be seen in Figure 1.2. In both images, the blue curves and the white arrows point to the vertebrae C4 and C5. In the left image,

Figure 1.1: Sagittal X-ray of the DISH spine showing,with white arrows,the thickening and ossification of anterior longitudinal ligament[4].

the ossifications (blue curve and white arrow) present anteriorly to the vertebrae can cause pressure on the esophagus, limiting the swallowing process. In the right image, there is no presence of ossifications and, therefore, are not limiting the swallowing process.

Other complications, such as restrictive lung disease, can occur when this disease is present in sternocostal or chondrocostal junctions, which may reduce the thorax movement. Also, in end-stage DISH subjects, this disease can lead to a vulnerable spine and make it fracture, even for low-level load trauma[10].

Beyond this complications, DISH has been associated with other diseases, such as cardiovascular diseases[11] and metabolic derangements[12].

There are three major diagnosing criteria to evaluate this disease. The criteria created by Resnick and Niwayama states that the ossifications must encompass at least four contiguous vertebrae and do not involve degenerative changes in the intervertebral discs or apophyseal and sacroiliac joints[8]. Julkunen *et al*.[13] created a criteria which only differs from Resnick and Niwayama's in the fact that they include bridged connecting two vertebral bodies in at least two sites of the thoracic spine. Utsinger *et al*.[14] considered that three contiguous vertebral bodies and the presence of peripheral enthesopathies were only necessary to diagnose DISH[15].

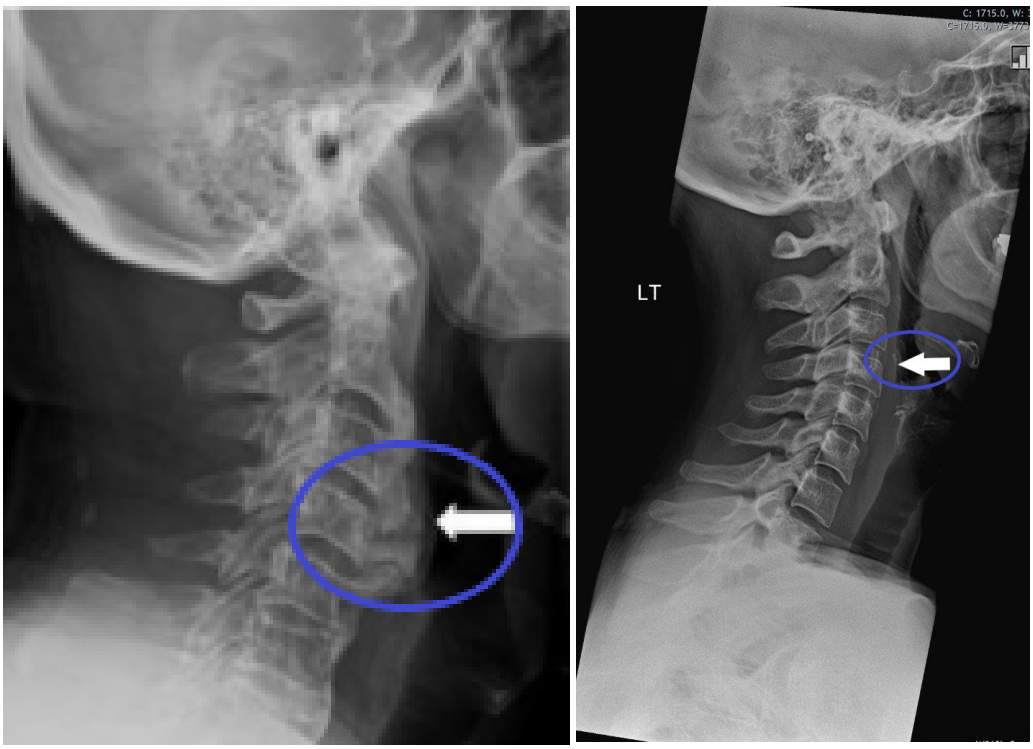

Figure 1.2: Two Sagittal X-rays of the spine of two different patients. (Left image): Patient with DISH and dysphagia showing, with white arrows and the blue curve, the ossifications in the cervical spine [Adapted from[4]]. (Right image): Non-DISH patient showing, with white arrows and the blue curve, that there are no ossifications [Adapted from[9]].

The diagnosis of this disease is mainly through imaging, specially radiography. This technique is more frequently used due to economic issues and usually anterior-posterior and lateral spine radiographs are recommended[16]. Moreover, Computed Tomography (CT) and Magnetic Ressonance Imaging (MRI) can also be used. Both imaging modalities have higher resolution than X-ray and provide a three dimensional visualization of structures and are good to detect spinal injuries. Also, both can be used to evaluate the extent of ossifications in the cervical spine and their impact on the esophagus[17]. These imaging modalities can, as well, be useful in differentiating this disease from Ankylosis Spondylitis (AS). AS, on contrary to DISH, usually affects the facet joints, which are connections between adjacent vertebrae, and CT can be useful in identifying changes in these structures. MRI, on the other hand, can provide insight into inflammatory changes[10], which are present in AS and not in DISH.

However, the diagnosis of the disease is rather difficult, requiring careful examination of images by expert professionals. These professionals have different experiences, thus, there is a high chance of variability of diagnoses[18]. Also, according to [19], in contrary to other spine injuries, DISH diagnosis is very delayed and the reason behind this fact is that pre-existent abnormalities on the radiographs may mask small fractures. In [20], it is stated that the criteria proposed by Resnick, Julkunen and Ustinger are only visible, and mostly applicable, 10 to 15 years after the onset of the disease, limiting their use.

Thus, an early recognition of this disease is very desirable, in order to allow for a better management of metabolic diseases associated with DISH with the goal of reducing the progress rate of the disease[2].

1.2 Contextualization

As stated earlier, DISH is usually diagnosed through analysis of X-ray images by professionals. Some limitations of these analysis are the possible misevalutations due to the intervariability between professionals. Therefore, an automatic and reproducible diagnosis of DISH would be of utmost importance nowadays. Some works have been proposed to achieve these automatic diagnostic tools, such as [21] and [18]. In 2019, Lopes [21] developed a semi-automatic segmentation pipeline for X-ray images of healthy individuals, with the ultimate goal of being applied to DISH patients. The results were satisfactory, although some limitations regarding the vertebrae segmentation persisted. In 2021, Viegas [18] proposed an algorithmic approach to develop generic model of spinal vertebral bodies using manual segmentations made by experts. The results showed that segmentation was effective on non-pathological X-ray images. Nevertheless, and a function of the generality of the obtained models, each vertebra presented abnormally smooth edges.

The present work fits in the context of the aforementioned works and builds on them, in particular [18], to achieve individualized vertebra segmentation, as well as an automatic tool for the diagnosis of DISH.

1.3 Objetives

In a general way, this work aims to contribute to the development of an accurate diagnostic tool for physicians and doctors to analyse DISH patients.

In a particular way, this work has two main goals: Firstly, since this work follows the work made by [18], it aims to show that the algorithm proposed here is better in evaluating the specific morphology of each vertebra. Secondly, this work aims mainly to build a patient-specific segmentation of vertebrae and, then, develop tools to characterize deformations on vertebral bodies in the spine, based on X-ray images caused by DISH. To do so, this work aims to provide a vertebrae segmentation algorithm and evaluating the differences between pathological vertebrae from non-pathological in X-ray images.

1.4 Questions to be answered in this work

The general questions aimed to be answered in the present work are the following:

1. Does this algorithm outperforms the segmentation performance of Viegas [18]?

2. Is the segmentation performance of this algorithm similar to the performance of experts in the area?

3. Are left-right discrepancies in x-ray intensities usable to distinguish pathological vertebrae from non-pathological ones?

4. Is there a difference between the histograms distributions of pathological corners and non pathological corners?

5. Is there a criteria based on intensity values able to diagnose DISH?

1.5 Structure of the Document

This document is organized in eight chapters and three annexes. The first chapter is the Introduction and it describes the work's motivation and contextualization as well as the its objetives and research questions. In the second chapter, important theoretical concepts needed to understand the current work and the literature review made on DISH assessment methods, automatic and diagnosing tools of spinal diseases are presented. The third chapter is dedicated to image processing concepts, including noise removal and contrast enhancement techniques and, specially, segmentation algorithms. The fourth chapter describes the material and the methodology applied in the work. The fifth chapter presents the results of segmentation evaluation as well as the discussion of them. In the sixth chapter, the results of the segmentation of vertebrae segmentations and their analysis, for DISH evaluation, are presented. The seventh chapter discusses the results described in the previous chapter. Finally, the eighth chapter summarizes the conclusions achieved by this work and also describes its limitations. Some proposals for future work are also mentioned here.

Concerning the annexes, the first one describes the size of each image used for the segmentation and analysis of vertebrae. The second annex shows the professionals' annotations used for the segmentation evaluation described in chapter five. The third annex shows the remainder of segmentations and the correspondent analysis for each image used for the DISH evaluation.

2

Theoretical Concepts

This chapter presents some theoretical concepts to contextualize the proposed work. First, a brief review of the anatomy of the spine, with a particular attention to the morphology of the vertebrae. Then, a brief description of the most used imaging modality for Spine: X-ray. After this, a description of DISH and its consequences on the spine health is made. Finally, a literature review of the works that have been done in order to contribute to the improvement of DISH and AS diagnosis is shown.

2.1 Anatomy of the Spine

The spine is a bone structure that comprises 33 vertebrae. It starts at the end of the skull and extends to the pelvis. In this anatomical structure, there are five sections and each one has a specific number of vertebrae. Also, the normal spine has three curves: the cervical curve is called lordosis, the thoracic curve is called kyphosis and the lumbar curve is called lordosis. These curves are important for balance and help one to stand up. As shown in Figure 2.1, the spine can be seen through different views: Anterior, Lateral or Posterior. This is quite important for professionals because it helps them to assess the angles of the spine and deviations to the natural curves.

The following enumeration describes each section in terms of number of vertebrae and the name given to the correspondent natural curves:

1. Cervical-Seven vertebrae(C1-C7)-Lordosis ;
2. Thoracic- Twelve vertebrae(T1-T12)-Kyphosis;
3. Lumbar- Five vertebrae(L1-L5)-Lordosis;
4. Sacrum- Five vertebrae(S1-S5)-;
5. Coccyx- Four unified vertebrae.

The spinal column has many functions such as protection of the spinal cord and load-bearing, by withstanding external forces and providing support for flexible movement [22].

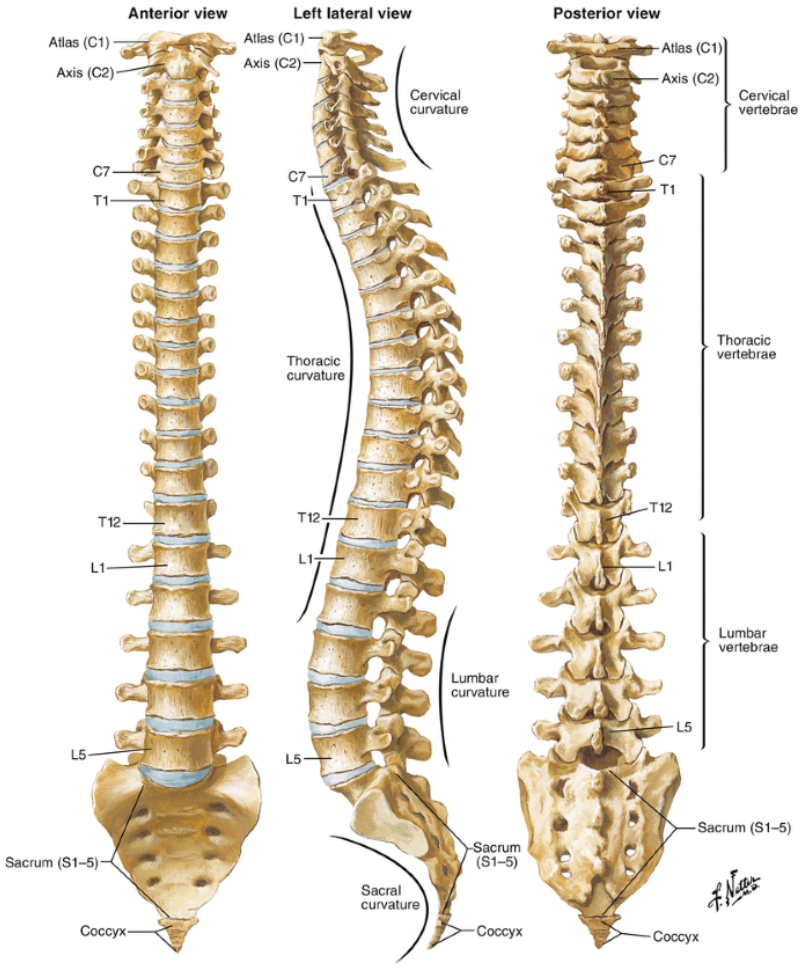

Figure 2.1: Different views of the spine and section division: Anterior View (Left), Left Lateral View (Middle), Posterior View (Right) [23].

2.1.1 Vertebrae

Vertebrae are structures with a basic morphology comprised by the anterior vertebral body and the posterior vertebral arch, as shown in Figure 2.2. Between these two areas, it is possible to find the *foramen*, which allows the spinal nerves and vessels to pass through the full length of the spine.

The anterior vertebral body is the load-bearing component and the size of this structure varies with the position in the collumn (bigger size in the lower sections) due to the need to cope with an increased weight load[24].

Concerning the posterior arch, this is constituted by various elements:

- Pedicles;
- Transverse processes;
- Laminae;
- Articular Processes;

- Spinous processes.

Pedicles connect the vertebral body to the transverse processes, which are two in each vertebra, projecting laterally and posteriorly. These structures connect the vertebral body to the transverse processes. The transverse processes are two in each vertebra and projected laterally and posteriorly. The laminae link the transverse processes to the spinous process and the articular processes link two consecutive vertebrae. Finally, spinous processes are bony proeminences where the two laminae of each vertebrae meet and act as the point where the muscles and ligaments of the spine attach to [25][24].

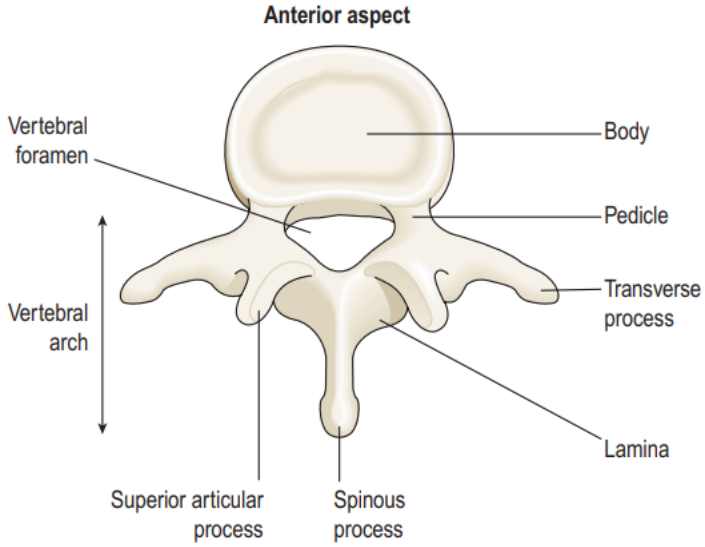

Figure 2.2: Superior view of a typical vertebra showing its basic morphology [26].

2.1.2 Intervertebral Disc

The inverterbral disk is a structure located between vertebrae in the cervical (except for C1 and C2), thoracic and lumbar sections. It has the function of preventing vertebrae from fracturing by reducing load and allow their movement, as well as permit nutrients to flow to the spine and spinal cord. Figure 2.3 shows a representation of an intervertebral disk.

Each intervertebral disk is composed of three components: the *nucleus pulposus*, the *annulus fibrosus* and the cartilaginous endplates, that anchor the discs to adjacent vertebrae. The *nucleus pulpusus* is located in the center of this structure and is gel-like. It is responsible for most of the flexibility and strength of the spine. The *annulus pulpusus* surrounds the *nucleus pulpusus*, and it is made of concentric collagen fibres. Each layer has a different orientation from the previous, conferring resistance in many directions. Lastly, the cartilaginous endplates cover either the superior or the inferior aspects of the intervertebral disk and are responsible for allowing the diffusion of nutrients and are the main source of nutrition in the disc[28].

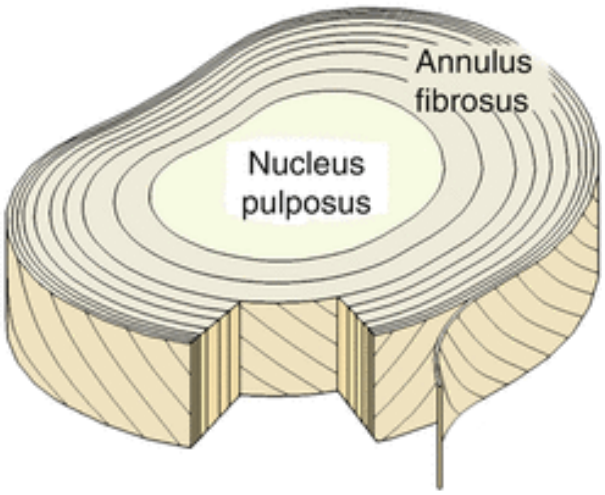

Figure 2.3: Representation of an intervertebral disc, indicating the *Nucleus Pulpusus* and *Annulus Fibrosus*[27].

2.1.3 Spinal ligaments

Spine is also composed of ligaments, which are fibrous band. They act as stabilizers of the the spine and protectors of the discs. Figure 2.4 shows the ligaments present in the spine, with a particular attention to three ligaments (green curves): the *ligamentum flavum*, the Anterior Longitudinal Ligament (AAL); and the Posterior Longitudinal ligament [29]. These are the major ligaments in the spine because contribute the most for its stabilization. The *ligamentum flavum* connects the laminae of adjacent vertebrae and the AAL covers the anterior part of the vertebrae throughout the spine. The Posterior Longitudinal ligament is located inside the spinal canal, throughout the spine.

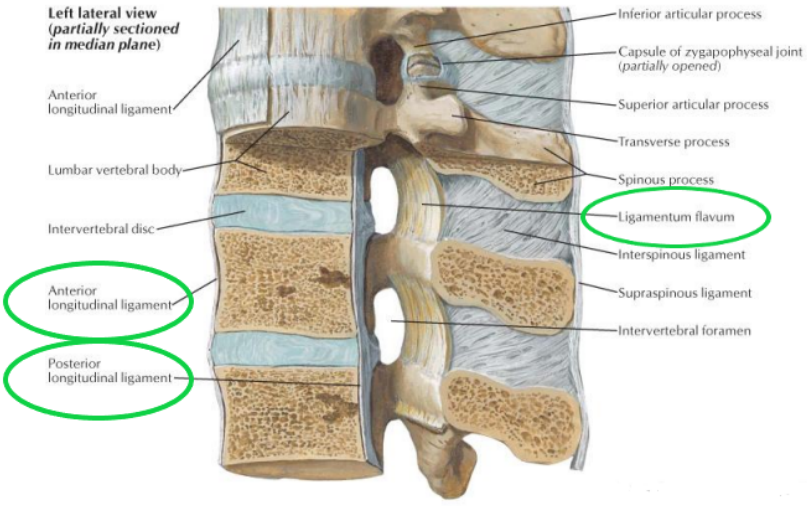

Figure 2.4: Ligaments present in the Spine showing, with green circles, the three major ligaments [Adapted from [23]].

2.2 X-ray imaging

X-ray imaging is a type of medical imaging used to obtain structural information of a specific region of human body. It has excellent properties for imaging, especially, to detect spinal diseases: fast and low-cost [30]. Figure 2.5 represents a normal radiograph system. In this technique, x-rays are produced in a x-ray tube through a process called *bremsstrahlung* effect. Then, the x-rays are passed through a collimator, which adjusts and shapes the x-rays coming from the tube [31]. Before reaching the patient region, this x-rays may be subjected to a filter in order to avoid, for example, low-energy x-rays, because these contribute to patient dose and not to the image formation [32]. After passing through the body and before reaching the imaging film, there may be a grid to avoid x-ray scattering and, then, prevent image blurring.

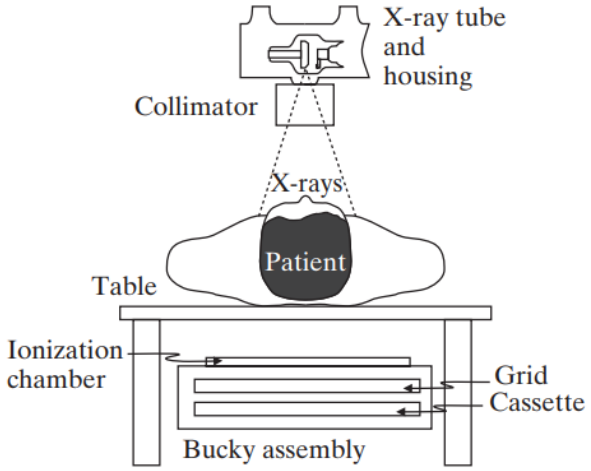

Figure 2.5: Conventional radiograph system [32].

2.3 Diagnosis of DISH

There are three major diagnosing criteria to evaluate this disease. The criterion created by Resnick and Niwayama, which is the standard diagnosing criterion, states that the ossifications must encompass at least four contiguous vertebrae and do not involve degenerative changes in the intervertebral discs. Also, the facet joints must be preserved. Finally, the apophyseal and sacroiliac. joints[8] must not be involved. Figure 2.6 is a illustration of this criterion. In the left image, the red arrows indicate the features of spine characterizing this criterion: Ossification of the AAL in at least four contiguous vertebrae (A); Preservation of interverterbral space (B) and facet joints (C); In the right image, the red curves indicate the sacroiliac joints, which must no be involved[33].

Beyond this criterion, other authors proposed other criteria for diagnosing DISH. Julkunen *et al*.[13] created a criterion which only differs from Resnick and Niwayama's in

the fact that they include bridged connecting two vertebral bodies in at least two sites of the thoracic spine.

Utsinger *et al.*[14] considered that three contiguous vertebral bodies and the presence of pheripheral enthesopathies were only necessary to diagnose DISH[15].

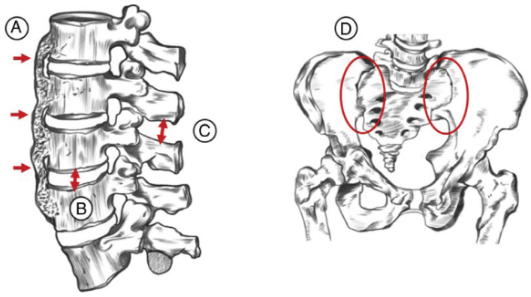

Figure 2.6: Criteria created by Resnick and Niwayma to diagnose DISH. (Left image): Red arrows indicate the (A) Presence of ossification in at least four contiguous vertebrae. (B) Preservation of the interverterbral space and (C) of the facet joints. (Right image): (D) Lack of involvement of the sacroliac joints (red curves) [33].

The diagnosis of this disease is mainly through imaging, specially radiography. This technique is more frequently used due to economic issues and usually anterior-posterior and lateral spine radiographs are recommended[16]. However, CT and MRI can also be used. Both imaging modalities have higher resolution than X-ray and provide a three dimensional visualization of structures, making it good to detect spinal injuries. Also, both can be used to evaluate the extent of ossifications in the spine. For example, they can be use to assess the extent of ossifications in the cervical spine and their impact on the esophagus[17]. These imaging modalites can, as well, be useful in differentiaing this disease from AS. AS, on contrary to DISH, usually affects the facet joints, which are connections between adjacent vertebrae, and CT can be useful in identifying changes in these structures. MRI, on the other hand, provides insight into inflammatory changes[10] in the spine, which are present in the AS.

Nonetheless, the diagnosis of the disease is rather difficult because it is usually performed by experts, by analysing radiographs, and these professionals have different experiences, which leads a high probability of variability of diagnoses among them[18]. Another problem in the diagnosis is the fact that there is the possibility of delayed diagnosis due to the presence of pre-existent abnormalities on the radiographs, maskering small fractures[19], and the fact that the aforementioned criteria are only visible, and mostly applicable, in later stages of the disease. Therefore, it is of utmost importance an early recognition of this disease in order to allow for a better management of metabolic diseases associated with DISH with the goal of reducing the progress rate of the disease[2].

2.4 Effect of DISH on the spine

As said before, DISH is characterized by the ossification of the AAL. The normal spine, this ligament is separated from the anterior aspect of the vertebral body by a thin radiolucent line. However, when this disease manifests, this separation is broken, and the ligament becomes fused to the anterior aspect of the vertebral body[34].

The changes in spine due to this disease typically occur in the anterolateral part of thoracic spine, contralateral to the descending aorta, due to the impact of the pulsating aorta. In the early stage of this disease, it is possible to see, in sagitall radiographs, small bony areas ahead of the disk space. As the disease evolves, the ossifications grow in size and thicken, particularly in the right and anterior side of verterbral bodies. In a lateral view of the spine, these ossifications resemble flowing candle wax, which can be attributed to the presence of segmental arteries which cross the vertebral bodies horizontally.

Nonetheless, DISH can also manifest in other sections such as Lumbar Spine and Cervical spine. Concerning lumbar spine, on contrary to the thoracic section, the flowing ossifications are frequent in both right and left sides of lumbar spine. Also, in this section, it possible to see the ossification of spinous processes and interspinous ligaments. Other possible consequences of the disease in this region are the spinal stenosis, mild to moderate narrowing of the intervertebral space and degenerative changes in the lumbosacral joint [4].

The cervical spine is another section prone to this disease. Here, the hyperostosis occurs in the lower half of the anterior vertebral body as a drooping drops. Then, these increase their size until they form enthesophytes and binding together. These enthesophytes extends themselves to the anterior and superior segment of the underlying vertebral body, which ultimately results in “candle flame” or “ bridge”. Also, other features of DISH in this section may occur in the cervico-occipital junction, where, due to bone formation, the vertebral bodies increase in diameter.

The difference between the cervical and thoracic spine ossification pattern can be explained by the fact that, in the neck, the main vessels are located lateral to the vertebral bodies and there are no segmental arteries. As a result, these arteries act as barriers to the development of DISH. Also, the fact that there no crossing segmental vessels in this section, lead to bar-like bony structure, on contrary to the flowing wax pattern of thoracic spine [8]. This difference can be seen in Figure 2.7. Here, images A and B are two sagitall images of the spine showing the different pattern of ossifications in the cervical spine (in blue) and the thoracic spine (in green). The images C and D are CT images, showing in yellow the position of the ossifications in the anterior part of the vertebral body in the cervical spine((c) and thoracic spine((d)). It is clearly that the position of ossifications are different in the two sections of spine. In the cervical spine, the ossifications are symmetrically disposed in the anterior part of the vertebral body, whereas, in the thoracic spine, the newly formed bone is located in the right anterolateral side of the vertebra, due to the impact of the pulsating aorta. Another important feature in image C is the fact that

the location of ossfications can lead to the displacement of the trachea(brown circle) and, then, causing airway obstruction.

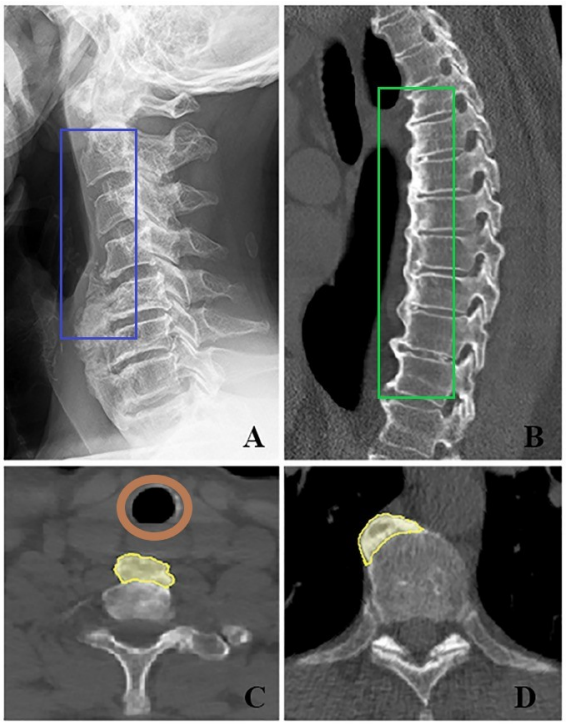

Figure 2.7: Patterns of DISH in cervical and thoracic spine. (A) Ossifications' Bar-like pattern (blue rectangle) in a sagitall radiograph of cervical spine. (B) Ossifications' "flowing wax " pattern (green rectangle) in a sagitall CT of thoracic spine. (C) Axial CT of cervical vertebra showing, in yellow and brown, the ossifications and the trachea, respetively. (D) Axial CT of a thoracic vertebra showing, in yellow, the ossifications [Adapted from[8]].

Despite the variety of ossifications patterns in DISH patients, these ossifications can be differentiated by those caused by AS, which is, as well, a hyperostotic disease, because it causes abnormal bone proliferation in spine.

The ossifications caused by this disease are called syndesmophytes. At early stages, their arise from the ossification of outer fibers of *annulus fibrosus* intervertebral disc, projecting vertically. As they develop and grow, they bridge the intervertebral disc, ultimately causing ankylosis, which is the fusion of vertebrae. The results of this is the so-called bammboo spine. This can be seen in Figure 2.8. Here, in a Sagitall radiograph of a 47 year old male, the white arrows point to the vertical syndesmophytes which led to the bridging of the anterior vertebral corners. It is also noteworthy the fusion of facet joints, specially at C2/C3 level(blue circle)[35].

As reported before, DISH is characterized by the presence of bridging osteophytes on the AAL. Nonetheless, in AS, the ossifications are called syndesmophytes, because they are calcifications present inside the spinal ligament or of the *annulus fibrosus*, and are often thinner and symmetrical [8]. Another differentiating feature of AS is the fact that this disease affects the facet joints, on contrary to DISH.

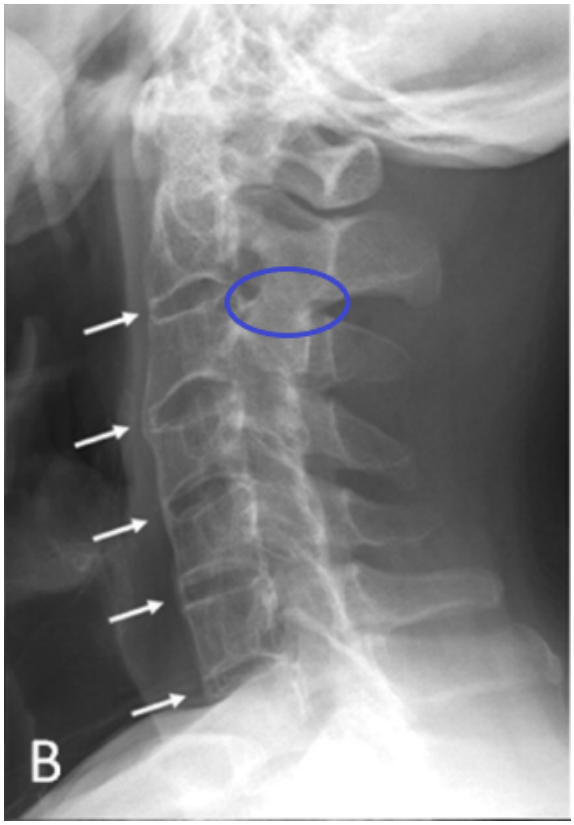

Figure 2.8: Sagitall X-ray image of a patient with AS showing, with white arrows and the blue circle, the syndesmophytes and the fusion of facet joints at C2/C3 level, respectively [Adapted from [35]].

2.5 Deformations in the spine caused by DISH

DISH and other spinal diseases cause deformations in the spine and vertebrae. In this sub-section, a description of the impact of DISH ossifications in the spine is provided.

As reported before in this chapter, DISH causes the abnormal formation of bone on the AAL. These ossifications can lead to an improper loading in the vertebrae, which can cause fractures on them, even with minor trauma, specially in advanced DISH patients[36]. These fractures are more frequent in the cervical and thoracic spine.

Patients diagnosed with DISH may develop fractures in the vertebral bodies due to loss of flexibility. This can be caused by greater stress due the ossification of the AAL [19]. This can lead to compressions fractures, that is, the collapse of the vertebral body, and dislocation injuries, where the vertebrae are displace from the normal position.

The most common mechanism of injury of the spine by DISH is the Hyperextension, which occurs when there is a sudden extension of the spine, leading to the compression of the vertebrae and dislocation of the spinal cord. In Figure 2.9, the image (A) shows an example of a fracture of a vertebral body caused by DISH, through the hyperextension mechanism.

Also, beyond involving the vertebral bodies, the endplates can also be involved, which

Figure 2.9: Fracture in a vertebral body caused by DISH, indicated by the black elipse [Adapted from [37]].

can lead to the disruption of the interverterbral disk[36], and,then, to irritation of nerves inside the *annulus fibrosus*, causing pain.

Moreover, DISH can lead to fractures in the cervical spine and cause, for example, odontoid fractures, which occur at C2 vertebra. Also, DISH can cause fractures or dislocations in the facet joints, leading to the disruption of the articulation between adjacent vertebrae and, consequent, destabilization of the motion of spine in the segment, where the facet joints are injured.

Beyond fractures on vertebral bodies, spinal deformations, such as scoliosis, can occur due to DISH. The pressure caused by the ossifications on the spine can be so huge that the normal architecture of the spine ca be altered, resulting in abnormal spine curvatures.

One commonly used metric to assess scoliosis is the Cobb angle. To calculate this angle, one need to define the two end vertebrae of the curve deformity. These are usually the ones with the endplates most tilted towards each other, as shown in Figure 2.10. Then, it is necessary to draw two tangents along the endplates, in a lateral spine radiograph. After this, it is also necessary to draw two lines perpendicular to the tangents ones, so that they intersect. Then, the angle at the point of intersection is calculated [38].

Several studies proved the impact of DISH on spine curvatures. For example, Yamada *et al*. [40] concluded that DISH patients had significantly more thoracic kyphosis, which is a condition where the curvature of the thoracic region is abnormal (bigger than 50 degrees), than non-DISH patients. The same study concluded as well that the patients with pathology had an increased lumbar lordosis, which is an excessive inward curvature at lumbar level, when compared with patients without DISH. In another work, Lorenzo Nardo *et al*. [34] found that high values of Cobb angles have been associated with DISH disease in older people only when the thoracic region is the pathological one. These findings can be useful to identify the extent of the disease and it's progression.

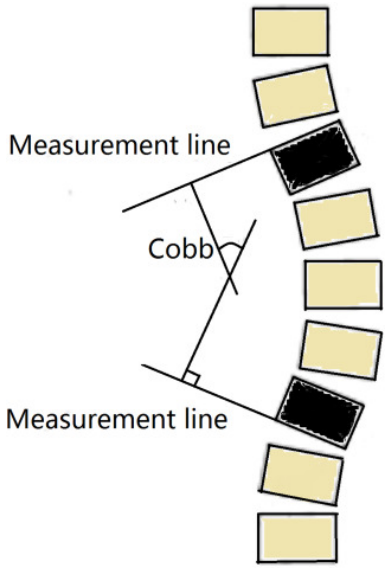

Figure 2.10: Schematic representation of how to calculate the Cobb angle [39].

2.6 Literature review

This chapter provides a literature review on the DISH assessment methods and automatic segmentation and diagnosing tools that have been proposed to segment pathological spine images spine, specially AS.

2.6.1 DISH assessment methods

As said in chapter 1, the normal diagnoses process of DISH passes through visualizing a X-ray image by experts in the area and then using the Resnick Criterion. However, this criterion is only suitable in later stages and it does not provide insight into the evolution of the disease. Thus, some other criteria have been developed to surpass these problems. For example, one of the approaches have been the grading of the extent of ossifications in the spine caused by DISH. To do so, in 1998, Mata *et al.* [41] created a score, usually known as Mata Score, to reveal insight into the degree of progression of this disease. In their work, the authors used both categorical and continuous measures to that purpose. The categorical evaluation was associated with the presence or not of ossifications and the extent of bridging of the disk space. Regarding the continuous measure, this was accomplished by a ruler, which was used to measure the ossifications size in the upper and lower endplates. This score ranges from 0 to 3, according to the following: 0 corresponds to lack of ossification in the ligaments and 1 correspond to ossifications without any bridging. 2 corresponds to ossification with incomplete bridging, and 3 corresponds to a complete bridging of the interverterbral space. Some [42] used the Mata Score to diagnose patients with DISH based on lumbar-spine X-ray images and the results showed that there is a huge probability that this method is capable of diagnosing DISH.

In another work, Kuperus *et al* [43] set out to find a criteria, based on a score system,

to evaluate Spinal CT images from patients and segregate them in three groups: no DISH, Early DISH and definite DISH. The method used in this work was a score system, which assessed the progression of bone formation in each segment of the spine. The score ranged from from 0 to 3, according to the presence of osteophytes, their length and the distance between the ossifications in adjacent vertebrae. After that, they found the best criteria combination to identify No DISH, Early DISH and DISH patients. The validity of this criteria was then assessed and the results showed that this criteria were acceptable to good.

2.6.2 Automatic segmentation and diagnosing tools

Although DISH has not been yet subject to a automatic diagnosing tool, some studies have developed automatic tools to evaluate AS a very similar disease to DISH. For example, Tan *et al.* [44] proposed a computer aided evaluation tool for AS in CT images. In this work, the authors resorted to a 3-D multiscale cascade of successive level sets, which follow the geodesic active contour formulation, to provide the segmentation of vertebral bodies and the syndesmosphytes, which are abnormal bone structures present in vertebrae. It aimed to measure the volume of this structures in order to assess the pathology. These results were then compared to a semi-quantitative evaluation made by a medical expert who visually inspected the CT scans.The results showed more than 90.00% of correlation between the specialist assessment and the algorithm.

In another work, Koo *et al.* [45] proposed an assessment tool based on deep learning algorithm to grade the structural damage from 0-3, as as result of AS, in radiographs. The results revealed a good performance, with an accuracy near 90.00% in all grades, demonstrating that it is possible to assess this structural changes in radiographs, where it is very hard to visualize using the visual observation method.

The present work aims to contribute to the diagnosing tool of DISH by using an algorithm of the family of active contours to achieve it.

Some studies have been proposed in this area. For instance, Sardjono *et al.* [46] proposed an algorithm based on interactive active contours to provided the segmentation of radiographs from scoliotic patients. Initially, the user had to put the initial contour close to the objects shape, which evolves until finds a homogeneous shape and the edges of the object. After this process, the resultant segmentation is converted into a binary image, which is used for segmentation evaluation. This is done by using two metrics: Misclassification Error and Relative Foreground Area Error. The first metric refers to the fraction of pixels which are misclassified relative to a ground truth segmentation and values close to 0 mean a good segmentation performance [47]. The second metric used is related with the amount of overlap between the area of the proposed segmentation and the ground truth and values close to 0 mean there is a perfect match between both areas[47].

The performance of this algorithm was compared with another segmentation called

interactive region splitting, which aims to split an image or region of image in subregions with similar features. The results showed that the use of active contours resulted in more effective segmentation, demonstrated by the 12.98% for Misclassification Error and 26.75% for Relative Foreground Area Error. The other segmentation method had 21.17% and 89.27%, respectively.

Juying Huang *et al.* [48] proposed an algorithm based on a improved Level-Set method for segmentation of pathological vertebrae in CT images. In this work, level-set methods were combined with active contours. The main feature of this algorithm is the lesser sensitivity to the initial contour, which is a common problem when using active contours. The results were very promising for the 56 patient datasets, indicated by 94.00% of Dice Coefficient. It is noteworthy that it was able to segment images with intensity inhomogeneity and blurry boundaries, which is another common problem in the active contour approach.

2.6.3 Previous works

The proposed work follows two previous works: Lopes[21] and Viegas [18]. Lopes [21], in his work, proposed an semi-automatic algorithm, based on empirical methods, to provide the segmentation of non-pathological vertebrae, with the goal of being applied to DISH radiographs. The algorithm needed a previous knowledge of the anatomy and appearance of the vertebrae on radiographs, in order to provide the segmentation. The results of segmentation were good and, when compared with manual segmentation of experts, revealed that the performance of the algorithm was equal or superior to the performance of the experts. Despite this results, the algorithm proposed had limitations.

Thus, Viegas [18] proposed vertebrae models of non-pathological radiographs based on manual segmentation of experts in 21 extra-long coronal radiographs. The algorithm required the user to indicate the intervertebral disc location between L4/L5. Hence, the proposed algorithm was semi-automatic. The results were good, which is proven by the following segmentation metrics: Dice coefficient of 89.57 ± 3.91%, and Hausdorff distance of 4.01 ± 1.52 mm. Despite the results, the work has some limitations, for example, the algorithm leads to a soft segmentation of vertebrae and, therefore, it does not capture their specific morphology. This is quite important in pathological vertebrae (i.e, DISH vertebrae) because their morphology may be altered and to assess the impact of the disease in these structures, it is necessary to obtain a specific segmentation of them.

2.6.4 Conclusion

Despite the Resnick Criterion is the current standard method to diagnose DISH, other studies tried to make use of score systems to evaluate DISH and its progression, based on the size of ossifications, with good results.

Other authors tried to make automatic diagnosing tools of AS, by using algorithm from the active contour family, and combining them with deep learning, with good performance

results.

Despite this good progress in trying to assess the severity and progress of DISH as well of similar diseases, an automatic diagnosing tool has not been created yet for this disease.

The work project, in which this work fits, have been trying to find a way to provide automatic diagnosing tool of DISH. Firstly, with Lopes [21], where a semi-automatic algorithm for the segmentation of non-pathological was created and the results obtained were good, although with vertebrae segmentation limitations. Then, with Viegas [18], who created generic vertebrae models to provide the segmentation of vertebrae, obtained good results. However, with the limitation of providing a smooth contour of the vertebrae, instead of capturing their specific morphology.

Thus, further work is needed to improve the segmentation of these previous works, in order to obtain a specific segmentation of vertebrae, specially in pathological cases.

3

Image processing

3.1 Image processing

In order to achieve the goal of this thesis, some image processing concepts need to be clarified. In this chapter, concepts related with image contrast enhancement, type of noise present in radiographs and examples of method to reduce them are described. Also, other concepts, such as morphological operations, affine transformations and segmentation methods, are also mentioned here, for a better understanding of the present work.

3.1.1 Noise present in X-ray images

Medical images, such as radiographs, in their raw state, are often corrupted by noise and many artifacts. The result is the poor quality of images which can lead to misinterpretations in clinical context [49]. Therefore, there are many image processing techniques able to reduce or eliminate the impact of these undesirable elements in images.

In X-ray images, two commonly types of noise are Poisson Noise and Gaussian Noise. The first is usually present due to the stochastic nature of the photons collection at the receptor. These follow Poisson processes, which means that the probability of arrival of a photon to the x-ray detector is not affected (independent) by the arrival of another and the average rate of arrival of a photon at the detector is constant. Therefore, follow the Poisson distribution, represented mathematically in equation 3.1. This equations refer to the probability of k ($k = 1, 2, 3, ..., \infty$) number of arriving photons to the x-ray detectors, $P(k, \lambda)$. This probability is dependent on a constant average rate λ, which is the average number of photons arriving to the x-ray detector in a fixed time interval and is constant in Poisson processes.

$$P(k, \lambda) = \frac{e^{-\lambda}\lambda^{K}}{k!} \tag{3.1}$$

This is a signal dependent noise, thus, it could be attenuated by increasing the dose value, when obtaining the X-ray images. However, this is not recommended, due to health issues. Hence, the use of image denoisin methods is the best approach. One possible filter to remove this kind of noise is the Median filter[50]. This is a non-linear filter, which runs

through each pixel of the image and replaces its value by the median of the neighbouring pixels. It allows removing outliers (i.e, noise), without losing the quality of images and, specially, near the edges of objects[51].

The second type of noise is Gaussian noise, which follows a Gaussian distribution, whose mathematically representations is in equation 3.2. This equation refers to the probability density function of a Gaussian distribution $f_g(x)$ with mean value a and a standard deviation of σ. This noise is additive, which can be formulated as follows: $v(x,y) = I(x,y) + \eta(x,y)$, where $x, y \in I$, I(x,y) is the original image, $\eta(x,y)$ is the gaussian noise and v(x,y) is the final image corrupted with Gaussian noise. This noise is the result of contributions from a large number of independent signals (large number of photons), as a consequence of application of the Central Limit Theorem. One way to remove this type of noise is by applying a Gaussian filter. This is a linear and low-pass filter and it works by running through the image, pixel by pixel, and replacing the value of that pixel by the value obtained by a Gaussian-weighted averaging of the pixel's neighborhood. The image pixels are smoothed and, therefore, it allows reducing noise[51].

$$f_g(x) = \frac{1}{\sqrt{2\pi\sigma^2}} e^{\frac{-(x-a)^2}{2\sigma^2}} \tag{3.2}$$

3.1.2 Histogram equalization

Histogram equalization is part of image processing techniques aiming to improve the contrast of images. An histogram consists a representation of the frequency of each gray-value pixel in a image. Histogram equalization consists spreading the pixels over all grayscale values in a image, in order to obtain an histogram in which all pixels have, approximately, the same frequency. Figure 3.1 demonstrates the histogram equalization on a X-ray image of the spine. The top image is the image before equalization and the correspondent histogram. The bottom image is the image after the equalization and the correspondent histogram after equalization. The histogram of the top image is not equally distributed over all bins, however, after the application of the histogram equalization, the result (bottom image) is an histogram, in which the pixels have, approximately, the same frequency. As a result, the image associated with the equalized histogram reveals an increase in contrast, specially near the edges of vertebrae.

However, this technique is suitable when a global contrast is needed. Since one of the most important features in X-ray images of spine and specially in the context of this work are the edges of vertebrae, the adaptive histogram equalization technique seems to be useful. This method allows local contrast enhancement by dividing the image in different blocks and computing histogram equalization in each of them, providing a local contrast.

3.1.3 Inverse Gaussian gradient operator

Inverse Gaussian operator is another concept of image processing that will be use in this work. This operator allows one to identify the edges of structures in a grayscale Image

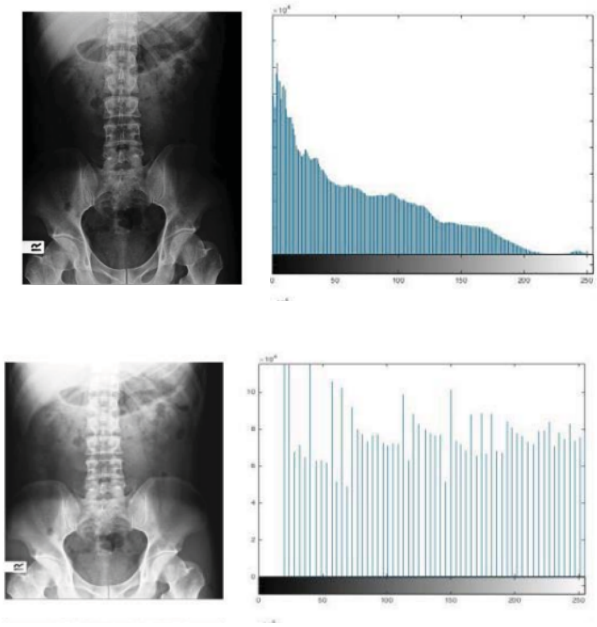

Figure 3.1: Histogram equalization: (Top image)- Before equalization and (Bottom Image) After equalization.

I and it is usually applied as a pre-processing step for morphological geodesic active contour, which will be discussed later in this chapter.

This operator depends on two parameters: σ and α. The first parameter is used to compute the magnitude of gaussian gradient and represents the standard deviation of the Gaussian filter. Figure 3.2 shows an example of this step. The magnitude of gaussian gradient with σ=5 is computed over the image on the left and the results is shown on the right. In the image on the left, the black regions refer to uniform areas of the right image and the white regions represent the edges of objects of the right image.

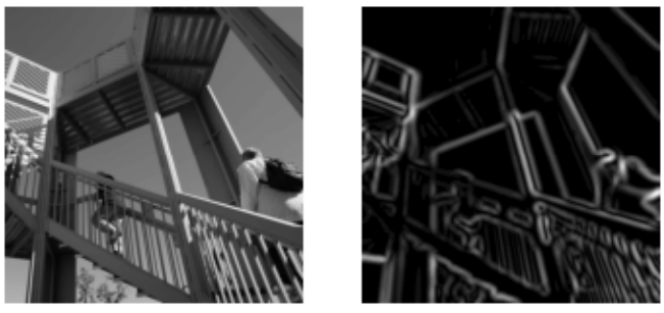

Figure 3.2: Application of gaussian gradient with σ=5. (Image on the left): Original image. (Image on the right): Result.

After this step, the values of the magnitude obtained are inverted to the interval [0,1], according to the equation 3.3. In this equation, α represents the parameter which controls the steepness of inversion and *gaus_magn* is the image after the magnitude of gaussian gradient is computed. The first parameter allows one to control the transitions

between flat and border areas and larger values enhances this transitions, allowing a better differentiation of both areas.

$$\frac{1}{\sqrt{1 + \alpha * gaus\_magn}} \tag{3.3}$$

The resultant image after application of this inversion of magnitude operator is found in Figure 3.3. It is possible to see here that uniform areas on the left image (regions in black) are set to values close to 1 and the edges of the objects (white) are set to values close to 0. The result of the applications of this operator is the right image.

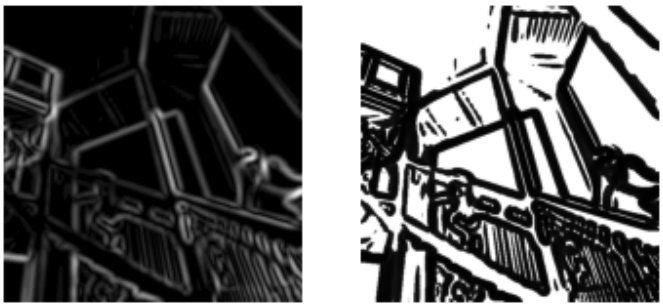

Figure 3.3: Application of gaussian gradient magnitude inversion with α=100. (Image on the left) Before of application. (Image on the left): Result.

3.1.4 Morphological Operations

Morphological operations are part of image processing techniques used to remove imperfections that causes distortions in shapes and textures of images. These operations make use of structuring elements, which are used to interact with the image. These elements have three characteristics: shape, size and origin, or seed point, which must be chosen according to the need of processing. The first is related with the arrangement of zeros and ones in a matrix. The size can be seen as windows in which the operation is done in images. The origin is the pixel chosen to be processed. The interaction is done in such a way that the origin pixel must be translated to all possible pixels in the image. Figure 3.4 shows an example of a structure element[52].

The two fundamental morphological operations are Erosion and Dilation and the other build on these two.

3.1.4.1 Erosion

This morphological operation aims to reduce an object's size and unwanted or small-scale details [52] by increasing the pixels with zero value and decreasing the ones with set to one. It removes elements lower in size than the structure element. This can be useful, for example, in removing noisy connections between objects[52].

The definition of this morphological operation is: The erosion of a binary image A by a structuring element S produces a new binary image g, according to equation 3.4.

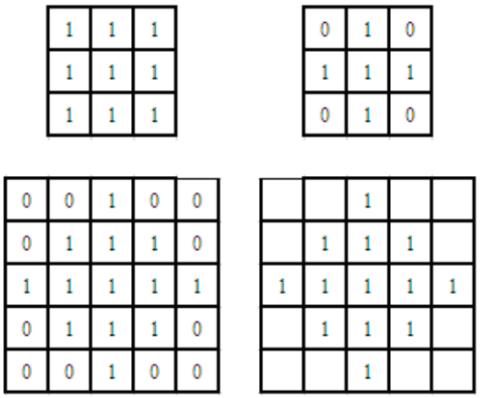

Figure 3.4: Example of structuring elements with different sizes and shapes [53].

$$g = A \ominus S \tag{3.4}$$

After the transformation, the new image g has ones in all seed points of S, where the pattern of S match exactly the input image A pattern, and zero where this is not seen. Figure 3.5 shows a example of erosion and it is possible to see that there are white pixels from letter D, shown by the red arrows in the right image, that were eroded and removed from original image (left image).

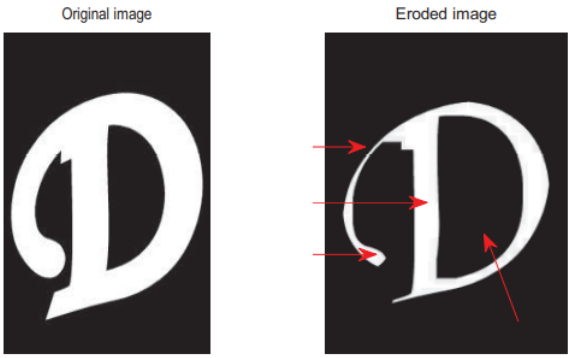

Figure 3.5: Example of erosion [53]. (Left Image) Original Image and (Right Image) after erosion [52]. The red arrows show the pixels removed by Erosion.

It is noteworthy that the larger the size of the structuring element, the larger the effect of erosion.

3.1.4.2 Dilation

In contrast to Erosion, Dilation increases objects in size and also fills holes in continuous objects, by increasing the number of pixels with value one and decreasing the ones with zero[52].

The definition of this morphological operation is: Dilation of a binary image A by a structuring element S produces a new binary image g, according to equation 3.5:

$$g = A \oplus S \tag{3.5}$$

After the transformation, the new image g has ones in all seed points of S where A image pattern and structure element S pattern has 1 matched pixel and zero where there is none. This transform adds more pixels to the boundaries of regions, as it possible to see in Figure 3.6 in the grey pixels. In this case, the original image, on the left, was subject to Dilation, and there was a increase in size of the object (D letter). Example of pixels added to this object are represented by the red arrows, on the right image.

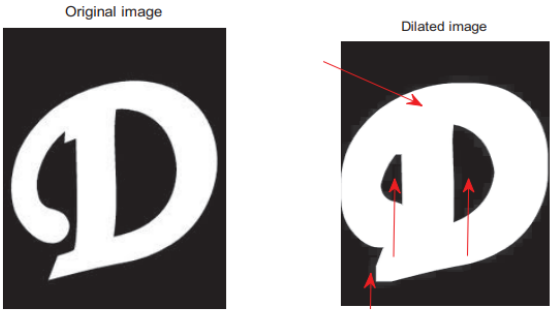

Figure 3.6: Example of dilation.(Left Image) Original Image and (Right Image) after dilation [52]. The red arrows show the pixels added by Dilation.

Many combinations of these two operations can be made. Some applications of these combinations is the removal of noise and extraction of external edges, internal edges and the pixels on the edges of objects.

3.1.5 Affine transformations

Affine transformations belong to the class of 2D geometric transformation in which the parallelism of lines are preserved, however, the angles and lengths can change. In these transformations, intensity values of pixels located in (x,y) position in images are mapped to other coordinates in the output image by applying linear operations, such as translation, rotation, scaling and/or shearing [54]. The four linear operations are represented in Figure 3.7. These type of affine transformations have been applied to biomedical images processing, specially in spinal diseases. In [55], for example, affine transformations were used to registrate the vertebrae models the authors constructed to the spine of a patient, in order to provide the segmentation of vertebrae and estimating their position and rotation in spine.

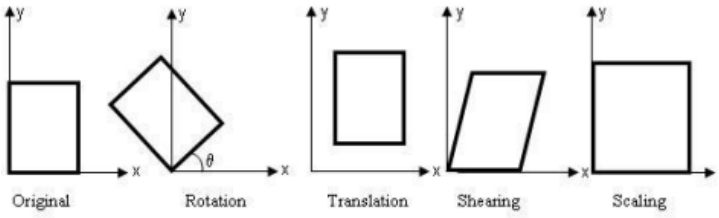

Figure 3.7: Examples of linear operations applied in affine transformations [54].

3.1.6 Segmentation methods

Segmentation of medical images is of utmost importance nowadays. The vast amount of medical image data which is produced nowadays make necessary the use of computer-aided-diagnosis tools to help clinicians and radiological experts to separate a certain region of interest from the rest in order to evaluate it in a more precise way. This segmentation process is accomplished by dividing an image into a set of pixels, characterized by an intrinsic feature or features such as the color, grayscale value, brightness, contrast [56]. The result of this segmentation is easier to analyse and provides more insight regarding, for example, a disease.

3.1.6.1 Local Segmentation

One category for segmentation methods is local segmentation. This is accomplished by operating on a small amount of pixels, and is used to target image processing techniques, such as denoising, pixel classification and edge detection, to regions of the image that present rather similar characteristics [56]. This type of segmentation is useful when a very small object, for example, a small tumor, is being overshadowed by the background[57].

3.1.6.2 Global segmentation

This type of segmentation is concerned about providing the segmentation of the whole image and dividing it according to some characteristics, for instance, the color or the brightness. In this category, there are three subcategories such as: Region-based approach, Boundary approach and Edge detection [56]. For the scope of this work, it will be only focused the Edge detection approach.

3.1.6.3 Active contours

Active contours, or snake models, are part of segmentation methods that exploit deformation models, which make use of image forces (i.e, the gradient in images's intensities) and external constraints (i.e, balloon forces, used to push the contour to the boundaries) to isolate pixels of interest for posterior analysis. There are two types of active contours models: Edge-based and Region-based models. Essentially, in the former, the initial curve evolution is determined by edge indicators, for example, gradients in the image's

intensities, and it should provide the contour of high gradient magnitude boundaries. In the latter, the initial curve evolves due to regional information, for example, intensity statistical information inside and outside of the contour and it should stop at regions where there is balance between inside and outside regional informations. Examples of active contours are the snake model, the snake model with balloon forces as external constraint and snake model with gradient vector flow as external constraint, which are parametric active contour models. As non-parametric active contour models, there are the geometric or geodesic active contour [58]. An example of application of active contours in medical images is represented in Figure 3.8. Here, it was proposed to segment the ventricles (represented in black at the center of a Brain CT, on the left image), which are hypointense regarding the surroundings. After applying the active contour algorithm, the result is found on the right image, in green.

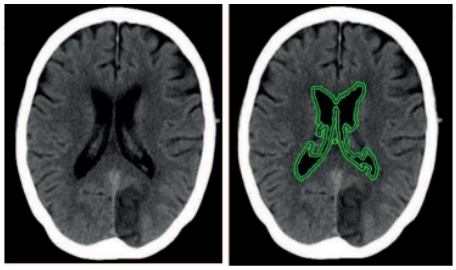

Figure 3.8: Example of application of active contours in the segmentation of ventricles in a Brain CT. (Left image): Original image. (Right image): Original image with the segmentation result in green [58].

Snake Model

A snake is a parametric spline curve C defined as $C(s,t) = (x(s,t), y(s,t))$, where x and y are the coordinates of the two-dimensional curve, s is a linear parameter, s $\in [0,1]$ and t is the time parameter $t \in [0,\infty]$.

The curve movement and evolution in the searching for the boundaries of an certain object, for example, is influenced by it's energy. This energy, also called $E_{snake(contour)}$, is composed of two energies, as seen in equation 3.8: The first term corresponds to the internal energy($E_{internal}$) and the second term to the image energy(E_{image}). As seen in equation 3.6, the first terms depends on two parameters: α, which controls how far the snake can be extended and it's elasticity, and β, which controls the smoothness of the snake. This energy is minimum when the snake has a relevant shape to be regarded as the real shape of the object. Also, in this equation, $C'(s)$ refers to the first derivative of the curve C and $C''(s)$ to the second derivative of the curve C.

On the other side, the second energy, whose mathematical representation is in equation 3.7, represents an image force, which leads the snakes to the edges of the image. Thus, its minimum is achieved at the object boundary position. This energy depends on two parameters: w_{line} and w_{edge}. The first is called the line efficient and controls the attraction to brightness. Negative values of this parameter will push the snake away from bright

regions. The second is called the edge efficient and it controls the attraction to the edges. Negative values of this parameter will push the snake away from the edges[58].

The snake C(s,t) gradually moves in a image in order to minimize the energy functional represented in equation 3.8. Also, this snake evolves according to a predefined number of iterations, which is set by the user. Beyond that, at each iteration, the snake moves according to a predefined time step. This parameter will influence the speed of convergence. At the end of each iteration, the curve is subject to a smooth step, where the shape of curve is revised. This is illustrated in Figure 3.9, which shows a representation of the snake evolution process during the search for an object boundary. At the beginning of the evolution process, the energy of the curve Γ_0 (green) is at its maximum as well as the velocity $\overrightarrow{v}$ of evolution, because the image forces here are maximum. As it evolves, the curve changes the morphology (dark blue and light blue curves) and moves gradually in order to minimize it's energy. As it gets closer to the edges (lower image forces) of the object, the velocity of curve motion decreases, until it finally hits the final curve (red).

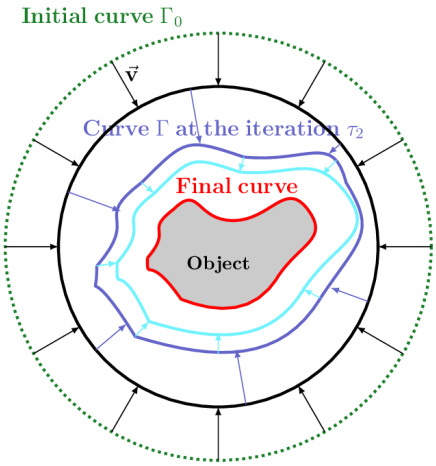

Figure 3.9: Representation of active contour segmentation. The initial contour Γ_0 (green) deforms as it evolves (dark blue and light blue curves) to adapt to the edges of the object (red curve) [59].

$$E_{internal} = \int_0^1 1/2(\alpha\,|(C'(s))|^2 + \beta\,|(C''(s))|^2\,ds \tag{3.6}$$

$$E_{image} = w_1|\nabla I(C(s)| + w_2|\nabla I(C(s))|^2 \tag{3.7}$$

$$E_{snake(contour)} = \int_0^1 1/2(\alpha\,|(C'(s))|^2 + \beta\,|(C''(s))|^2\,ds + w_1|\nabla I(C(s))| + w_2|\nabla I(C(s))|^2 \tag{3.8}$$

Despite this two energies being the only usually applied in these models, other external forces can be imposed by the user, such as inflation forces (balloon model), which will be discussed later in this chapter.

According to [60], there are three key limitations in these models. One is the fact that that the curve must be initialized near the desired boundary, otherwise the curve can get trapped in false or weak minima. The other is that it cannot handle concave boundaries and variations in topology, due to the fact the snake is parameterized . Moreover, this approach is characterized by having numerical instabilities [61][62]. This can be related with the fact that the introduction of discrete time step can lead the snake to oscillate between the minima or even get trapped in different local minima.

Balloon Model

The Balloon model was designed to overcome some weaknesses of the snake model. Those limitations are related with the initial position of the snake. For example, if the snake is smaller than the real contour, the snake will not be able to find the right contour and will collapse totally. To demonstrate this, one can imagine a black rectangle in a white background. If the snake is put inside the black rectangle, despite the good edge detection, the snake will shrink, until is completely gone[58]. Also, in the snake model approach, if the initial curve is set far from the edges, the curve will not be attracted by those edges.

To surpass these problems, in this model, as shown in equation 3.9, new forces acting on the snake are introduced, where k_1 stands for the magnitude of the force. This parameter can be either positive or negative: if positive, it will inflate, if negative, it will deflate. Thus, in the case of the black rectangle mentioned before, the sign of k_1 could be set positive and the curve would inflate until reaching the edges of the rectangle[63].

$$F_{inflation} = k_1 \overrightarrow{n}(s) \tag{3.9}$$

Here, k_1 represents the magnitude of the curve and $\overrightarrow{n}$ represents the normal unity vector of the curve.

One advantage of this model is that it stops the curve from staying trapped in false weak edges (i.e, noise isolated points) and goes on with the evolving process until it finds the real strong edges. This advantage leads to another, which is the widening of the spectrum of the initial guess position possibilities[63][58]. This allows the curve to be initialized far from the objects boundaries, on contrary to the traditional snake models.

An example of the improvement this model brought to the traditional snake model approach is found in Figure 3.1.6.3. Here, it was proposed the segmentation of a oval shape within a image corrupted with noise. The initial contour used is found in the top image (red). The results for the Snake model is found in the left image of the bottom (red). The result for the Balloon model is found in the right image of the bottom (red). As possible to see, with the Balloon model, the initial contour had a better adjustment to the edges of the shape. On the contrary, with snake model, due to the noise, some points of the initial contour stopped at those noise points, during the evolution of the curve.

Despite these advantages, the value for this k_1 cannot be either too small or too big, because must be in balance with the the regularization forces (i.e, smoothness energy) and the edge forces (i.e, image energy). Essentially, the inflation force must be enough, so

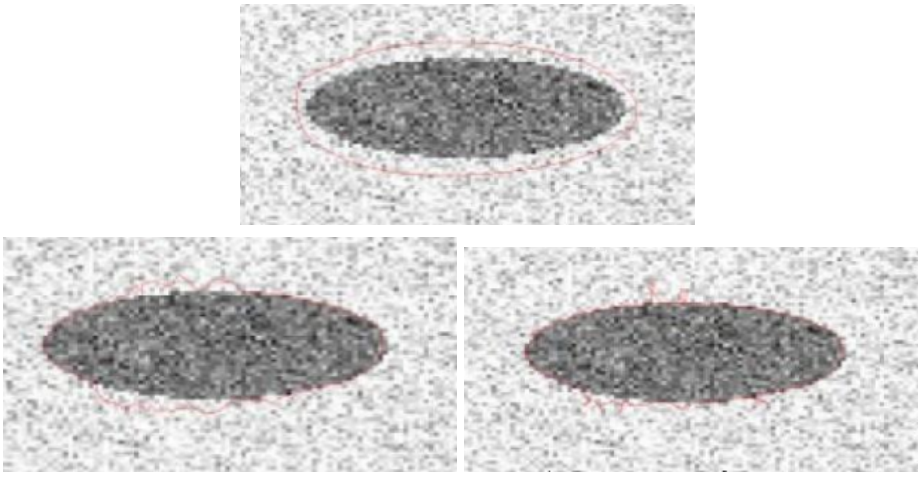

Figure 3.10: Improvement on segmentation of an oval curve in a noisy image that the Balloon model brought to the original snake model approach. (Top image): Initial contour (red curve) used for segmentation. (Bottom Left image): Segmentation result (red curve) by traditional active contour algorithm. (Bottom right image): Segmentation result (red curve) by using traditional active contour algorithm with Balloon forces [64].

that the image force is able to adjust with it, in order to find the right edges. For example, the case of the Figure 3.11. In this case, the initial contour (red rectangle) is supposed to evolve until it reaches the edges of the shape. In both cases, the value of k_1 was not set properly. On the left image, the value is not big enough to let the curve fit the entire shape, however, it is too big to, in certain regions of the curve, let the curve leak beyond the edges of the object (see white arrows). Thus, the initial contour was not able to adjust perfectly to the right shape. On the other hand, if the inflation term is increased, as in case of the Right image, the curve may fit the shape of the object in some regions and in other regions evolve beyond the edges (see white arrows) and finish in weak ones (ie, weak boundaries or noise points)[65].

Another drawback of this model is the slow processing [58].

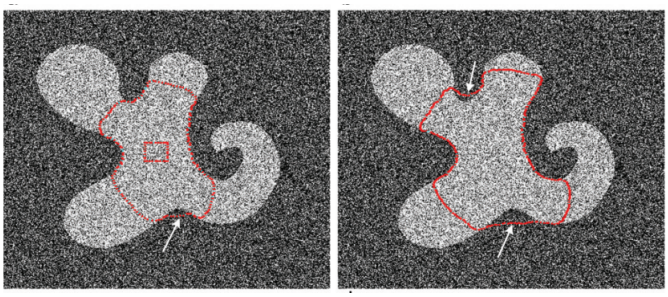

Figure 3.11: Example of difficulties in determining the right value for k_1 in the active contour segmentation with balloon forces [65]

Gradient vector flow

The Gradient Vector Flow (GVF) was designed to overcome some other limitations of the snake models, namely, the poor performance on concave boundaries and low

performance on the segmentation of objects far from the position of the initial contour [58].

In this approach, it is necessary to compute the gradient vector flow field. To do so, firstly, it is computed the edge mapping function f(x,y) from Image I(x,y) $I : R^2 \rightarrow R$. This accomplished by convolving a 2D gaussian function G(x,y) with I(x,y) and calculate the magnitude of the gradient, as seen in equation 3.10

$$f(x, y) = -\nabla|[G(x, y) * I(x, y)]| \tag{3.10}$$

Then, the gradient vector flow is determined as the vector $v(x, y) = (u(x, y), v(x, y))$, which minimizes the energy functional ϵ, represented in equation 3.11. This equation has two terms: The first, on the left, is a smoothing term. The second term, on the right, is related with the image gradient. The first term is dependent on a parameter μ, whose value is dependent on the noise level, for example, if noise is high, this parameters must be high as well[58].

$$\epsilon = \int \int \mu(u_x^2 + u_y^2 + v_x^2 + v_y^2) + |\nabla f|^2 |v - \nabla f|^2 dx dy \tag{3.11}$$

where ϵ represent the energy functional to be minimized, u and v represent the coordinates of the function v and f is the edge mapping function. The parameter μ controls the effect of noise level in the segmentation process.

After computing the vector $v(x, y)$, the image term in equation 3.8 is replaced by this vector. As a results, the the equation for a gradient vector flow snake, seen in equation 3.12, is obtained.

$$E_{snake(contour)} = \int_0^1 1/2(\alpha \left|(C'(s))\right|^2 + \beta \left|(C''(s))\right|^2 ds + v \tag{3.12}$$

Figure 3.12 shows an example of the improvement GVF modes brought to the original snake model. In this figure, it is proposed the segmentation of a scissors, characterized by it's concave boundaries, with the initial contour seen in the leftmost image(blue). The snake model result, seen in the middle image, was not able to provide the segmentation because of the concave boundaries of the object. However, as seen in the right image, the application of GVF led to the segmentation of the whole object[64].

Figure 3.13 shows another example of using GVF as segmentation algorithm for the Left ventricle of human heart in a MRI image. Here, the whole process of obtaining this segmentation is shown: from the edge mapping function computing to the final result. In this figure, (a) shows the left ventricle in a MRI image of the heart (short axis). (b) shows the edge mapping function *f(x,y)* of the image with σ=2.5. (c) shows the the gradient vector flow of the image. The segmentation result in a white curve is shown in (d).

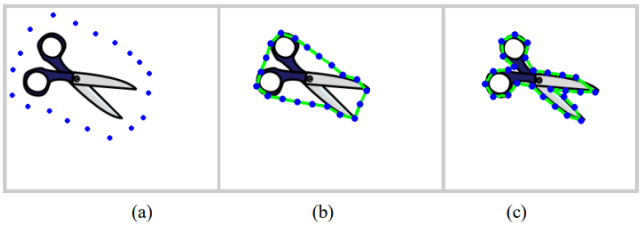

Figure 3.12: Representation of improvement of segmentation on concave boundaries that the GVF models brought to the traditional snake model approach. (a) Initial contour(blue). (b) Traditional active contour segmentation. (c) Traditional active contour segmentation with GVF as external force [64].

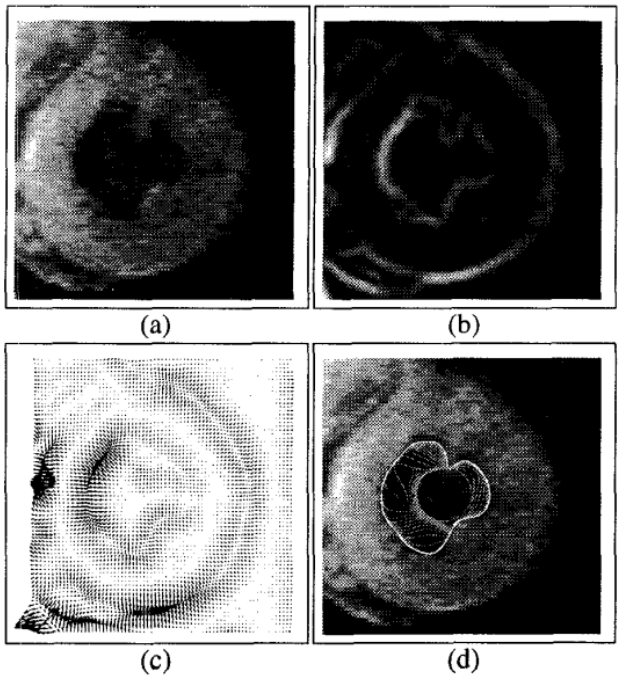

Figure 3.13: Whole process of application of GVF as external force for active contour segmentation of a medical image. (a) MRI of the left ventricle of a human heart(a). (b)- the edge mapping function f(x,y), with σ=2.5. (c)- GVF of image. (d)- Left ventricle segmentation shown as a white curve [60].

3.1.6.4 Geodesic active contour models

To surpass other drawbacks of traditional active contours models, for example, the fact that the original snake model cannot handle topology changes during the curve evolution, Caselles *et al.* [61] proposed a new active contour model approach: geodesic active contours models.

The idea behind this approach is to find contours of objects, in a image $I : R^2 \rightarrow R$, relying on the geometrical evolution equation of a geodesic active contour C(t). This curve, instead of being parameterized, is initially represented as a zero level-set, which is a surface in a three dimensional space, of a function of higher dimension $\Phi(x, y, t)$.

Equation 3.13 shows the mathematical formulation of the zero level-set. This function embeds the contours of the objects to be found, which are found not directly, but implicitly, because these models work with whole regions, instead of edges, like the traditional snake model.

$$C(t) = \{x, y | \phi(x, y, t) = 0\} \tag{3.13}$$

The evolution of the geodesic active contour can be formulated mathematically according to the equation 3.14.

$$\frac{\partial \phi}{\partial t} = g(I)|\nabla \phi|(div(\nabla \frac{\nabla \phi}{|\nabla \phi|} + v)) + \nabla g(I) \nabla \phi. \tag{3.14}$$

where ϕ represents the level-set function, *g(I)* represents the edge indicator function, I is the image and v is a parameter which controls the balloon force.

This equation is composed of two parcels: The first on the left is associated to the internal energy and the second on the right is associated with the external energy. The former has two components: one related with the smoothing operator, which smooths the curve in high curvature segments, and the second related with balloon force. This balloon force is responsible for inflating or deflating the curve.

The latter component is in charge of evolving the curve to the desired boundaries[66]. The effect of all three components are controlled by the *g(I)* parameter, which is the edge indicator function.

The edge indicator is normally formulated as seen in equation 3.15:

$$g(I) = \frac{1}{1 + |\nabla (G\sigma * I)|^2} \tag{3.15}$$

where *g(I)* represents the edge indicator function, I is the image where the objects to be segmented are, and $G\sigma$ represents the gaussian function with a certain value of σ. It is noteworthy that this functions is low where the gradients are high.

The curve deforms during its evolution, through a velocity influence, which is composed of two terms: one related to the regularity of the curve and the other related to either the shrinkage or expansion of the curve towards the boundaries of objects.

During the evolution, the model has the capability of automatic changes in topology[67], for example, splitting and merging, making it possible to detect more than one object during the curve evolution, even when there is no previous information regarding their number.

Figure 3.14 illustrates the evolution of the initial level-set (top Image in red) in order to segment two objects (bottom image in red). At the beginning (t=0), the initial curve is set as the zero level-set of the function $\phi(x, y, t)$ and initial curve does not have a previous knowledge of the number of objects to be segmented. As it evolves, the curve moves gradually, according a velocity, which changes over time, dependent on the position relative to the highest gradient (at it gets closer to the boundaries of the objects, the

velocity decreases) and the smoothness of the curve (internal energy of the curve, i.e, the lesser the internal energy, the lesser the velocity). Also, during the evolution, the curve automatically splits (red curves in the Bottom image), in order to the segment both objects.

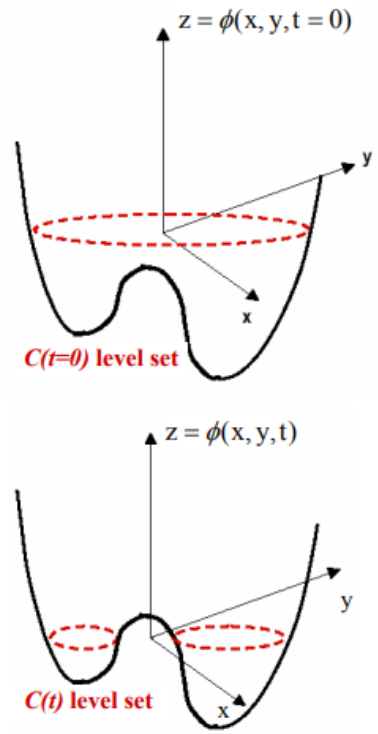

Figure 3.14: Example of level-set curve evolution . The black line represents the level-set function. (Top image) Initial curve C (red dotted curve) at t=0. (Bottom image) Curve at t [68].

This method has better performance than the other active contours because it allows the segmentation of various objects and the curve does not stop a local minima, during the evolution of the curve[69].

On other hand, one drawback associated with level-set solutions by using numerical operations is that it can result in inaccuracies and sluggishness due to the numerical approximations.

3.1.6.5 Morphologicalgeodesic Active Contours

Traditional geodesic active contours rely on numerical operations to solve Partial Differential Equations (PDE). However, due to the disadvantages named before regarding numerical approaches, a new approach[70] to this method was created in order tot replace numerical operations with morphological operations with the same infinitesimal behaviour as equation 3.14[66]. According to the authors, the terms in PDEs for contour evolution algorithm (balloon force term, attraction force term and smoothing term), seen in equation 3.14, are replaced by the combination of morphological operators, such as

dilation and erosion.

Here, the initial level-set curve u : $R^2 \rightarrow 0, 1$ corresponds to a binary component (u(x)=1 inside the contour and u(x)=0 outside the contour). Similar to the geodesic active contour approach, this level-set comprised the region of interest, where the desired object or objects to be segmented are denoted.

This initial level-set curve will evolve, according to a predefined number of iterations n, and a balloon force parameter ν, which will determine if the curve inflates or deflates. In terms of morphological operations, if the curve inflates, it is applied the Dilation, otherwise, it is applied Erosion. Moreover, as said before, the initial level-set curve denotes the desired object or objects to be segmented. This can accomplished by applying the Inverse Gaussian operator of the original image, which was described before in this chapter, and determines the gradient at each point of the image I: *g(I)*. Another term which will influence the evolution of the curve is the smoothing operator μ. This must as well be predefined by the user and it will influence the number of time this smoothing operator will be applied, per iteration, to smooth the curve.

The three terms (the term related with the balloon force, the term related with the attraction force and the term related with smoothing operator) are also represented inn equation 3.14, which represents mathematically the evolution of the geodesic active contour. In the morphological geodesic active contour approach, these three parcels have discrete versions, which are represented in equations 3.16, 3.17 and 3.18, respectively.

Essentially, the curve u^{n+1} is defined by u^n, which represents one iteration, through application of three steps and are mathematically represented in equations 3.16, 3.17 and 3.18.

The equation 3.16 refer to the balloon force term. As said before for the geodesic active contour approach, *g(I)* is a term which controls the balloon force strength. *g(I)* allows the curve to move fast in because the in uninteresting areas (in these low-gradient areas, *g(I)* is big). In this equation, the effect of this term can be discretized by using a θ threshold. This parameter controls the velocity of the curve movement at each point x_i, and it helps the curve not to stuck in low gradient areas of the image. If *g(I)* is high in an certain point of a curve, that point is updated with the balloon force. If not, the point is not changed. Moreover, the application of erosion (curve shrinking) or dilation (curve expansion) depend on the parameter $\nu \in [-1, 1]$: if ν >0, it is applied dilation,if ν<0, it is applied erosion. This parameter is chosen by the user[71].

$$u^{n+\frac{1}{3}} = \begin{cases} D_d u^n(x_i) & \text{if} |\nu| g(I)(x_i) > \theta \\ and & \nu > 0 \\ E_d u^n(x_i) & \text{if} |\nu| g(I)(x_i) > \theta \\ and & \nu < 0 \\ u^n(x_i) & otherwise \end{cases} \tag{3.16}$$

where D_d an E_d refer to the discrete version of Dilation and Erosion, respectively. *g(I)*

is the edge indicator function of Image I, u^n and $u^{n+\frac{1}{3}}$ represent the level-set curve at iteration n and $n+\frac{1}{3}$, respectively, and x_i represent a point in the curve u.

On the other hand, the equation 3.17 refers to the attraction force. Here, each point x_i of the curve u modified (or not) from the last step, is set to 1, 0 or is not modified, depending on the the gradient of the curve u in that point as wells the value of *g(I)*.

$$u^{n+\frac{2}{3}} = \begin{cases} 1 & \text{if } \nabla u^{n+\frac{1}{3}} \nabla g(I)(x_i) > 0 \\ 0 & \text{if } \nabla u^{n+\frac{1}{3}} \nabla g(I)(x_i) < 0 \\ u^{n+\frac{1}{3}}(x_i) & \text{if } \nabla u^{n+\frac{1}{3}} \nabla g(I)(x_i) = 0 \end{cases} \tag{3.17}$$

where $u^{n+\frac{1}{3}}$ and $u^{n+\frac{2}{3}}$ are the snake curve at iteration $n+\frac{1}{3}$ and $n+\frac{2}{3}$, respectively, x_i represent a point in the curve u and *g(I)* is the edge indicator function of Image I.

Finally, the equation 3.18 refers to the morphological smoothing operator and is the last step of an iteration process. Here, each point x_i of the curve u modified (or not) from the last step, is subject to the application of the morphological curve operator $SI_d \circ IS_d$, depending on the *g(I)* in that point.

$$u^{n+1}(x_i) = \begin{cases} (SI_d \circ IS_d)^{\mu} u^{n+\frac{2}{3}} & \text{if } g(I)(x) > 0 \\ u^{n+\frac{2}{3}}(x_i) & otherwise \end{cases} \tag{3.18}$$

where ,u^{n+1} $u^{n+\frac{2}{3}}$ are the snake curve at iteration *n+1* and $n+\frac{2}{3}$, respectively and x_i represent a point in the curve u. $SI_d \circ IS_d$ correspond to a morphological operation, known as morphological curve operator F. The parameter μ refers to the number of time this smoothing operator is applied by iteration.

This model has some advantages over the methods mentioned before, for example, this approach is faster, because the operators are fast. Also, it is more stable, because it use morphological operations instead of numerical[72]. As a result, the curve is not degraded, resulting in no need for re-initialization, meaning less computation burden[66]. Also, the initial curve is much simpler to define (ones inside the curve and zeros outside the curve), on contrary to the traditional active contour approach, in which the curve is parameterized.

Nonetheless, one of the main problems regarding this method is the choice of the initial level-set initialization, which, in turn, influences the time of computation. If the initial level-set is initialized far from the object to be segmented, more of time of computation is needed.

This method has been widely used in medical applications such as in breast tissue segmentation [73], spinal cord segmentation[74], for instance. One example of application of this method in breast ultrasound images is found in Figure 3.15. It shows the evolution of the initial level-set curve (Frame(0)) to the final curve (Frame(80)), where 80 is the number of iterations. The initial level-set was initialized inside the object to be segmented (red circle in the left image). To achieve the segmentation , the boundaries of the object

(breast) had to be denoted, which was possible by the application of the edge indicator. Furthermore, since the initial contour was set inside the object to be segmented, the balloon parameter was set positive, in order to inflate the initial contour.

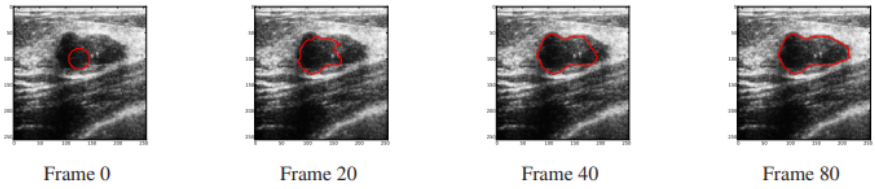

Figure 3.15: Example of application of morphological active contours in breast ultrasound images. This image represents the evolution of the initial level-set curve (red) (Frame 0) until the last level-set curve (Frame 80) [66].

3.1.7 Segmentation Evaluation metrics

Medical image segmentation is widely important and critical nowadays. Thus, segmentation of medical images with high precision methods are necessary in order to evaluate human anatomical structures.

Semi automatic or automatic segmentation methods have been applied in medical image analysis with the purpose of reducing the drawbacks of manual segmentation, such as the intra-observer and inter-observer variability errors.

The evaluation of the performance of these segmentation methods is very important and is usually done by some objective criteria. Among these, there are the Dice Coefficient (DC)and the Hausdorff Distance (HD) [75].

The first correspond to the amount of spatial overlap between the predicted region and the ground-truth region[76] and is mathematically represented in equation 3.19.

$$DC(X,Y) = 2\frac{|X \cap Y|}{|X| + |Y|} \tag{3.19}$$

where $DC(X,Y)$ is the Dice Coeffecient between X and Y, which represent the number of positive pixels/voxels on the ground-truth and predicted result, respetively.

In this metric, the values range from zero percent to one hundred percent. Zero percent means that both regions are not similar. One hundred percent means that both images match completely[48].

The second corresponds to maximum distance one has to travel between one point from one of the two set of points (X and Y, for example) to the closest point in the other set. The distance is mathematically represented in equation 3.20.

$$HD(X,Y) = max(hd(X,Y)), hd(Y,X)) \tag{3.20}$$

where *HD(X,Y)* is the Hausdorff Distance between X and Y, *hd(Y,X)* is the hausdorff distance between Y and X and *hd(X,Y)* is the hausdorff distance between X and Y. These are also called one-sided hausdorff distances.

The one-side hausdorff Distances are mathematically represented in equations 3.21 and 3.22. ,

$$h(Y, X) = \max_{y \in Y} \min_{x \in X} \|y - x\| \tag{3.21}$$

where *h(Y,X)* is the maximum distance between the closest points of Y to X and $\|y - x|$ is the euclidean distance between y and x.

$$h(X, P) = \max_{x \in X} \min_{y \in Y} \|x - y\| \tag{3.22}$$

where *h(X,Y)* is the the maximum distance between the closest points of X to Y and $\|x - y|$ is the euclidean distance between x and y.

In Figure 3.16, it is possible to see a representation of how to calculate the HD distance between two set of points X and Y(blue and red curves, respectively). In the image, the arrows represent the distances represented in equation 3.21 and 3.22, respectively. After computing these distances, it is necessary to calculates the maximum among these two and that's the Hausdorff Distance between these two sets.

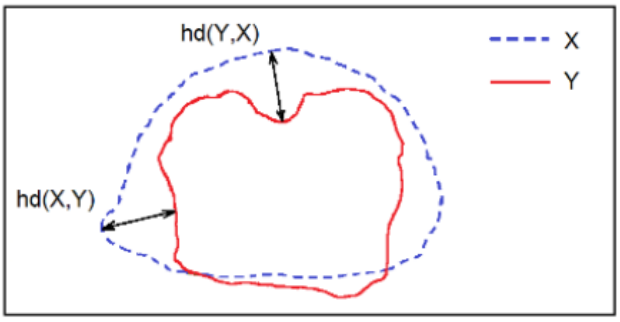

Figure 3.16: Representation of calculation of HD between two set of points X(dotted blue curve) and Y(red curve). The arrows correspond to both one-sided hausdorff distances [75].

In this metric, the values range from zero to infinite. Zero means that both sets share the same the borders. High values mean that both sets are distant from one another[48].

For segmentation purposes, it is desirable to have low values of HD and high values of DC.

4

Materials and Methods

This chapter presents a description of the materials and methods used in the present work.

4.1 Materials

4.1.1 Computer features information

This work was done on Windows Computer with the following settings: Processor AMD Ryzen 7 3700U with Radeon Vega Mobile and 16 GB of memory RAM.

4.1.2 X-ray image dataset

In this work, five X-ray images were used, which were found by searching online for X-ray images from DISH patients. Four of these are pathological and one is non-pathological. Also, the radiographs are coronal X-ray images with anterior-posterior views of the spine. Some of them include only thoracic vertebrae while others include both thoracic and lumbar vertebrae.

This set of images is good for the purpose of the work because, as said before, all images contain thoracic vertebrae, and, in most of them, these vertebrae pathological. As reported in chapter 2, the characteristics of DISH in anterior-posterior views of thoracic spine include ossifications in the right antero-lateral aspects of vertebral bodies, leaving the other lateral side without any manifestations of the disease. Hence, this type of images will be useful to understand if there is a difference in intensity values between these two sides and, ultimately, obtain a metric able to differentiate the pathological vertebrae from non-pathological, which is one of the objectives of this work.

Despite this advantage, the images have some features which surely will affect the performance of the segmentation and posterior analysis of the vertebrae. For example, some radiographs are from patients with deteriorated spines, due to DISH, and because of it, it is possible to visualize clips and metalic structures that give support to the spine. Moreover, some of the images have low-resolution.

The dimension of each image can be found in I.1 in Annex I.

4.1.2.1 Image 1

This image, shown in Figure 4.1, was retrieved from [77], by cropping it. It is a anterior-posterior X-ray image from a patient with DISH. It shows the thoracic spine (T9-T12) and lumbar spine (L1-L4). In this image, it is noteworthy the presence of ossifications in the right side of the following vertebrae: T9-L2.

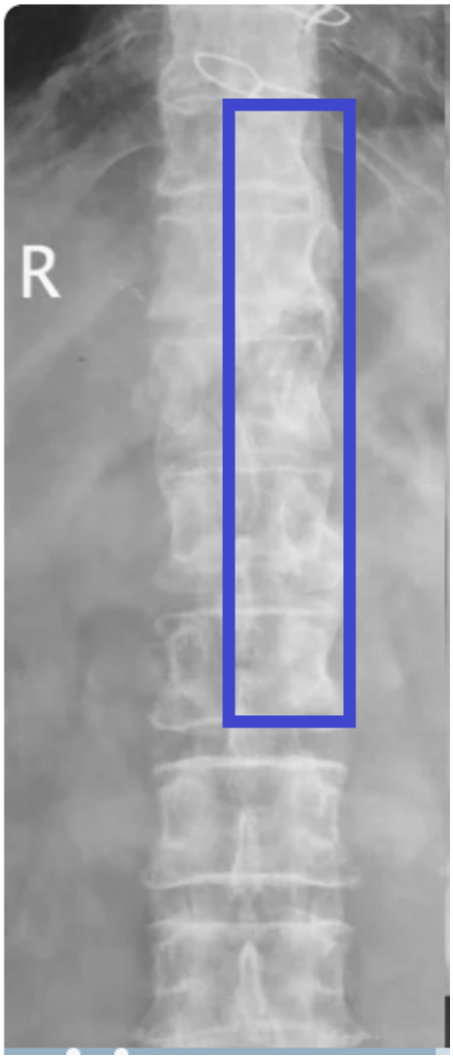

Figure 4.1: Anterior-posterior view of a patient with DISH. The blue rectangle surrounds the region of vertebrae where the ossifications originated by DISH are present [Adapted from [77]].

4.1.2.2 Image 2

This image, shown in Figure 4.2, was retrieved from [36], by cropping it . It is a anterior-posterior X-ray image from a 51-year-old man with DISH and it shows the thoracic spine (T7–T11). In this image, it is noteworthy the white arrows, which show penetrating areas of protruding disk material in flowing ossifications at multiple levels.

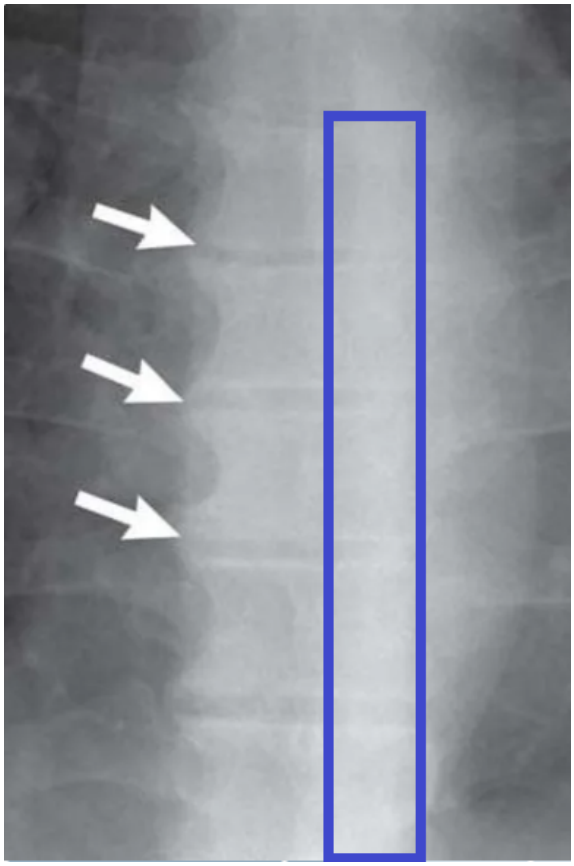

Figure 4.2: Anterior-posterior x-ray of 51-year-old man with DISH showing, with white arrows, areas of protruding disk material and, with the blue rectangle, the location of the ossifications [Adapted from [36]].

4.1.2.3 Image 3

This image, shown in Figure 4.3, was retrieved from [78] by cropping it. It is an anterior-posterior X-ray image from a 48-year-old woman with lower back pain and later diagnosed with DISH. By this time, there was no ossification or bone bridge formation in the lumbar section of the anterior longitudinal ligament. It contains vertebrae from thoracic spine (T11-T12) and lumbar spine (L1-L5).

4.1.2.4 Image 4

This image, shown in Figure 4.4, was also retrieved from [78], by cropping it. It is an anterior-posterior x-ray image from the same 48-year-old woman, fourteen years later, now aged 64. During this time, the patient was subject to three surgeries and this image was taken after the third. Also, the progression of ossifications in the anterior longitudinal ligament was very fast and the presence of ossifications in it spread to almost its extension: from the thoracic region to the sacral area. It contains vertebrae from thoracic spine (T11-T12) and lumbar spine (L1-L5).

Figure 4.3: Anterior-posterior x-ray image of 48-year-old woman without DISH[78].

4.1.2.5 Image 5

This image, shown in Figure 4.5, was also retrieved from [36], by cropping it, but it is not from the same person as Images 3 and 4. It is a anterior-posterior X-ray image from a 52-year-old man with DISH and it shows the thoracic spine (T2-T11). In this image, it is noticeable more than four contiguous ossified vertebrae (T7-T11) and this finding was important for DISH diagnoses. The quality of the image is not good, specially the lack of definition of the boundaries of vertebrae, which make the analysis of vertebrae very difficult.

4.1.3 Programming language

Images, specially medical images, are rich data sources. According to [79], in order to obtain the most of these data, it is required sophisticated software tools to deal with them. *Python* is one of most sophisticated programming language used in image processing. It is clear, concise and open-source and possesses a myriad of libraries available to deal with images and data. The following libraries were used for purpose of this work:

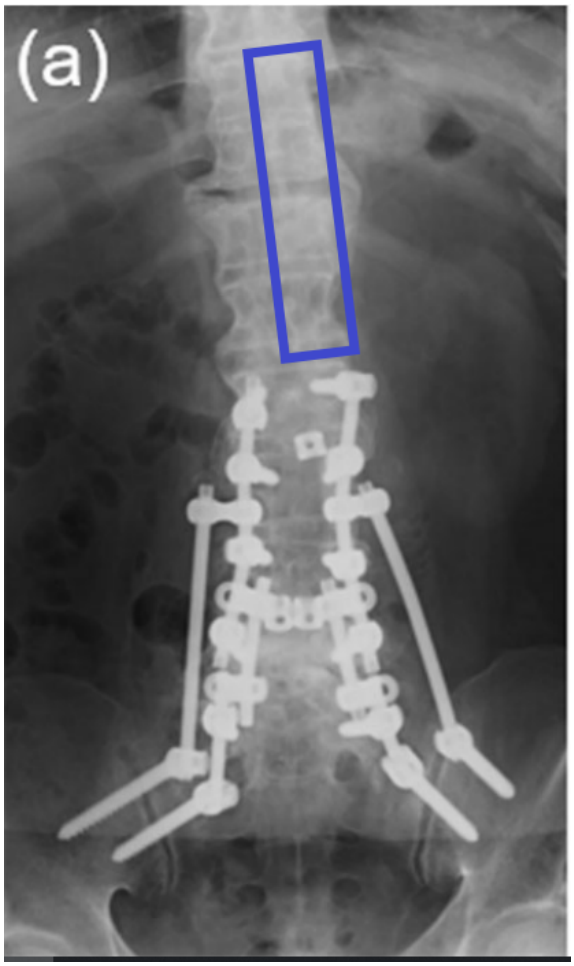

Figure 4.4: Anterior-posterior x-ray image from 48-year-old woman with DISH showing, with the blue rectangle, the ossifications of the AAL [78].

Numpy: It is a library used to manipulate arrays and provides efficient storage and manipulation of dense typed arrays or matrixes, like the images. Moreover, this library was useful in manipulating the data obtained from the analysis of intensities of vertebrae.

Skimage: This library provides high-quality and *easy- to-use* image processing algorithms which can be used for professional purposes[79]. By using this library, it was possible to load images, convert them to grayscale value images and pre-processing them. Also, this library has plenty of segmentation algorithm which can be applied to images such as algorithms of the active contour family.

Pandas: It is a widely used library in data science, providing tools to make the data more organized and obtain information, for example, statistics [80].

Scipy: It is a library used in scientific programming, which can be used to solve mathematical problems. It can also be applied in the analysis of signals, to characterize them, for example, find its peaks.

Matplotlib: It is a library used with the purpose of displaying the images as well as the segmentations proposed by the algorithm.

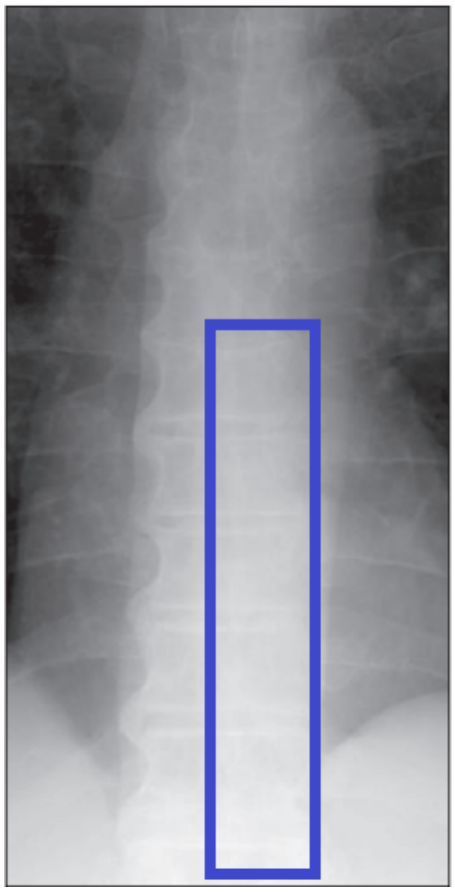

Figure 4.5: Anterior-posterior x-ray image from 52-year-old man with DISH showing, with the blue rectangle, the location of the four contiguous ossified vertebrae (T7-T11) [Adapted from [36]].

4.2 Methodology

Based on the characteristics of DISH in thoracic vertebrae, it was proposed the development of a methodology able to segment the vertebrae and capture their specific morphology, with the ultimate goal of analysing them and find a metric able to differentiate DISH from NON-DISH vertebrae.

To achieve it, two different methodologies were used: one for the segmentation of vertebrae and another for their analysis. The methodology for the segmentation of vertebrae is described first and three main steps are required to achieve the final result: Loading and conversion of the image into an grayscale value image array. Then, the pre-processing step, to remove noise of radiographs, enhance important vertebrae features, such as the edges. Finally, the processing step, in which the segmentation algorithm is applied.

The methodology applied for the analysis of each vertebra is described at the end of this chapter and three main steps are also required. After the segmentation, each vertebra is divided in nine squares in order to be possible the analysis of the corners, where the disease occurs. Then, the corners are analysed based on their intensities values. Lastly,

based on these values, it is calculated two metrics to verify if can be used to differentiate pathological from non-pathological vertebrae.

4.2.1 Methodology for segmentation

4.2.1.1 Load and conversion of the image

The images used in this work were loaded into an array using the *skimage* library. After this, the images were transformed to grayscale values. This is achieved by using the skimage library function *rgb2gray*.

4.2.1.2 Image pre-processing

X-ray images were subject to a pre-processing phase. Firstly, the noise were removed. Then, it was necessary a contrast enhancement phase, in order to highlight the edges of vertebrae. Finally, the last step of this phase was the application of the Inverse Gaussian Operator, which is critical for the application of the morphological active contour segmentation algorithm.

4.2.1.3 X-ray image denoise

The images were subject to a noise removal step. Here, it was used the function created by [18] for X-ray images horizontal noise removal, which removes noise acquired during he acquisition process of radiographs.

This function starts by an initial contrast enhancement phase, by applying the skimage histogram equalization function *equalize_ adapthist*, with three arguments: image, *kernel _size*, *nbins*, where image is the image to be processed, the *kernel size* is the kernel used to enhance the edges and the *nbins* correspond to the number of bins used for the histogram. The parameters chosen were according to the characteristics of the image dataset used in this work: the original images were decoded in 8 bits and 256 was suitable for being the number of bins. For the *kernel size*, it was chosen 113. In order to get a good contrast, and taking into account the characteristics of the dataset images near boundaries, it was not reasonable to use small sized kernels, because this would enhance small and non-important features of the image, so 113 was chosen.

After this, the function computes the mean of the image, along the horizontal axis, and applies a moving average filter. Then, subtracts the mean with the result of this filter, obtaining a vector containing the peaks of the horizontal noise. These are then found by the application of *skimage* function $find\_peaks$, which return the vertical coordinates of the noise points.

At the end, it is applied a uniform filter or *mean* filter. This filter replaces the value of a pixel by the mean of the neighbouring pixel, from the *scipy* library, which is used to remove the horizontal noise, essential to remove it from the vertebrae, specially at the edges, which will be very important in this work. Then, by using the information

of the coordinates of the peaks, the horizontal noise intensity in the original image is replaced by the correspondent values in the image resultant from the application of the uniform filter. The result of the application of this function for Image 1 is seen in Figure 4.6. As it is possible to see, the contrast of the original image (on the right) increased (on the right), specially at the edges of the vertebrae, Also, grey-color rectangles are shown, which represent the horizontal noise removed from the image on the left (blue arrows and rectangle).

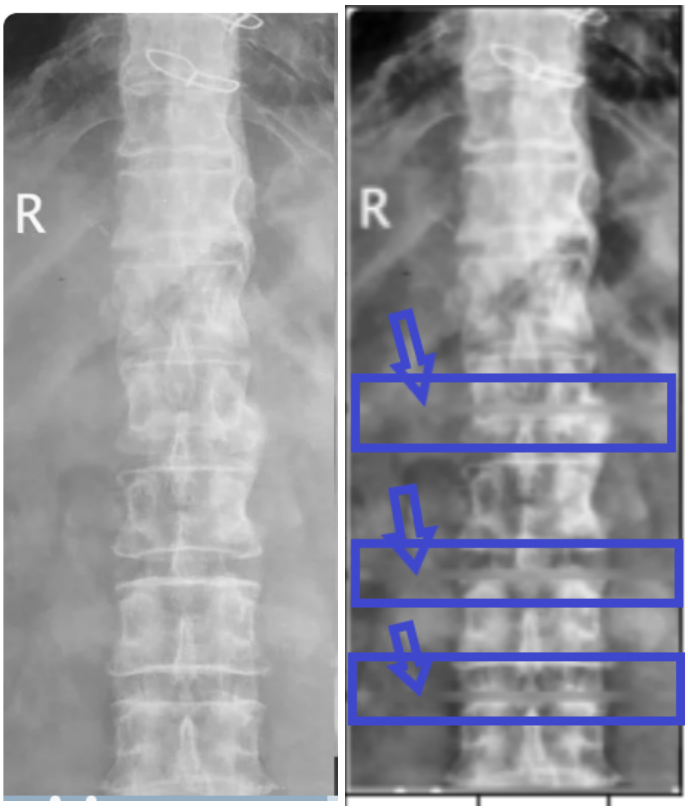

Figure 4.6: Example of application of image noise removal function:(Left image)Before removal and (Right image) After removal.

4.2.1.4 Vertebrae edges enhancement

After the removing the noise, there was another contrast enhancement phase because this work is widely dependent on the edges of vertebrae, and the DISH vertebrae boundaries can be very ambiguous near the boundaries. To accomplish this, it was used the same function *equalize_ adapthist*, with the same values for parameters: *kernel _size*, *nbins*. Figure 4.7 shows the application of this step on the image on the left, resulting in the image on the right. The edges of vertebrae were, once again, the main feature to be enhanced, resulting in more contrast at those regions. This was important for the next pre-processing step, which aims at constructing an image to be applied to the morphological geodesic active contour.

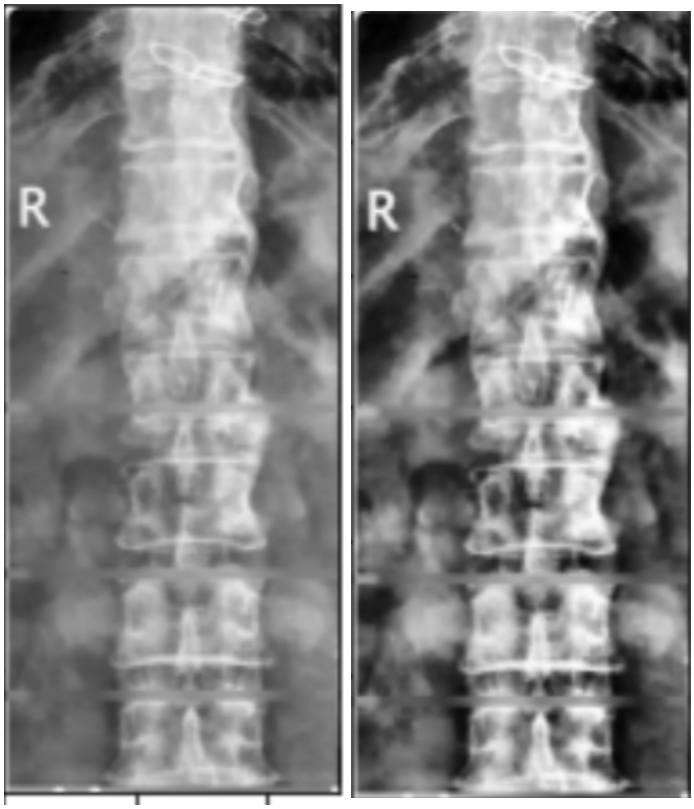

Figure 4.7: Example of application of image contrast enhancement: (Left image) Before enhancement and (Right image) After enhancement.

4.2.1.5 Application of the Inverse Gaussian operator

After this two steps, it was necessary to construct an image able to be applied to the morphological active contours algorithm. The efficiency of this algorithm is highly dependent on this image. Then, to construct this image, the function *inverse_gaussian_gradient* from *skimage.segmentation* library was used in order to highlight the edges of vertebrae. The theoretical background of this function can be found in chapter 3.

This function requires three arguments, according to the following example:

skimage.segmentation.inverse_gaussian_gradient(image, alpha, sigma)

where image is the image after the contrast enhancement phase, the α parameter controls the steepness of inversion and σ is the standard deviation of the Gaussian filter.

In the present work, the following parameters were used:

inverse_gaussian_gradient(image after contrast enhancement,80,3)

The α parameter was set 80. As said before, this parameter controls the steepness of the inversion of gaussian gradient. When choosing this parameter, there is a trade-off between low-values, which would cause the regions ear the edges of vertebrae not to be strong enough to be found by the algorithm, and high values, which would cause the inversion

to be sensitive to every point in the image with high gradient (i.e, noise or local minima). The σ was set 3 because the goal was to highlight the edges of the vertebrae and bigger values would smooth the edges in such a way that the segmentation algorithm would not be possible to find the right edges. Also, with smaller values, although it would enhance the edges of vertebrae, they would not be strong enough concerning the environment, and the algorithm would possibly stop at local minima at the surroundings. The image before application of the Inverse Gaussian operator (left image) and the image after the application (right image) are shown in Figure 4.8.

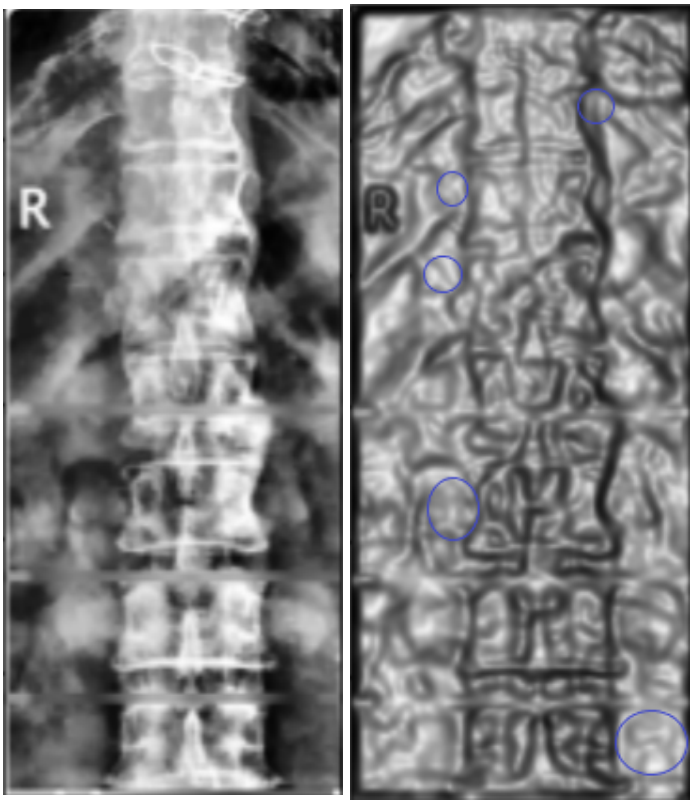

Figure 4.8: Example of application of inverse gaussian gradient: Before application (Left image) and After application (Right image). The right image also shows, with blue circles, the element that will be removed in the next step of pre-processing.

As it is possible to see in the right image, the edges of vertebrae are represented as dark pixels, which will be used as image forces for the morphological active contour to push the curve to this edges.

However, this image has many unnecessary elements (surrounded by the blue circles), specially near the edges of the vertebrae. These could interfere with the evolution of initial level-set curve, making it stop at those structures. Thus, these elements were eliminated. To do so, it was computed it's histogram and it was found the bin with the most pixels (threshold), by visual inspection. This bin is marked in red in the histogram found in Figure 4.9 and is, approximately, 0.65. Then, each bin value bigger or equal than this was assigned to 1. The result is shown in Figure 4.10. The use of smaller values would

probably eliminate important features of the image (i.e, edges of the vertebrae, which are represented by darker pixels in the image), thus, it was chosen a bin value capable of removing these unnecessary pixels, with minimum interference with the vertebrae edges.

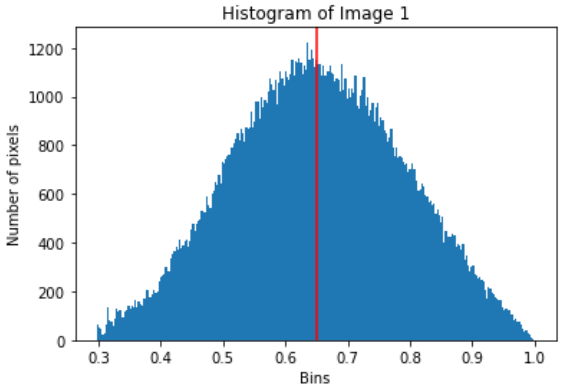

Figure 4.9: Histogram of the image after the inverse gaussian gradient was computed showing, with a red line, the bin with most pixels.

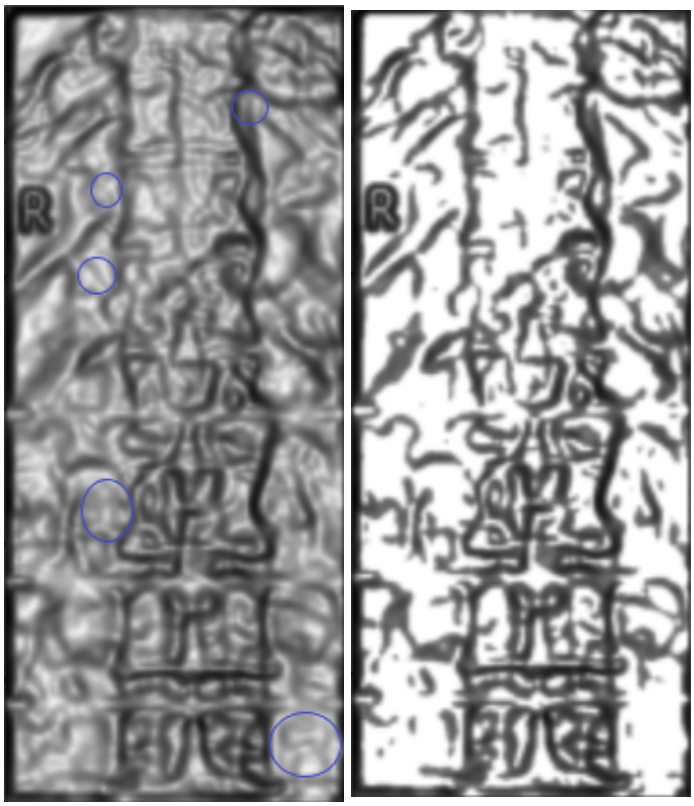

Figure 4.10: Removal of unnecessary pixels. (Left Image): Before. (Right image) After.

The final image was then considered input for the morphological geodesic active contours for segmentation, which uses this image as image force to lead the initial level-set curve to the desired object, in this case a vertebra.

4.2.1.6 Morphological Geodesic Active contours

In order to provide the segmentation for the vertebrae, it was used the morphological geodesic active contours algorithm. The *skimage* library from *Python* has a function which enables one to implement this segmentation algorithm. The function with its most important arguments is represented as follows:

$$morphological\_geodesic\_active\_contour(gimage, num\_iter, init\_level\_set, smoothing, threshold, balloon)$$

,where *gimage* represents the image to be segmented after being pre-processed and computed the $inverse\_gaussian\_gradient$, num_iter is the number of iterations, the $init\_level\_set$ is the initial level set, the smoothing argument is the number of times the smoothing operator is applied per iteration, the threshold is a maximum value of an image to be considered an edge and the balloon force is the guidance force for the contour in non-informative areas, where the gradient is very small to push the contour to the edges.

The result of application of this function is the final segmentation and the final level-set. The values for these parameters were chosen based on the segmentation quality, assessed by visual inspection of the segmentation result, and the time of computation:

$$morphological\_geodesic\_active\_contour(gimage, num\_iter = 300, init\_level\_set, smoothing = 20, threshold = 1, balloon = -1)$$

For $num\_iterations$, 300 was chosen because the images are of small shape and the time of computation for this number of iterations is small (5 minutes). Also, with this value, it was possible to achieve a reasonable segmentation. On the other hand, the smoothing parameter was set to 20 because DISH images present very high intensities near the edges of vertebrae, and, with this value, it is possible to diminish the effect of those intensities on the final segmentation. The threshold parameter was set to 1 in order to avoid the contour, as it evolves, to stop at weak edges, and stop at the borders of vertebrae. Finally, the balloon force parameter was set to -1 because the initial level-set incorporates the region to be segmented and the contour must shrink until the edges of that region.

Concerning the initial level set, this is a vertebra dependent argument. The initial contours used in this work were from the algorithm created by [18]. However, since it was not possible to get the contours for the dataset images used in this work, the contours are from a non-pathological image with a different size (5882x2024). Due to this fact, it was necessary to match the contours to the correspondent vertebrae in the dataset images. To accomplish this, firstly, each contour was centered to the correspondent vertebra, as shown in Figure 4.11 (top left image). Then, it was applied affine transformations to this contour in order to place it in the surroundings of the vertebra, as seen in the top right image in Figure 4.11. After that, it was computed the initial-level-set, as shown in the bottom left image. This is done using the *skimage* function *polygon*, which take as input the coordinates of the centered contour and return the pixel coordinates of the polygon.

Then, it is created a blank mask with the same size as the original image. The coordinates are then used to create a binary mask, which is the initial level set: The pixels inside are set to 1 and outside are left 0. Then the morphological geodesic active contour algorithm was applied and the segmentation result is found in the bottom right image.

After obtaining the segmentation result, the course of the algorithm depends on the result of the last step. If the segmentation capture the specific morphology of the vertebra, such as in the case of the top right image in Figure 4.12, the search for the contour stops. If not, as in the case of the bottom right image in Figure 4.12, it is necessary to change the initial level-set location, by using affine transformation, such as translation and rescaling.

In this case, the visual inspection of the left superior corner reveals that it is not well segmented, thus, there is a need to displace the initial level set to the left (negative translation) and also increase size (positive rescaling) (bottom left image), in order to segment that region. Both initial contours can be seen in left images in Figure 4.12. Although not very noticeable, the initial contour (blue) represented in the top left image is slightly bigger and displaced to the left, concerning the initial contour represented in the bottom left image. As a result, the segmentation results, which are represented in green in the correspondent right images, are different. This image shows that the segmentation result is quite sensitive to the initial position of the initial contour.

4.2.1.7 General overview of Segmentation methodology

The general workflow of this methodology is found in Figure 4.13. Firstly, the images are transformed to grayscale value, by using the aforementioned *skimage*functions. Then, horizontal noise from the images are removed and the contrast is enhanced, specially near the edges of vertebrae. The next step is the computation of the Inverse Gaussian Gradient, by using the *skimage* correspondent function. This returns an image with the edges of vertebrae highlighted, necessary for the application of the morphological geodesic active contour. However, this image has unnecessary pixels, which are removed by, firstly, computing the histogram and find, by visual inspection, the bin with the greatest number of pixels. Next, it is the segmentation phase. Here, the algorithm proposed here uses the contour for a specific vertebra, obtained by using the algorithm proposed by [18], and uses affine transformations to match the initial contour to the vertebra to be segmented. Then, with this transformed contour, it is calculated the initial level-set, which is a binary image, and comprises the desired object. After this, based on the parameters chosen and the image obtained from the pre-processing phase, this curve is subject to a series of morphological operations, which transforms it, until reaching the edges of the object(s).

4.2.2 Methodology for analysis of vertebrae

The ossifications caused by DISH influences the intensity values in a X-ray image. In reality, areas with bigger ossification translates into more intense pixels in X-ray images, due to

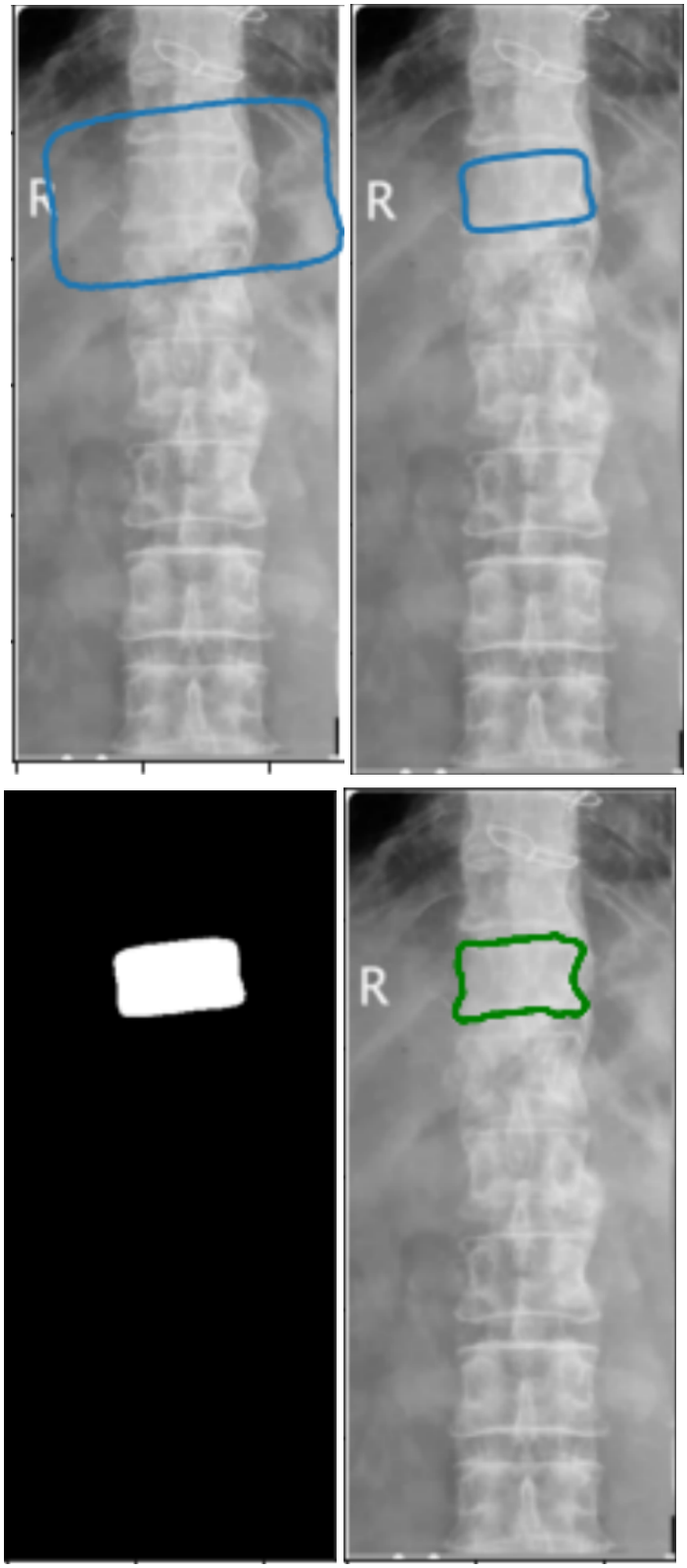

Figure 4.11: Steps needed to obtain the segmentation of a vertebra. (Top left image) image: Centering of the average contour obtained from [18].(Top right image): result of the application of affine transformations to the contour on the top left image. (Bottom left image): Initial level set used in the morphological active contour algorithm. (Bottom right image): Segmentation obtained for the vertebra.

higher x-ray absorption and, therefore, fewer x-ray photons reaching the sensor/image plane [81].

Also, DISH mainly manifests in the corners of the vertebrae and there is a preferential side for manifestation, in the thoracic region. Figure 4.14 shows an anterior posterior x-ray image of a column presenting DISH characteristics. The right-hand side vertebrae display hyperintense regions, when compared to the left-hand side corners. The white arrows correspond to disc protrusion (hernitation), probably caused by the bridging ossifications in the right side of the vertebrae.

Taking this into account, it was proposed to analyse each vertebrae in terms of intensity values, in order to find insight able to help the diagnoses of DISH. Each vertebra was divided in 9 squares, as shown in the Figure 4.15, and the corner squares (blue squares) were considered for evaluation.

For each one of those corner squares, it was calculated the average intensity value and computed the histograms distributions. Also, in order to evaluate the difference between the pathological side and the non-pathological, it was also calculated the ratios seen in equations 4.1 and 4.2, assuming a symmetry between the two sides of the vertebra. In the first equation, the numerator stands for Left superior corner average intensity value (LS) and the denominator stands for Right superior corner average intensity value (RS). Regarding the second equation, the numerator stands for Left inferior corner average intensity value (LI) and the denominator stands for Right inferior corner average intensity value (RI). During these calculations, it was necessary to ensure that each corner had, approximately, the same number of pixels as the other.

$$Ratio1 = \frac{LS}{RS} \tag{4.1}$$

$$Ratio2 = \frac{LI}{RI} \tag{4.2}$$

4.2.2.1 General overview of vertebrae analysis methodology

The general workflow of this methodology is found in Figure 4.16. Firstly, the after getting the segmentation results of a vertebra, the vertebra is then divided in nine squares, however, only the corners are considered for evaluation. Then, it is computed the histograms of those corners as well as the average intensity values. Based on the assumption of Gaussian-like shape of the distributions and the symmetry of vertebrae, two ratios are calculated: LS/RS and LI/RI.

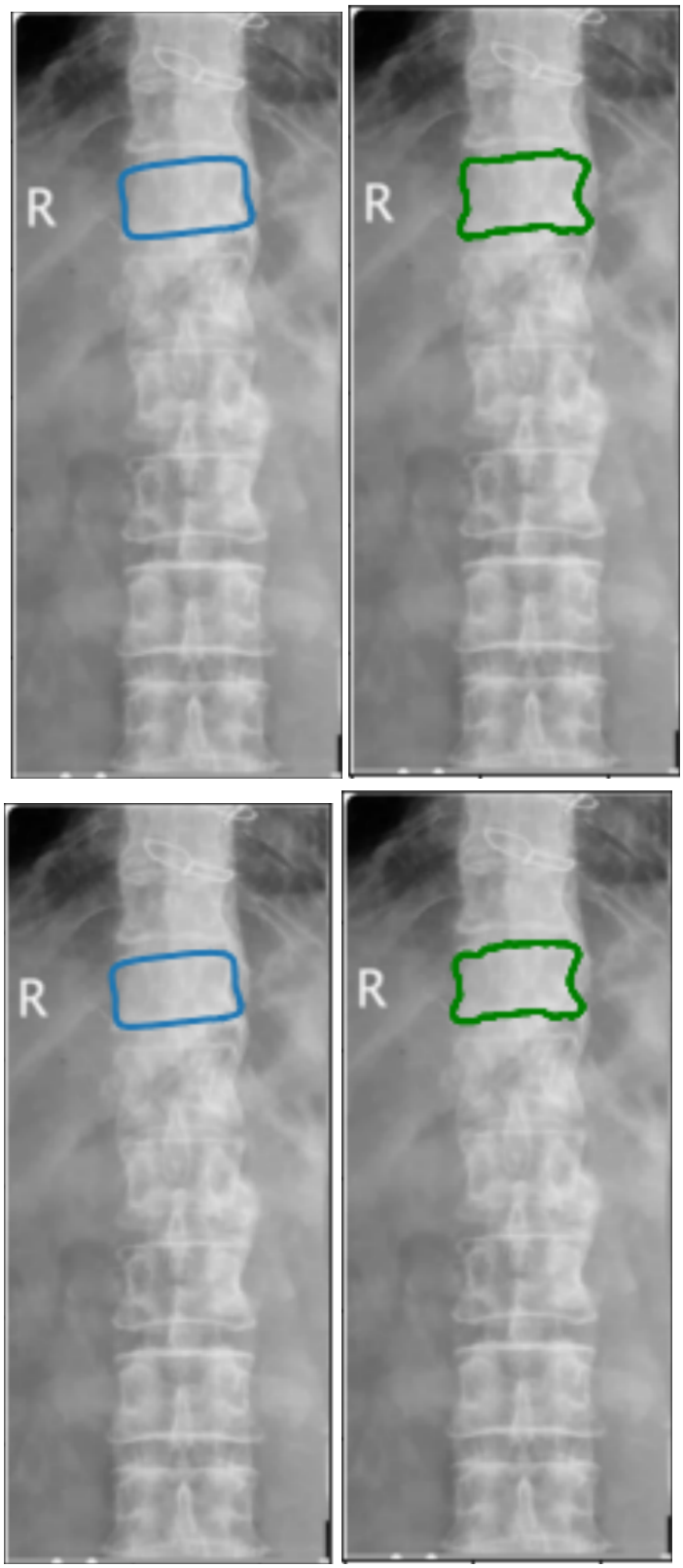

Figure 4.12: Segmentation results of the algorithm depending on the position of the initial contour.(Top images): (Left) initial contour and (Right) adequate segmentation result (green). (Bottom images): initial contour (Left) and (Right) the not reasonable segmentation result.

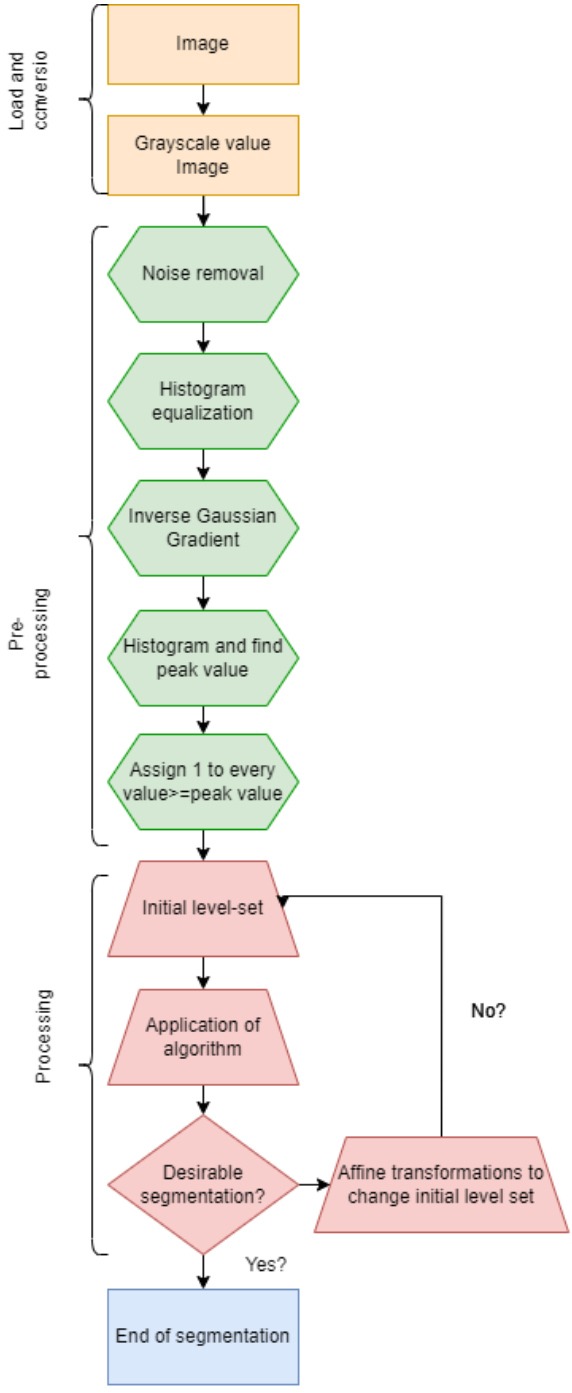

Figure 4.13: General flowchart of the methodology applied for segmentation of vertebrae.

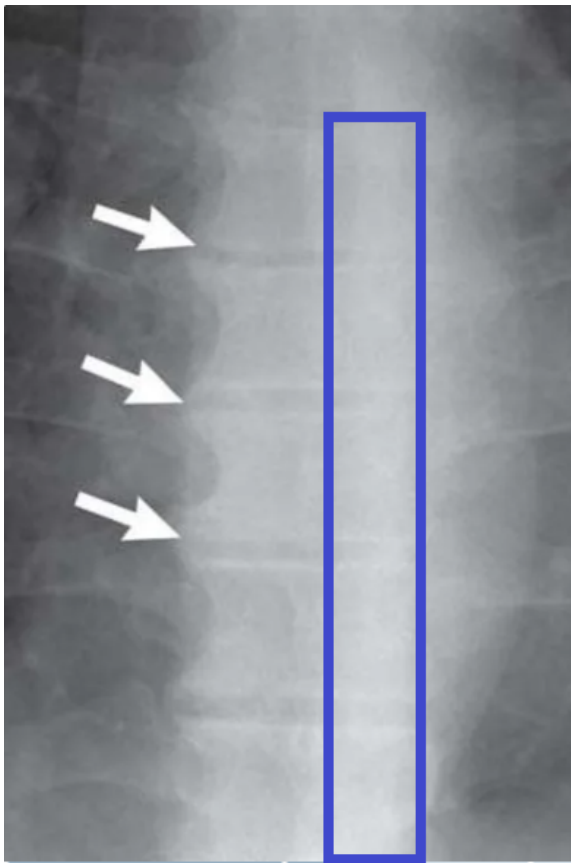

Figure 4.14: Image of a patient with DISH, showing a preferential side (more white) for disease manifestation (blue rectangle box) [Adapted from [36]].

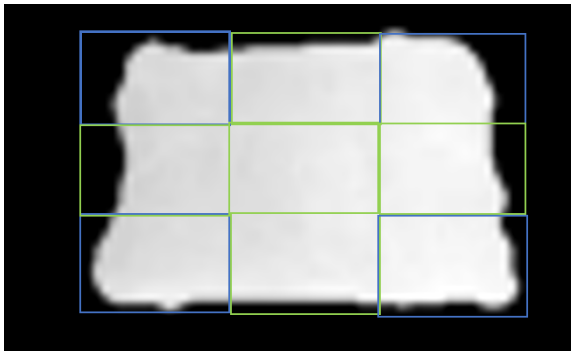

Figure 4.15: An example of division of a vertebra in 9 squares (blue and green squares), where the blue ones represent the corners.

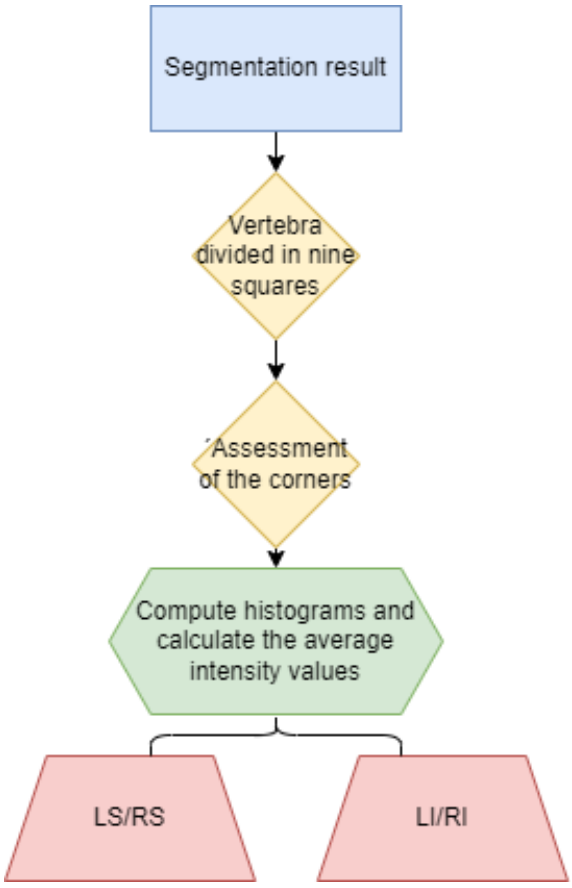

Figure 4.16: General flowchart of the methodology applied for the analysis of vertebrae.

5

Results and discussion of segmentation evaluation

5.1 Results

As said before, [18] developed vertebrae models with the help of experts manual annotations. In his work, each image used held two manual annotations, Annot1 and Annot2, to be more precised, which were built by experts in the area. It is also said in its work that after the models are created as well as the algorithm, a third expert organized the Annot 1, Annot2 and the results of the algorithm built in terms of segmentation accuracy. The results showed that the Annot1 held the highest score.

Thus, in order to evaluate the segmentation performance of this work, Annot 1 was used as the ground-truth segmentation. The DC and HD were evaluated and compared for the following pair of segmentations: Annot1/Annot 2, Annot1/ algorithm of [18] and Annot1/this algorithm. The results allow one to evaluate the similarity of each segmentation to the segmentation Annot1.

To accomplish this evaluation, two images from the dataset used by [18] were selected. These images are represented in Figure 5.1. The correspondent annotations can be found in Annex II. The methodology used was the same as described in 3.1.7. However, there was slight difference in the parameters of the morphological active contours: the number of iterations was changed to 30 and the smoothing operator was changed to 6.

These images had to be, firstly, downsized, in order to make it possible to get a segmentation result in a short number of iterations and, therefore, in short time. By visual inspection of the segmentations, it was possible to get a good specific segmentation of the vertebrae in 30 iterations. Also, on contrary to the dataset images used for evaluating in vertebrae, the images shown in Figure 5.1 are less noisy. Therefore, the smoothing operator needed not to be big, so 6 was chosen for allowing, as well, get a good and smooth segmentation result.

The results of these calculations are summarized in Tables 5.1 and 5.2.

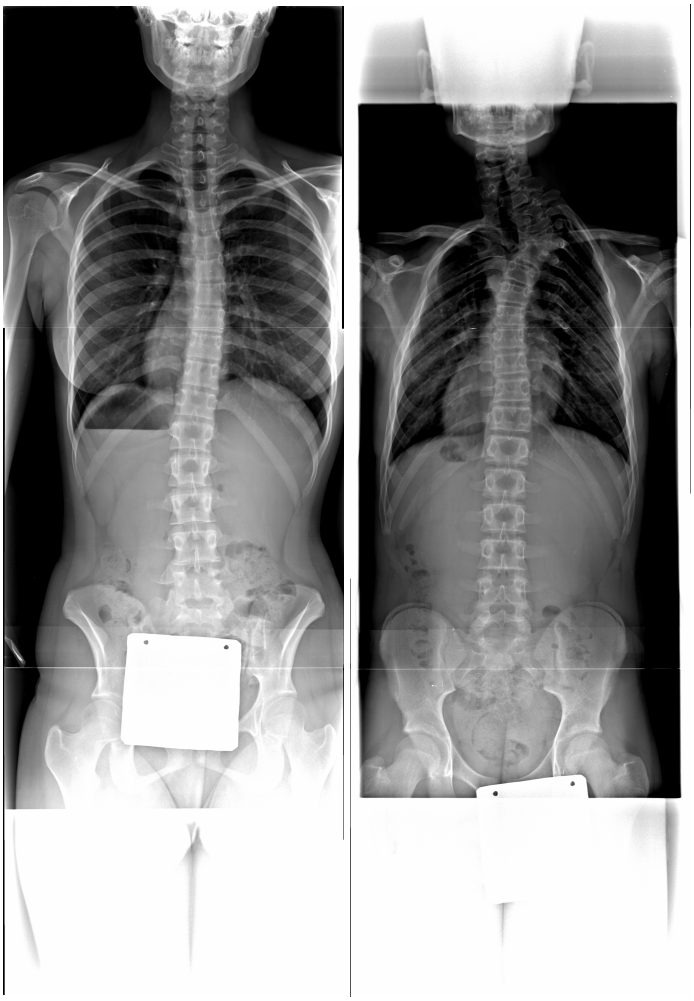

Figure 5.1: Images used by [18] to construct the algorithm and were used in these work for segmentation evaluation. Left image was labeled as Image 6 and the right image as Image 7.

A summary of the results is found in Figures 5.2, for Image 6, and 5.3, for Image 7.

5.2 Discussion

According to the results in Tables 5.1 and 5.2, the algorithm proposed here provides good segmentation results for both Image 6 (DC 93.45±1.72%, HD 3.78±1.15 mm) and Image 7 (DC 92.915±2.04%,HD 3.51±1.23mm). Also, it has better results than[18] for both Image 6 (DC 90.30±2.84,HD 4.31±0.80mm) and Image 7 (DC 91.630±3.1881%,HD 3.90±1.86mm).

According to these results,the algorithm proposed here brought an improvement to the segmentation presented by the algorithm developed by [18].

Comparing the results with Annot1/Annot2,this has better results for both Image 6 (DC 94.70±1.67%,HD 2.43±0.62mm) and Image 7 (DC 94.91±1.65%,HD 2.48±0.53mm).

Despite the results showing that Annot2 has a bigger similarity with Annot1, the difference is not very significant. As seen in 5.2 and 5.3, there is bigger intersection of

	Annot1/Annot2		Annot1/Ruben		Annot1/Algorithm	
Vertebra	DC(%)	HD(mm)	DC(%)	HD(mm)	DC(%)	HD(mm)
L4	97.37	1.59	91.35	4.64	93.56	5.83
L3	93.83	2.76	91.64	5.73	93.48	4.54
L2	97.78	1.55	92.65	4.04	95.51	2.40
L1	94.38	2.44	94.53	3.65	91.68	4.37
T12	94.80	2.08	89.78	5.39	95.35	4.02
T11	94.95	3.28	86.14	4.6	92.53	3.64
T10	93.07	3.35	91.56	3.11	95.75	1.86
T9	94.59	2.24	89.84	3.98	93.43	4.11
T8	92.84	2.25	85.11	4.15	92.80	2.85
T7	93.43	2.76	90.35	3.83	90.43	4.13
$\overline{x}$	94.70	2.43	90.30	4.31	93.45	3.78
σ	1.67	0.62	2.84	0.80	1.72	1.15

Table 5.1: Segmentation evaluations metrics, DC and HD, for each vertebra from Image 6.

	Annot1/Annot2		Annot1/Viegas		Annot1/Algorithm	
Vertebra	DC(%)	HD(mm)	DC (%)	HD(mm)	DC(%)	HD(mm)
L4	97.37	2.68	87.54	7.27	91.28	6.09
L3	95.20	2.64	94.73	3.55	96.37	2.45
L2	96.58	2.24	91.58	3.79	92.26	3.96
L1	95.93	3.24	86.73	6.24	93.09	3.34
T12	95.20	2.62	87.55	5.52	92.94	3.82
T11	96.64	2.10	92.06	3.10	93.95	2.57
T10	91.35	3.30	94.06	1.90	95.44	1.85
T9	94.53	1.90	94.27	2.59	93.35	2.57
T8	96.22	1.56	94.63	1.73	90.49	4.32
T7	93.60	2.78	93.15	3.29	89.96	4.09
$\overline{x}$	94.91	2.48	91.63	3.90	92.92	3.51
STD	1.65	0.53	3.19	1.86	2.04	1.23

Table 5.2: Segmentation evaluations metrics, DC and HD, for each vertebra from Image 7.

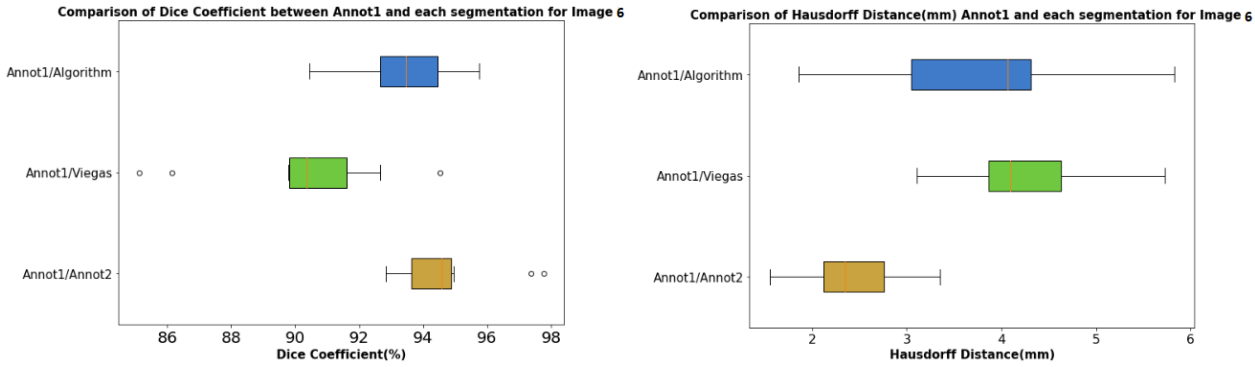

Figure 5.2: Graphical comparison between Annot1/Annot2 and Annot1/Viegas and Annot1/Algorithm for Image 6.

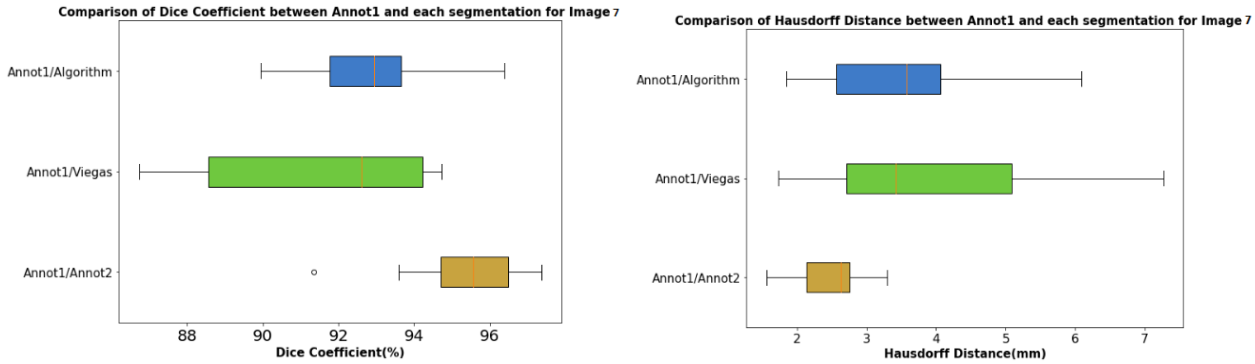

Figure 5.3: Graphical comparison between Annot1/Annot2 and Annot1/Viegas and Annot1/Algorithm for Image 7.

values of DC between Annot1/Annot2 and Annot1/Algorithm in both images, being Image 6 the one with greater intersection. This means that the proposed algorithm performance comprises the range of intervariability between experts, being similar to both.

Regarding HD, in both images, Annot1/Annot2 had better results. Despite this, the results for Annot1/Algorithm are quite similar to Annot1/Annot2, specially for Image 6, because, as shown in Figure 5.3, the range of results Annot1/Algorithm incorporates practically the variability of results of Annot1/Annot2. Hence, it is possible to state that both segmentations provided similar results.

6

Results of vertebrae segmentations and analysis

This chapter presents the segmentations provided by the algorithm for some vertebrae from each image and also the correspondent histograms. The goal here is show the variability of segmentation results obtained for each image, thus, only a few vertebrae were chosen. At the end of presenting the segmentations in each image, a table containing the intensity values for each vertebra in each image and the corresponding ratios is presented as well as a graphical representation of the ratios for each image.

At the end of this chapter, a general overview of the ratios from all vertebrae analysed is presented.

6.1 Segmentation results for vertebrae in each Image

6.1.1 Image 1

In this part of this chapter, the segmentation results for some vertebrae from the image shown in Figure 4.1 is presented. The remainder of the segmentations is found in III, in section III.1.

6.1.1.1 T10 vertebra

Here, the analysis of vertebra T10, presented in Figs. 6.1 to 6.3, aims to show the behaviour a vertebra, in which DISH is present.

Figure 6.1 shows the initial-level set used for the segmentation of the T10 vertebra from Image 1 and the concomitant segmentation.

Figure 6.2 displays the corners of T10 and the correspondent histograms.

Figure 6.3 displays all four corners' histograms, for visual comparison.

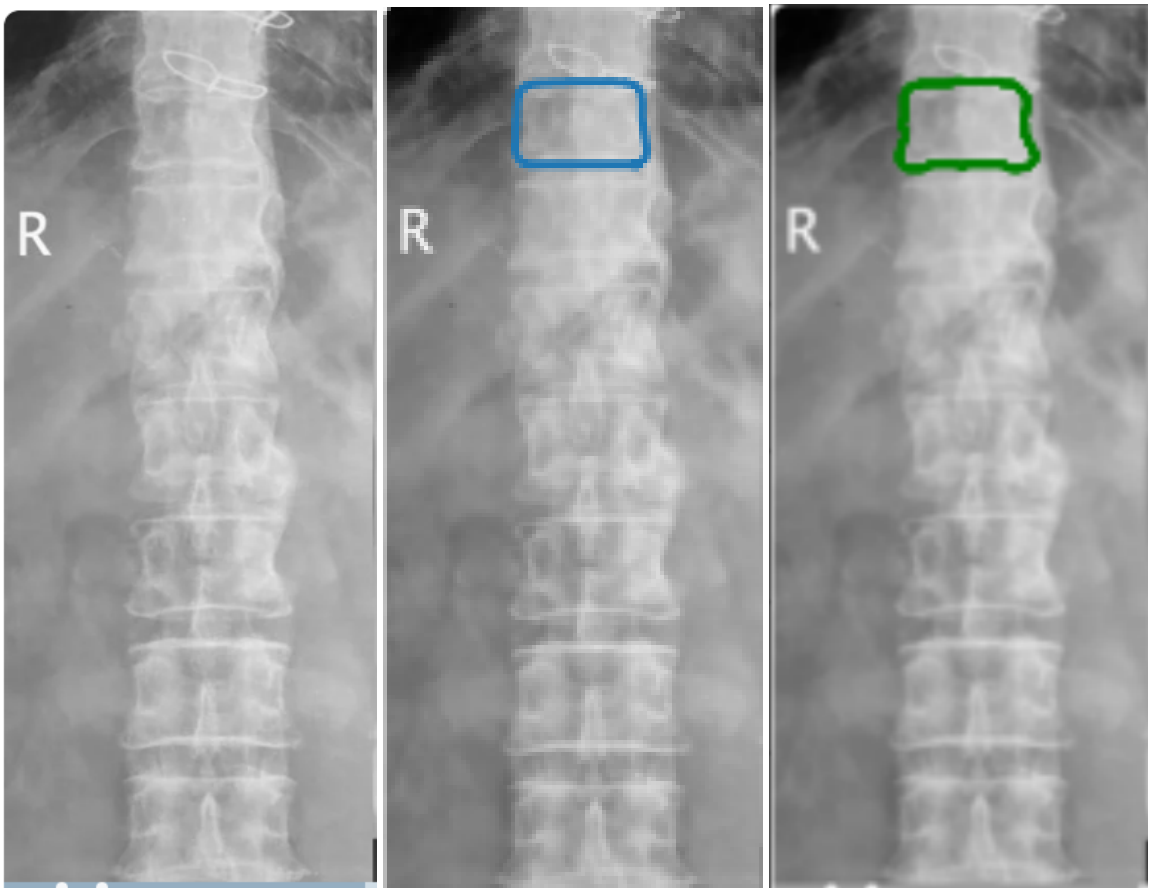

Figure 6.1: Initial level-set and segmentation result for T10 from Image 1.Image on the left: Original image; Image on the middle: Initial level-set (blue curve) used for segmentation of that vertebra; Image on the right: Segmentation result(green) for the correspondent vertebra.

6.1.1.2 L1 vertebra

Similar to the previous section, the vertebra L1, from Image 1, is now analysed, and presented in Figures 6.4 to 6.6. This analysis aimed at illustrating a different kind of behaviour in the absence of DISH.

Figure 6.4 shows the initial-level set used for the segmentation of the L1 vertebra from Image 1 and the concomitant segmentation.

Figure 6.5 displays the corners of L3 and the correspondent histograms.

Figure 6.6 displays the corners' histograms, for visual comparison.

6.1.1.3 L3 vertebra

In this section, the analysis of vertebra L3, from Image 1, presented in Figures 6.7 to 6.9, aims to illustrate a different type of behaviour, occurring in the absence of DISH.

The initial-level set used for the segmentation of the L3 vertebra from Image 1 and the concomitant segmentation are shown in Figure 6.7.

Figure 6.8 displays the corners of L3 and the correspondent histograms.

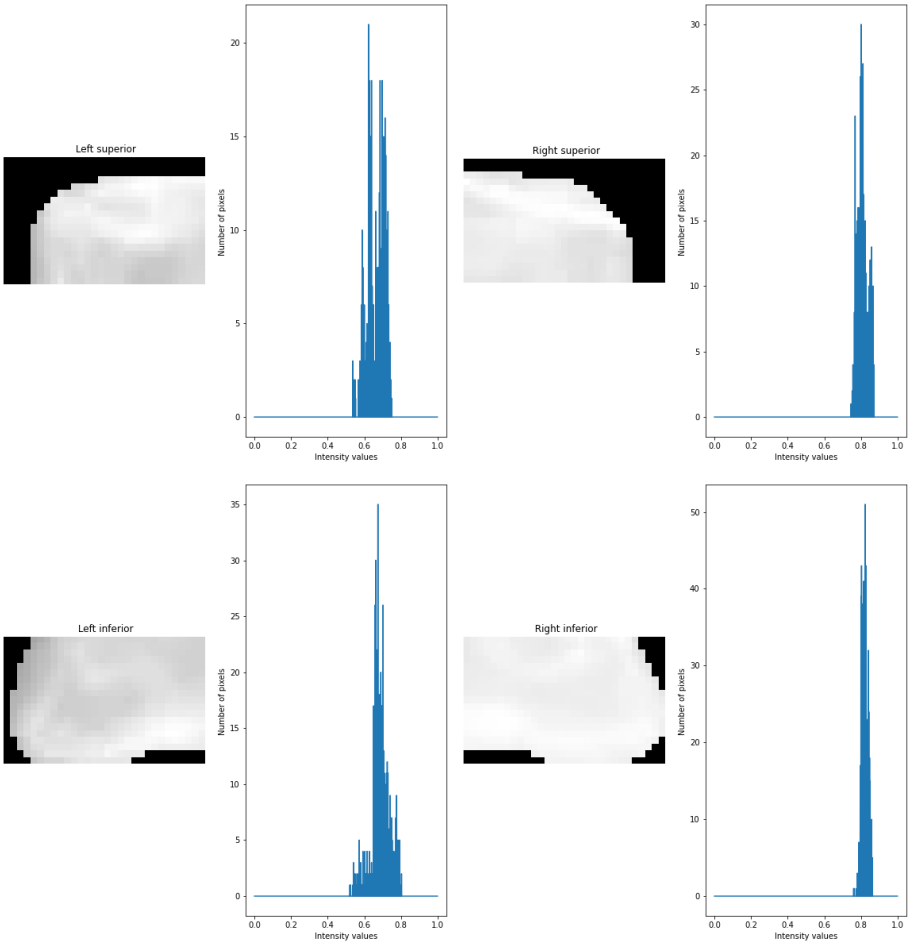

Figure 6.2: Comparison of each corner and its histograms for T10 vertebra from Image 1.

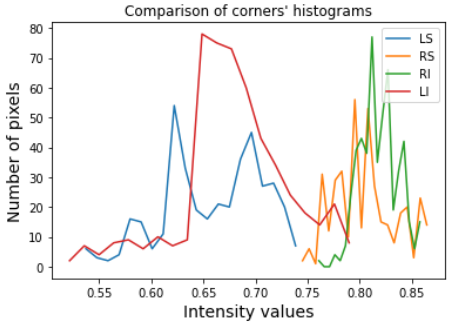

Figure 6.3: Comparison of all corners' histograms for T10 from Image 1, showing the difference between right side (green and orange curves) and left side of vertebra (red and blue curves)

Figure 6.9 displays the corners' histograms, for visual comparison.

6.1.1.4 L4 vertebra

In this section, as done for the previous vertebra, is presented the analysis of vertebra L5, from Image 1, presented in Figs.6.10 to 6.12. The initial-level set used for the segmentation

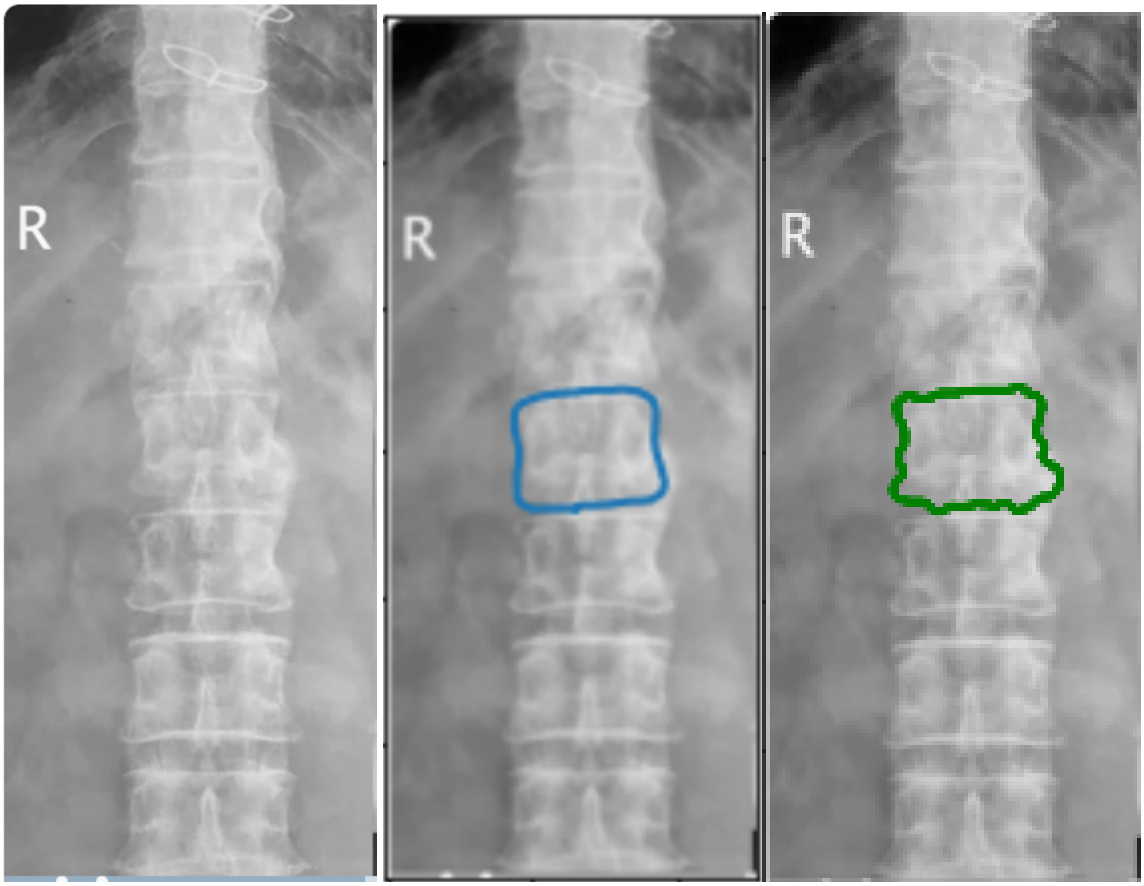

Figure 6.4: Initial level-set and segmentation result for L1 from Image 1. Image on the left: Original image; Image on the middle: Initial level-set (blue curve) used for segmentation of that vertebra; Image on the right: Segmentation result (green) for the correspondent vertebra.

of vertebra L4, from Image 1, and the concomitant segmentation are represented in Figure 6.10.

Figure 6.11 displays the corners of L4 and the correspondent histograms.

Figure 6.12 displays the four corners' histograms, for visual comparison.

6.1.1.5 Overview of the results for Image 1

Table 6.1 shows the average intensity values for each corner of each vertebra as well as the correspondent ratios values. In this table and in all tables in this chapter, DISH(+) vertebrae correspond to vertebrae with the disease and DISH(-) without. In this table, in DISH(+) vertebrae, the left intensity Average values (LS and LI) are pretty close to one another and quite different from the right intensity average values (RS and RI), which refers to the location in the vertebrae where the diseases manifests.

Figure 6.13 shows the ratio values (LS/RS and LI/RI) for each vertebra from Image 1. For ratio LS/RS, there is not difference between DISH(+) and DISH(-), however, the difference for ratio LI/RI between both DISH(+) and DISH(-) is quite clear.

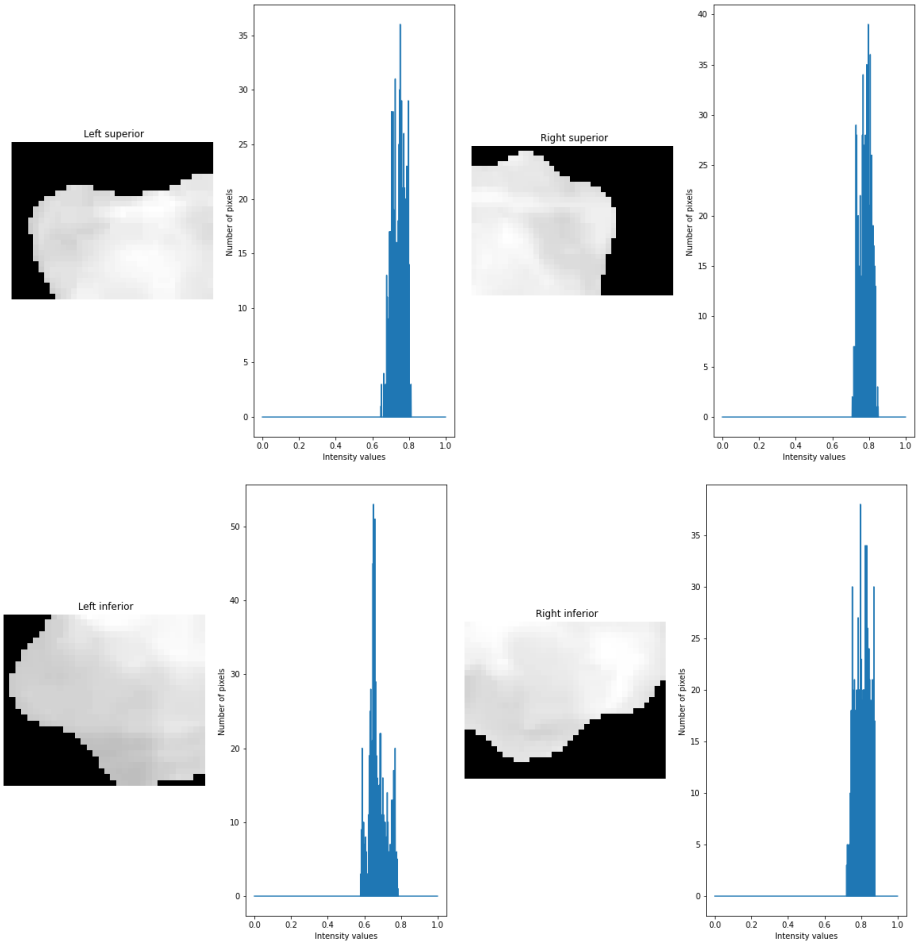

Figure 6.5: Comparison of each corner and its histograms for L1 vertebra from Image 1.

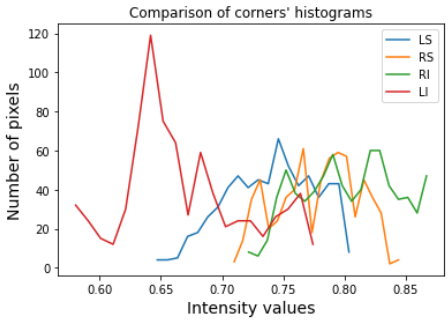

Figure 6.6: Comparison of all corners' histograms for L1 from Image 1, showing the difference between right side (green and orange curves) and left side of vertebra(red and blue curves).

6.1.2 Image 2

Similar to the previous section, all results showed herein are referent to Image 2. The remainder of the segmentations is found in III in section III.2.

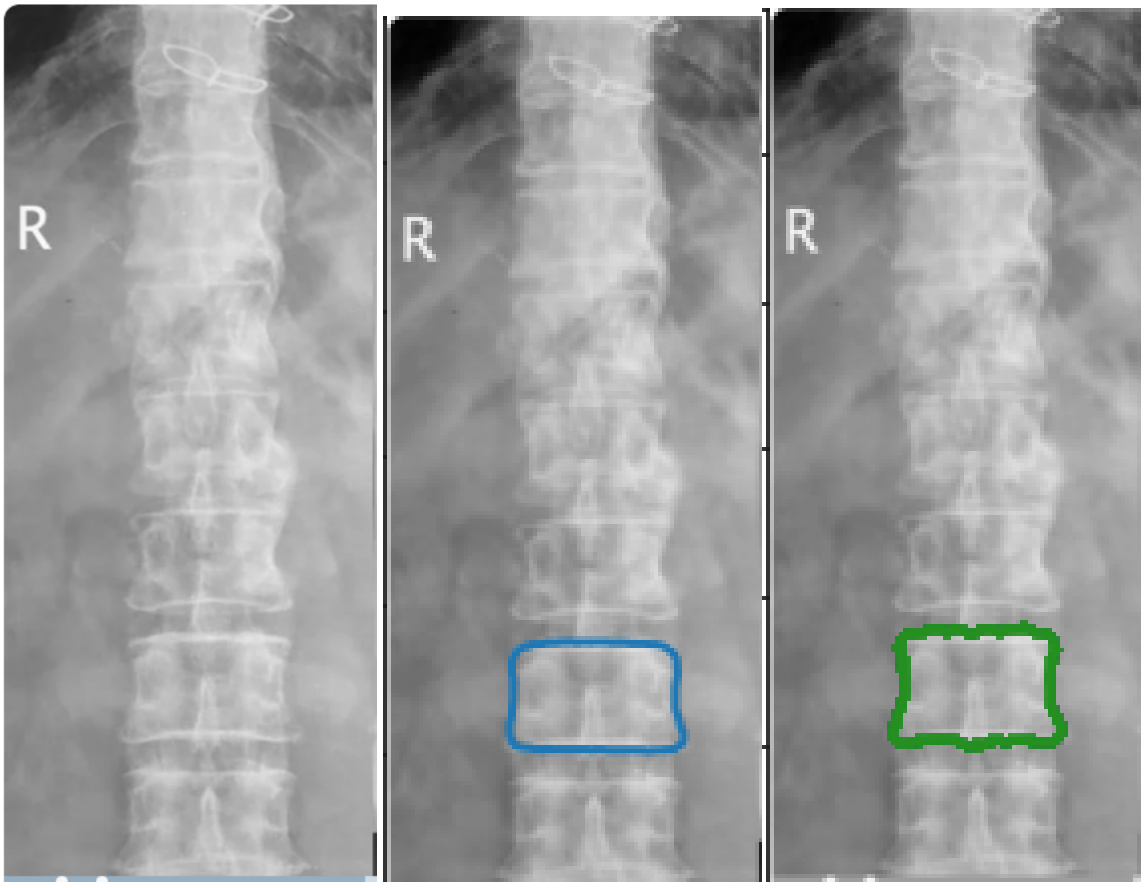

Figure 6.7: Initial level-set and segmentation result for L3 from Image 1. Image on the left: Original image; Image on the middle:Initial level-set (blue curve) used for segmentation of that vertebra; Image on the right: Segmentation result (green) for the correspondent vertebra.

Vertebra	DISH(+/-)	LS ± σ(LS)	RS ± σ(RS)	RI ± σ(RI)	LI ± σ(LI)	ratio(LS/RS)± δ(ratio(LS/RS))	ratio(LI/RI)± δ(ratio(LI/RI))
T10	DISH(+)	0.66±0.05	0.81±0.03	0.82±0.02	0.69±0.05	0.82±0.07	0.84±0.06
T11	DISH(+)	0.71±0.05	0.80±0.02	0.84±0.03	0.74±0.03	0.88±0.07	0.89±0.05
T12	DISH(+)	0.78±0.03	0.75±0.04	0.83±0.04	0.72±0.03	0.96±0.07	0.86±0.05
L1	DISH(+)	0.74±0.03	0.78±0.03	0.81±0.04	0.67±0.05	0.95±0.06	0.84±0.07
L2	DISH(+)	0.65±0.05	0.82±0.03	0.78±0.04	0.67±0.04	0.80±0.06	0.86±0.07
L3	DISH(-)	0.72±0.06	0.81±0.05	0.75±0.04	0.70±0.04	0.89±0.09	0.94±0.08
L4	DISH(-)	0.72±0.05	0.78±0.05	0.73±0.05	0.70±0.05	0.93±0.09	0.95± 0.10

Table 6.1: Intensity results for Image 1. In this table, it is possible to see the intensity values for each corner (LS-Left superior, RS-Right superior, RI-Right Inferior, LI-Left Inferior) and also the values of the ratios LI/RI and LR/RS.

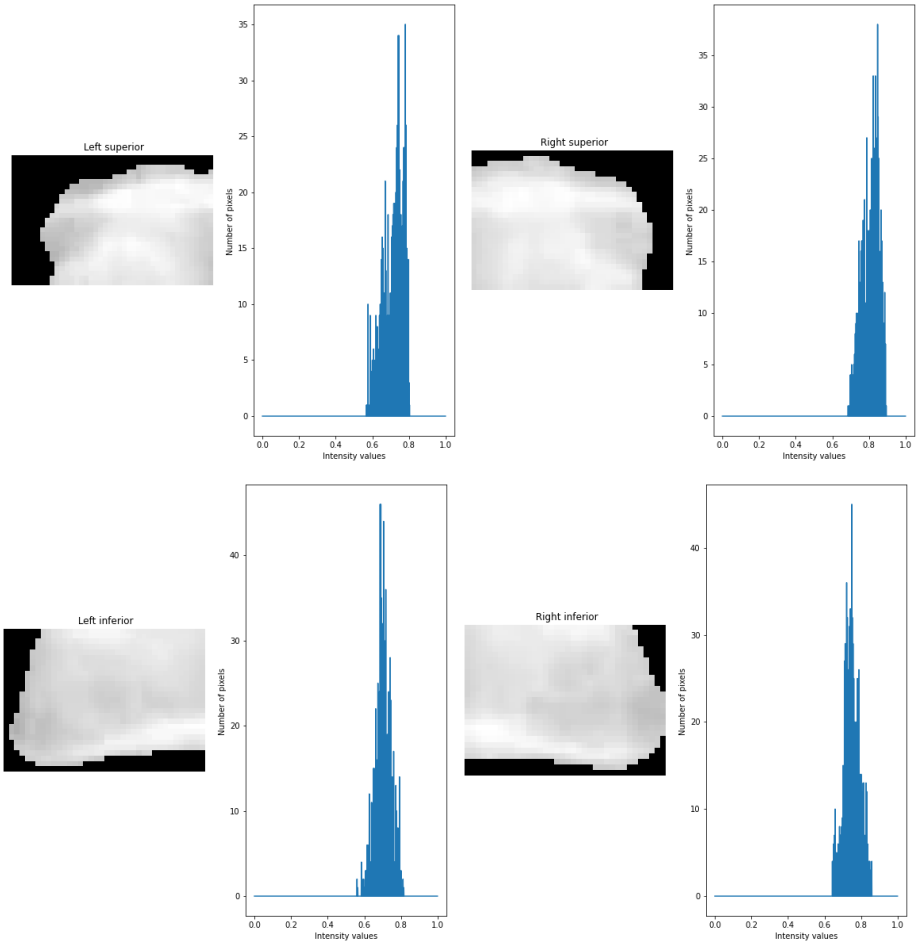

Figure 6.8: Comparison of each corner and its histograms for L3 vertebra from Image 1.

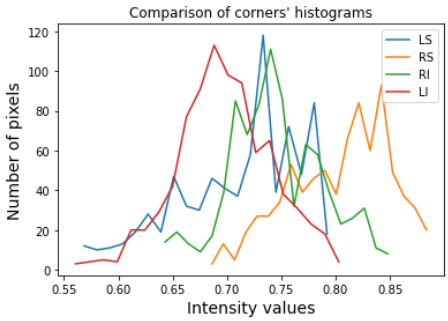

Figure 6.9: Comparison of all corners' histograms for L3 from Image 1, showing the difference between right side (green and orange curves) and left side of vertebra(red and blue curves).

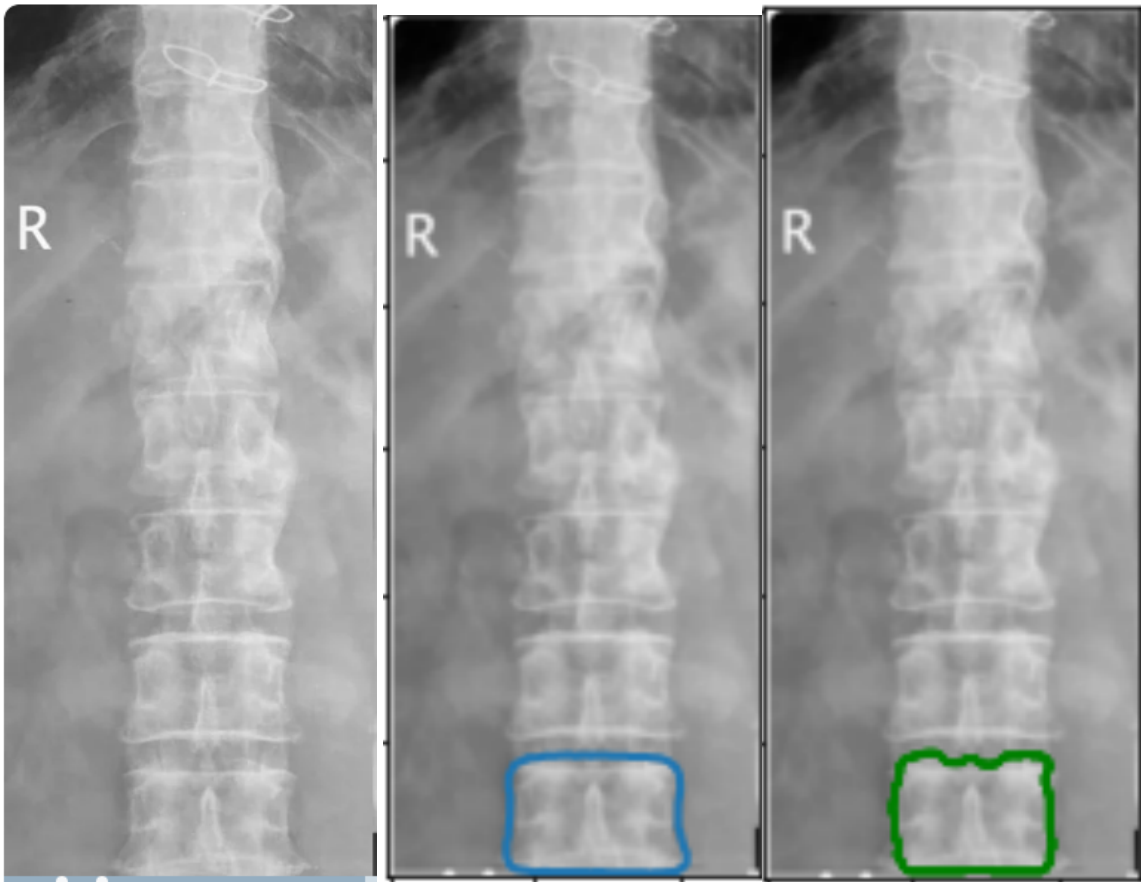

Figure 6.10: Initial level-set and segmentation result for L4 from Image 1.Image on the left: Original image; Image on the middle: Initial level-set (blue curve) used for segmentation of that vertebra; Image on the right: Segmentation result (green) for the correspondent vertebra.

6.1.2.1 T8 vertebra

The initial-level set used for the segmentation of vertebra T8, from Image 2, and the concomitant segmentation are shown in Figure 6.14.

Figure 6.15 displays the corners of L3 and the correspondent histograms.

Figure 6.16 displays the four corners' histograms, for visual comparison.

6.1.2.2 T9 vertebra

As the previous section, all results, presented in Figures 6.17 to 6.19, are referent to vertebra T9, from Image 2.

The initial-level set used for the segmentation of vertebra T9, from Image 2, and the concomitant segmentation are shown in Figure 6.17.

Figure 6.18 displays the corners for vertebra T9 and the correspondent histograms.

Figure 6.19 displays all four corners' histograms, for visual comparison.

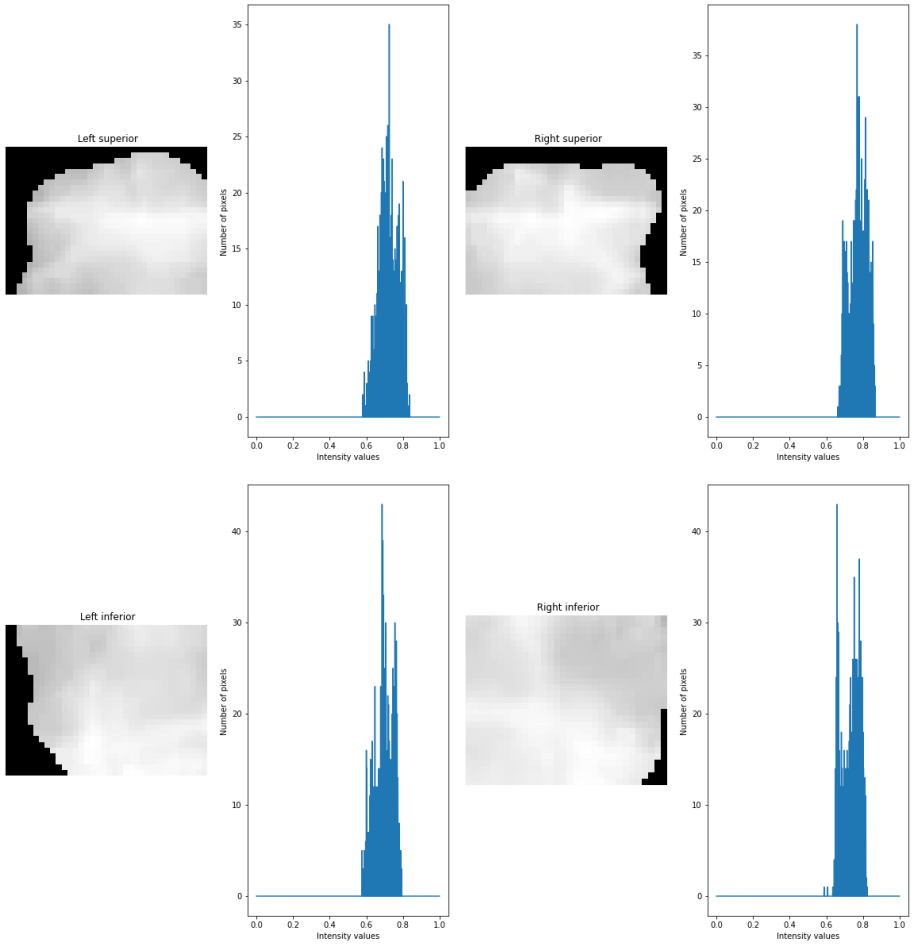

Figure 6.11: Comparison of each corner and its histograms for the L4 vertebra from Image 1.

Vertebra	DISH(+/-)	LS ± σ(LS)	RS ± σ(RS)	RI ± σ(RI)	LI ± σ(LI)	ratio(LS/RS)± δ(ratio(LS/RS))	ratio(LI/RI)± δ(ratio(LI/RI))
T7	DISH(+)	0.64±0.01	0.71±0.01	0.74±0.01	0.65±0.02	0.89±0.02	0.88±0.03
T8	DISH(+)	0.69±0.015	0.760±0.01	0.77±0.012	0.70±0.03	0.90±0.02	0.90±0.04
T9	DISH(+)	0.74±0.01	0.79±0.01	0.79±0.02	0.74±0.01	0.93±0.02	0.94±0.03
T10	DISH(+)	0.71±0.03	0.80±0.02	0.82±0.01	0.72±0.02	0.88±0.03	0.88±0.03

Table 6.2: Intensity results for Image 2. In this table, it is possible to see the intensity values for each corner(LS-Left superior,RS-Right superior, RI-Right Inferior,LI-Left Inferior) and also the values of the ratios LI/RI and LR/RS.

6.1.2.3 Overview of the results for Image 2

Table 6.2 shows the intensity values for each corner as well the correspondent ratios values. Similarly to the results obtained for Image 1, the average intensity values for left corners (LS and LI) are very similar between each other and quite different from the results for the right corners (RS and RI), where the disease manifests.

Figure 6.20 shows the ratio values(LS/RS and LI/RI) for each vertebra from Image 2.

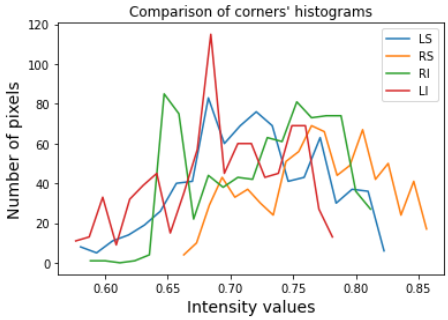

Figure 6.12: Comparison of all corners' histograms for L4 from Image 1, showing the difference between right side (green and orange curves) and left side of vertebra (red and blue curves).

6.1.3 Image 3

As done for the two previous sections, the results presented here refer to the analysis of some vertebrae from Image 3. The remainder of the segmentations is found in III in section III.3.

6.1.3.1 T12 vertebra

The initial-level set used for the segmentation of vertebra T12, from Image 3, and the concomitant segmentation are shown in Figure 6.21.

Figure 6.22 displays the four corners of vertebra T12 and the correspondent histograms.

Figure 6.23 displays all four corners' histograms of T12 vertebra.

6.1.3.2 L2 vertebra

As done for the previous vertebra, in this section, the results, presented in Figures 6.24 to 6.26, refer to the vertebra L2.

The initial level-set used for the segmentation of the vertebra L2, from Image 3, and the concomitant segmentation are shown in Figure 6.24.

Figure 6.25 displays the four corners of vertebra L2 and the correspondent histograms are shown.

Figure 6.26 displays all four corners' histograms, for visual comparison.

6.1.3.3 L3 vertebra

As done for the previous vertebra, the results presented in the section, shown in Figures 6.27 to 6.29.

The initial-level set used for the segmentation of the L3 vertebra from Image 3 and the concomitant segmentation are shown in Figure 6.27.

Figure 6.28 displays the four corners the corners of L3 vertebra and the correspondent histograms.

Figure 6.29 displays all four corners' histograms, for visual comparison.

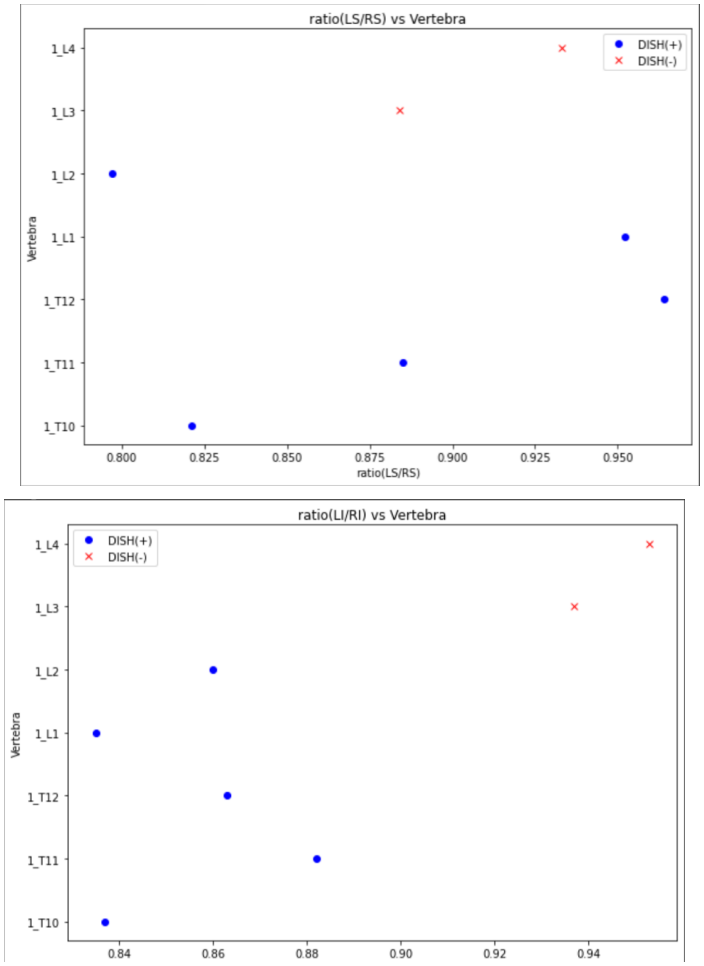

Figure 6.13: Comparison of the ratio LS/RS (figure at the top) and ratio LI/RI (figure at the bottom) for each vertebra from Image 1. The blue points refer to the pathological vertebra and the red points to the non-pathological.

Vertebra	DISH(+/-)	LS ± σ(LS)	RS ± σ(RS)	RI ± σ(RI)	LI ± σ(LI)	ratio(LS/RS)± δ(ratio(LS/RS))	ratio(LI/RI)± δ(ratio(LI/RI))
T11	DISH(-)	0.47±0.03	0.45±0.03	0.42±0.03	0.40±0.03	0.96±0.09	0.97±0.09
T12	DISH(-)	0.36±0.02	0.39±0.03	0.37±0.03	0.35±0.03	0.94±0.09	0.94±0.10
L1	DISH(-)	0.33±0.03	0.35±0.03	0.32±0.04	0.31±0.03	0.95±0.10	0.97±0.16
L2	DISH(-)	0.34±0.03	0.30±0.04	0.30±0.03	0.30±0.03	0.89±0.17	0.99±0.14
L3	DISH(-)	0.36±0.03	0.35±0.03	0.34±0.05	0.33±0.04	0.99±0.12	0.99±0.18

Table 6.3: Intensity results for Image 3. In this table, it is possible to see the intensity values for each corner (LS-Left superior, RS-Right superior, RI-Right Inferior,LI-Left Inferior) of each vertebra as well as the values of the ratios LI/RI and LR/RS.

6.1.3.4 Results for Image 3

Table 6.3 shows the average intensity values for each corner as well as the correspondent ratio values for each vertebra from Image 3. As it possible to see, the difference between the average intensity values for all four corners is not significant for all DISH(-) vertebrae.

Figure 6.30 shows the ratio values (LS/RS and LI/RI) for each vertebra from Image 3. It is possible to see that the values for LI/RI are bigger than LR/RS, highlighting the lack of difference between both side of DISH(-) vertebrae.

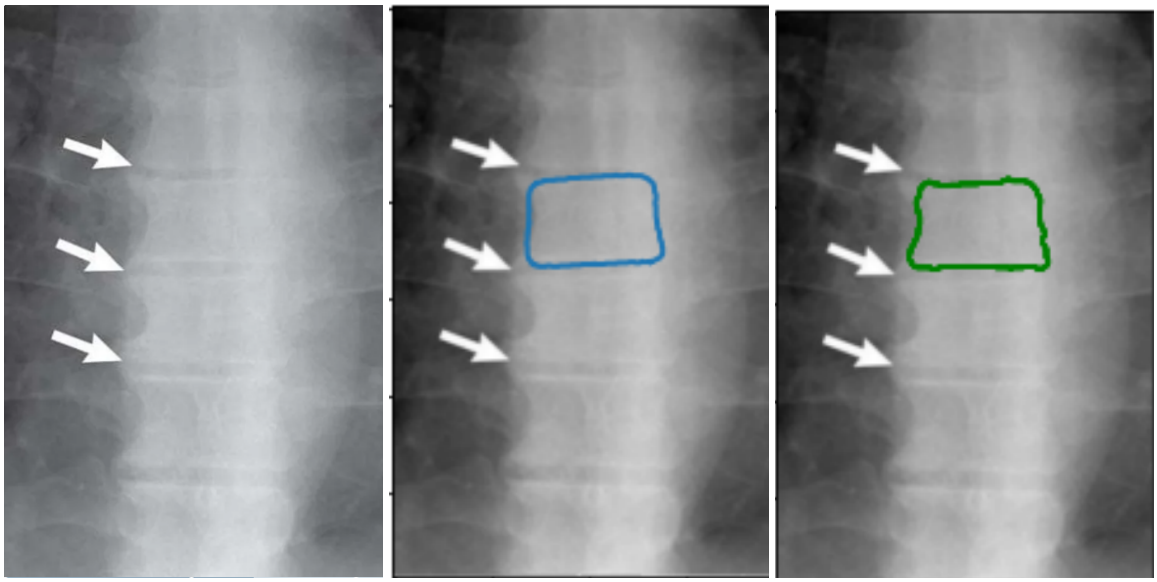

Figure 6.14: Initial level-set and segmentation result for T8 from Image 2.Image on the left: Original image;Image on the middle: Initial level-set(blue curve) used for segmentation of that vertebra; Image on the right: Segmentation result(green) for the correspondent vertebra.

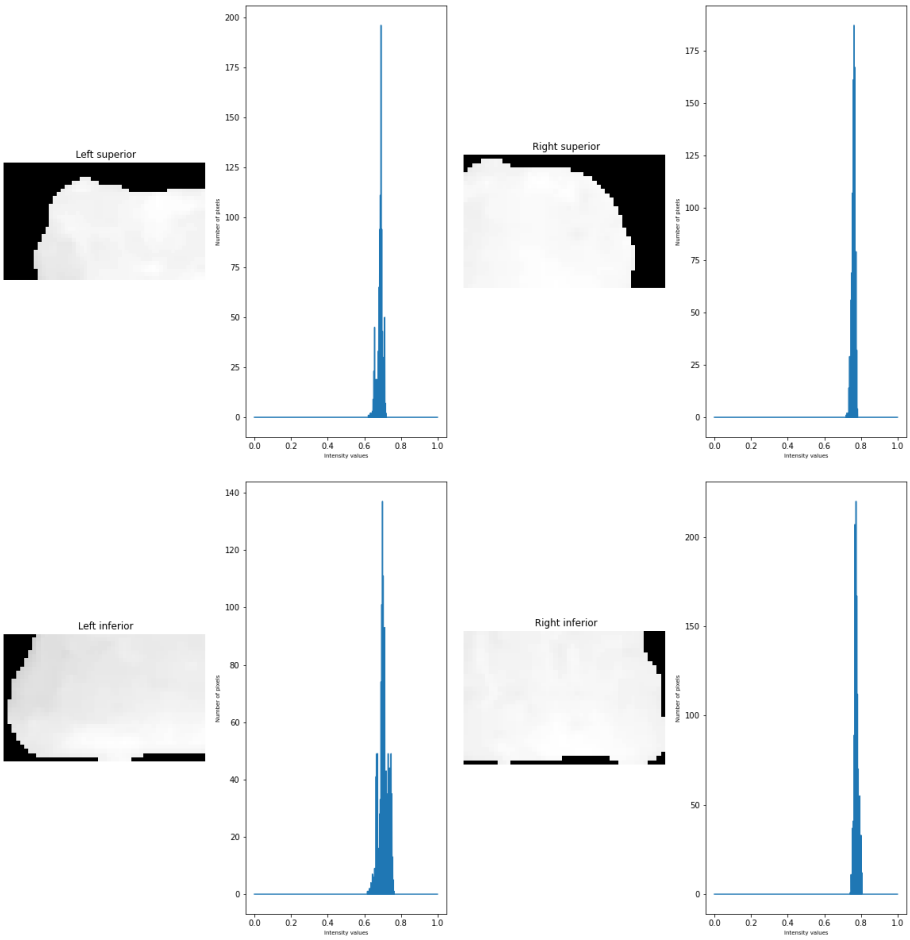

Figure 6.15: Comparison of each corner and its histograms for the T8 vertebra from Image 2.

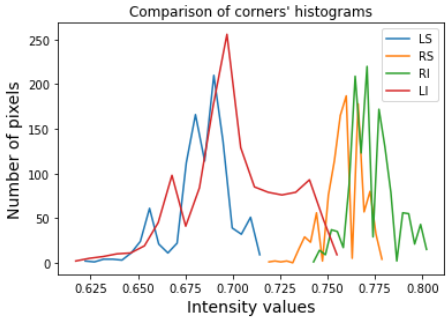

Figure 6.16: Comparison of all corners' histograms for T8 from Image 2, showing the difference between right side (green and orange curves) and left side of vertebra(red and blue curves)..

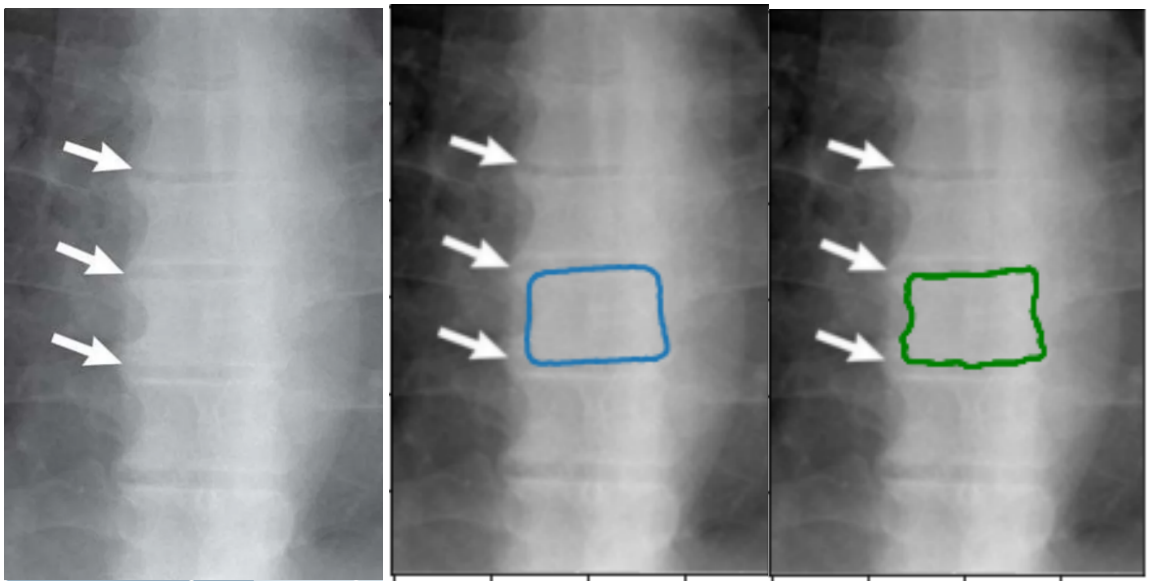

Figure 6.17: Initial level-set and segmentation result for T9 from Image 2.Image on the left: Original image; Image on the middle: Initial level-set (blue curve) used for segmentation of that vertebra; Image on the right: Segmentation result (green) for the correspondent vertebra.

6.1.4 Image 4

As done for the other Images, this section refers the results obtained for some vertebrae of Image 4. The remainder of the results is found in III in section III.4.

6.1.4.1 T12 vertebra

The initial-level set used for the segmentation of vertebra T12, from Image 4, and the concomitant segmentation are represented in Figure 6.31.

Figure 6.32 displays the corners of vertebra T12 and the correspondent histograms.

Figure 6.33 displays all four corners' histograms, for visual comparison.

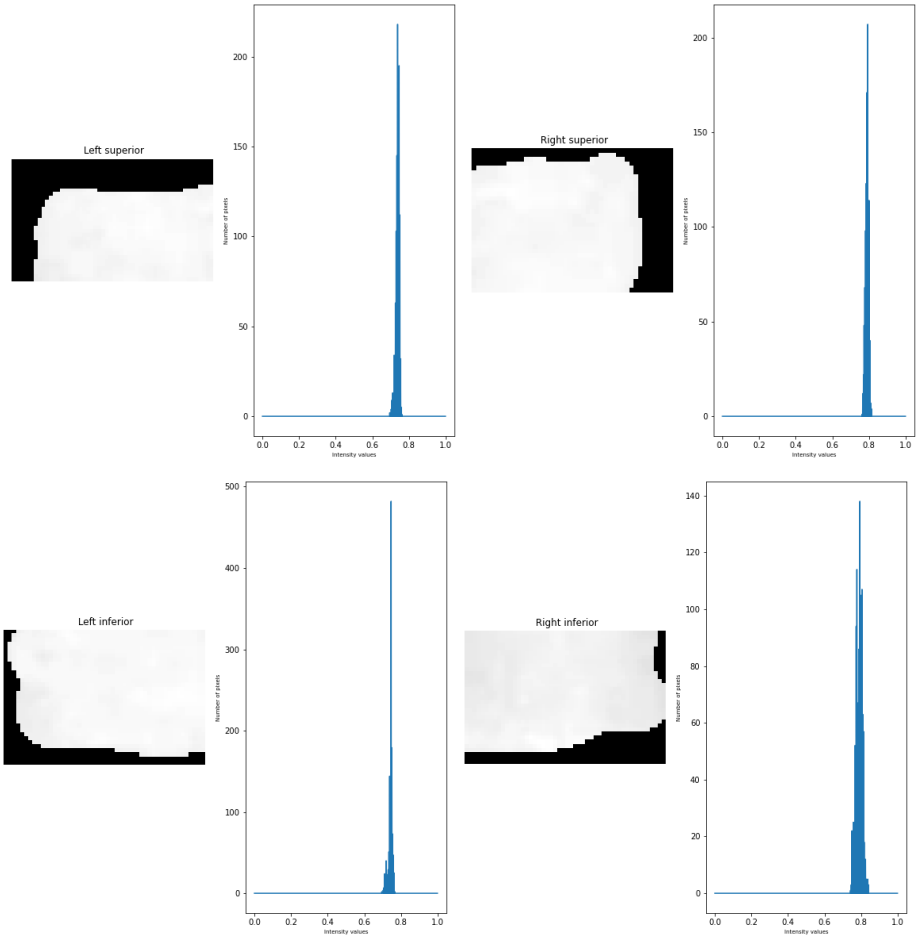

Figure 6.18: Comparison of each corner and its histograms for T9 vertebra from Image 2.

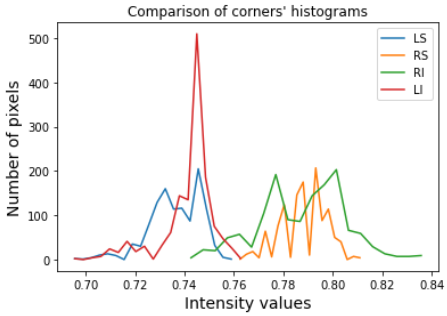

Figure 6.19: Comparison of all corners' histograms for T9 from Image 2, showing the difference between right side (green and orange curves) and left side of vertebra(red and blue curves) for T9 vertebra from Image 2.

6.1.4.2 L1 vertebra

As done for the previous section, herein the results, presented in Figures 6.34 to 6.36, refer to the vertebra L1.

The initial-level set used for the segmentation of vertebra L1, from Image 4, and the concomitant segmentation are shown in Figure 6.34.

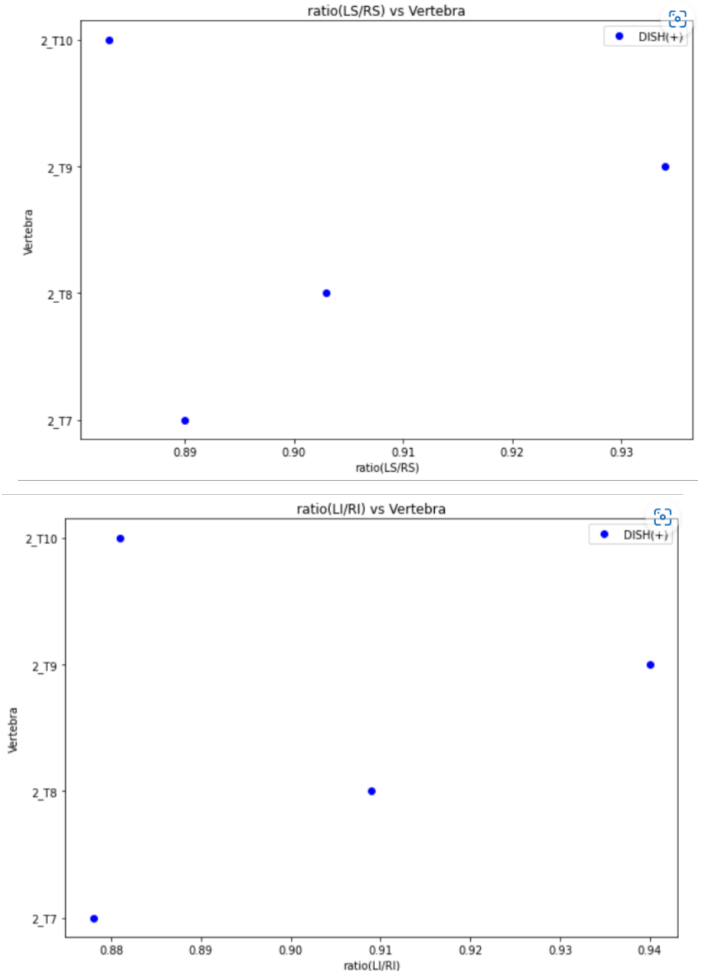

Figure 6.20: Comparison of the ratio LS/RS(figure at the top) and ratio LI/RI (figure at the bottom) for each vertebra from Image 2. The blue points refer to the pathological(DISH(+)) vertebrae.

Vertebra	Type of vertebra	LS ± σ(LS)	RS ± σ(RS)	RI ± σ(RI)	LI ± σ(LI)	ratio(LS/RS)± δ(ratio(LS/RS))	ratio(LI/RI)± δ(ratio(LI/RI))
T10	DISH(+)	0.57±0.03	0.59±0.04	0.62±0.03	0.56±0.05	0.96±0.09	0.91±0.09
T11	DISH(+)	0.60±0.03	0.68±0.03	0.63±0.02	0.54±0.03	0.88±0.06	0.85±0.05
T12	DISH(+)	0.61±0.03	0.69±0.02	0.67±0.02	0.56±0.04	0.89±0.06	0.84±0.07
L1	DISH(+)	0.69±0.024	0.74±0.02	0.70±0.02	0.63±0.02	0.93±0.04	0.90±0.04

Table 6.4: Intensity results for Image 4. In this table, it is possible to see the intensity values for each corner (LS-Left superior, RS-Right superior, RI-Right Inferior, LI-Left Inferior) and also the values of the ratios LI/RI and LR/RS.

Figure 6.35 displays all four corners of L1 vertebra and the correspondent histograms. Figure 6.36 displays the four corners' histograms, for visual comparison.

6.1.4.3 Results for Image 4

Table 6.4 shows the intensity values for each corner for vertebra L1 as well as the correspondent ratios. It is noteworthy that the average intensity values for the right corners, where the disease manifests, are bigger than the correspondent left ones.

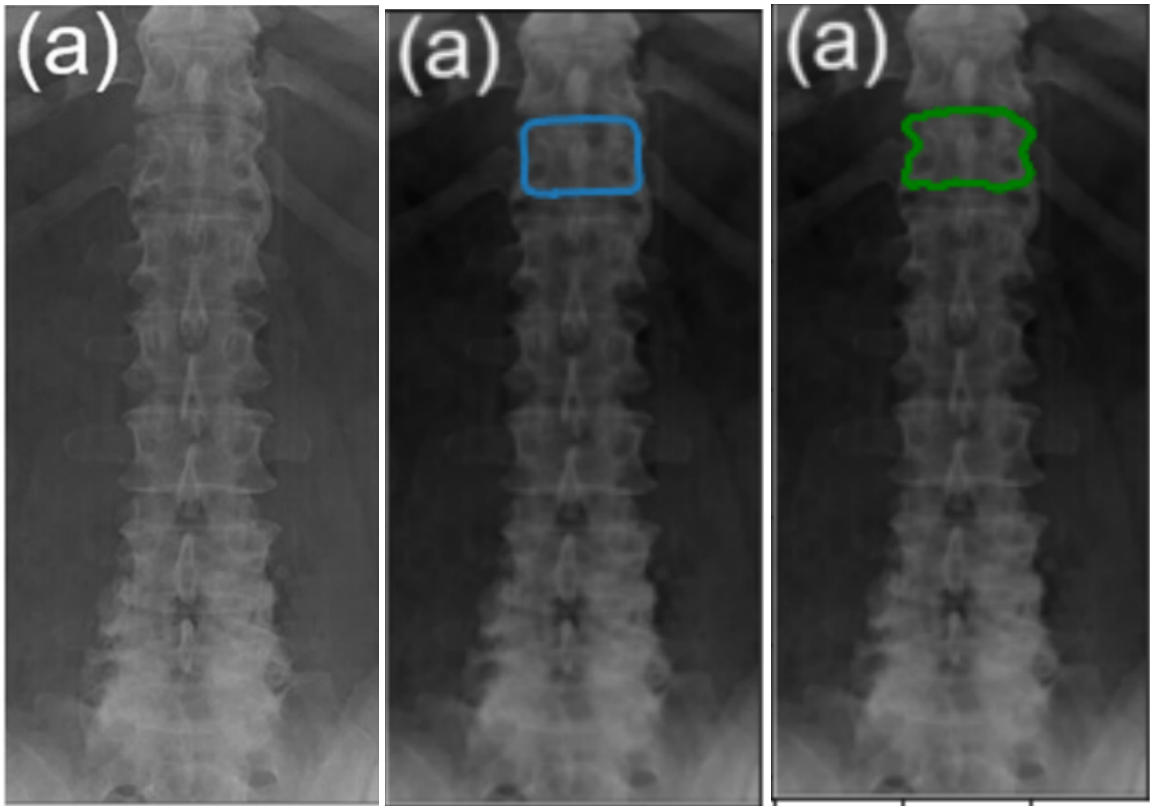

Figure 6.21: Initial level-set and segmentation result for T12 from Image 3. Image on the left: Initial level-set (blue curve) used for segmentation of that vertebra; Image on the right: Segmentation result (green) for the correspondent vertebra.

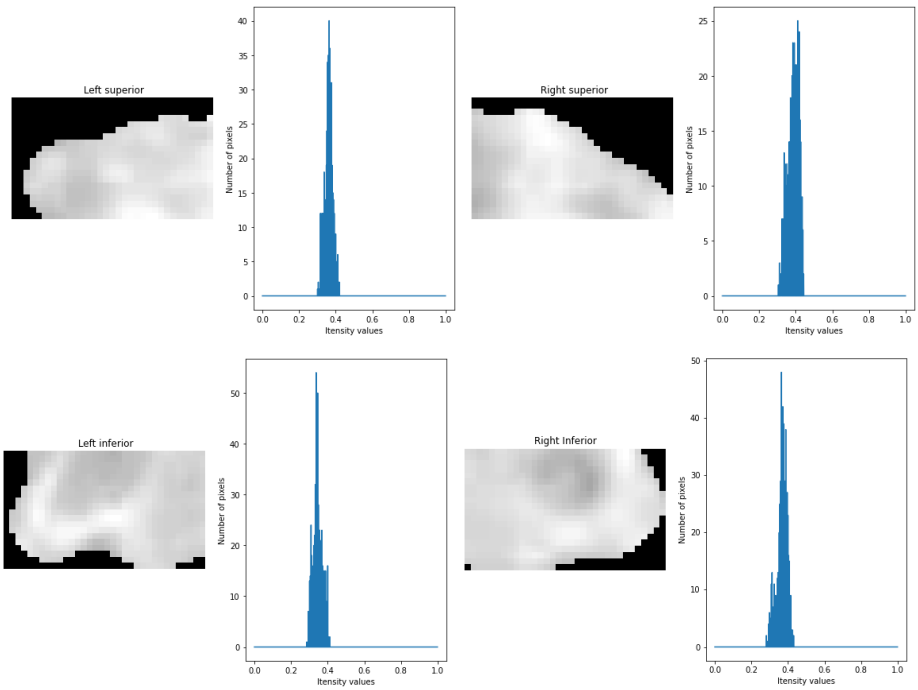

Figure 6.22: Comparison of each corner and its histograms for the T12 vertebra from Image 3.

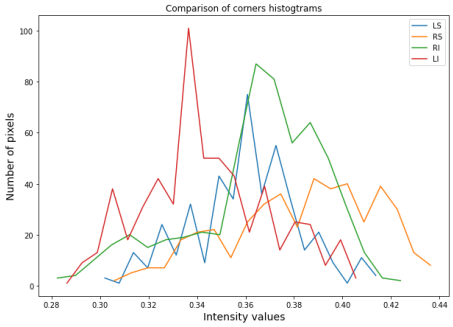

Figure 6.23: Comparison of all corners' histograms for T12 from Image 3, showing the difference between right side (green and orange curves) and left side of vertebra (red and blue curves).

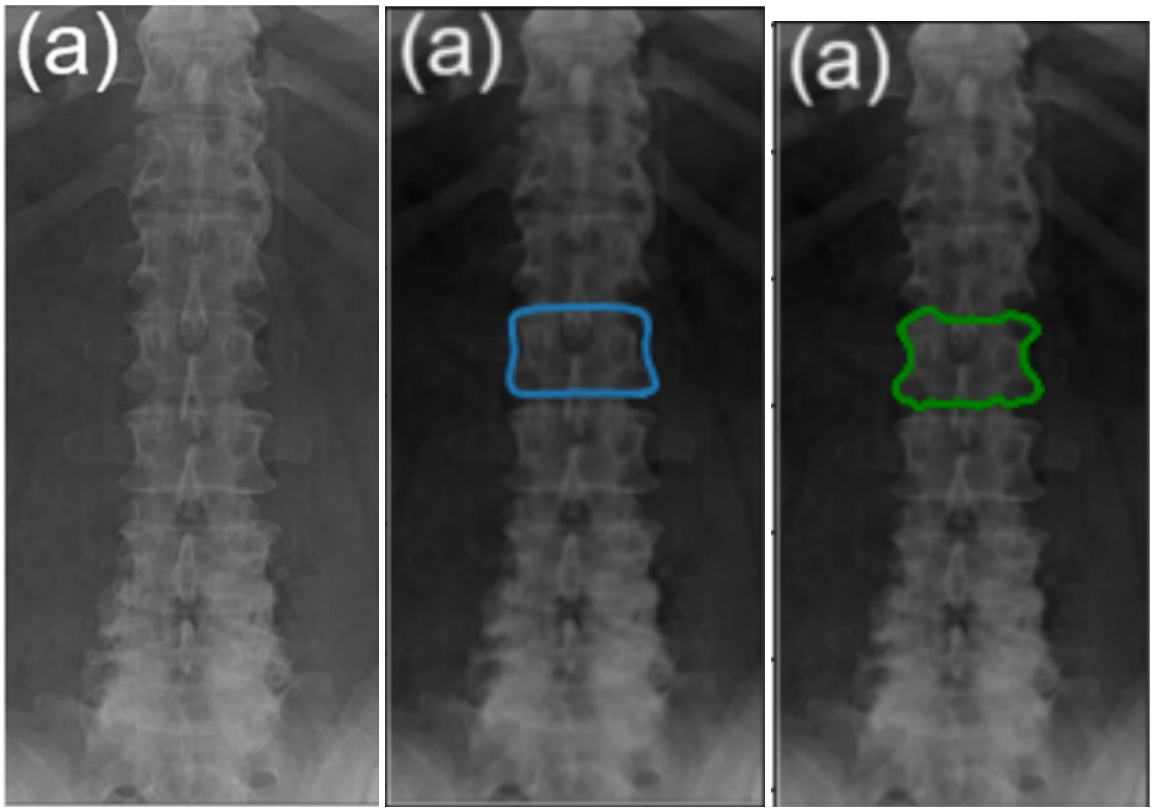

Figure 6.24: Initial level-set and segmentation result for L2 from Image 3. Image on the left: Initial level-set (blue curve) used for segmentation of that vertebra; Image on the right: Segmentation result (green) for the correspondent vertebra.

Figure 6.37 shows the ratio values (LS/RS and LI/RI) for each vertebra from Image 4. In this figure, it is possible to see that the ratio LI/RI values, shown in the Right image, has lower values than LR/RS, highlighting the difference between both sides of DISH(+) vertebrae.

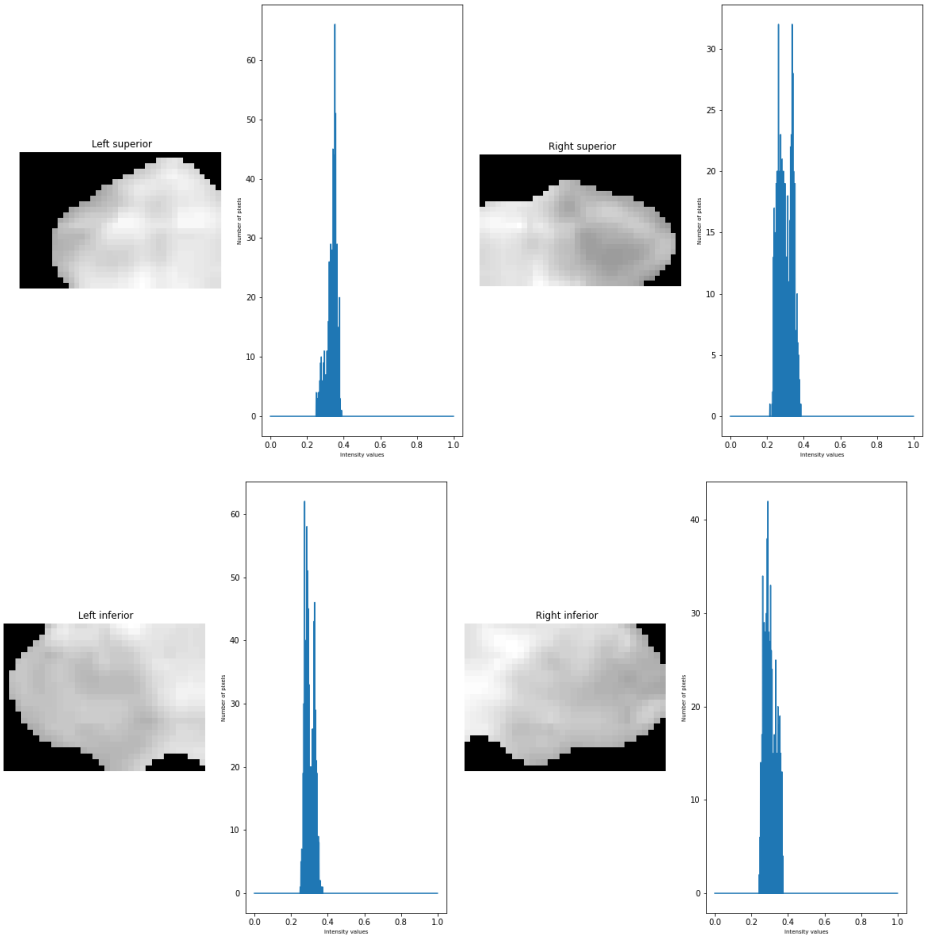

Figure 6.25: Comparison of each corner and its histograms for the L2 vertebra from Image 3.

6.1.5 Image 5

Finally, the results obtained for some vertebrae from Image 5 are presented in this section. The remainder of the segmentations is found in III in section III.5.

6.1.5.1 T7 vertebra

The initial-level set used for the segmentation of the vertebra T7, from Image 5, and the concomitant segmentation are shown in Figure 6.38.

Figure 6.39 displays the corners of vertebra T7 and the correspondent histograms.

Figure 6.40 displays the four corners' histograms, for visual comparison.

6.1.5.2 T10 vertebra

Herein, the results for vertebra T10 are represented in Figures 6.41 to 6.43.

The initial-level set used for the segmentation of the T10 vertebra, from Image 5, and the concomitant segmentation are shown in Figure 6.41.

Figure 6.42 displays the corners of vertebra T10 and the correspondent histograms.

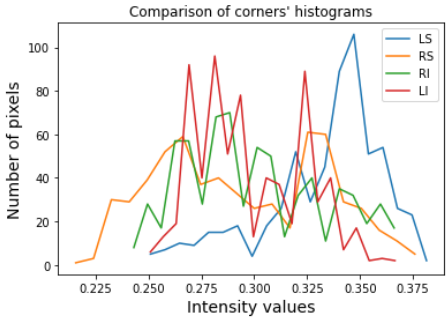

Figure 6.26: Comparison of all corners' histograms for L2 from Image 3, showing the difference between right side (green and orange curves) and left side of vertebra (red and blue curves).

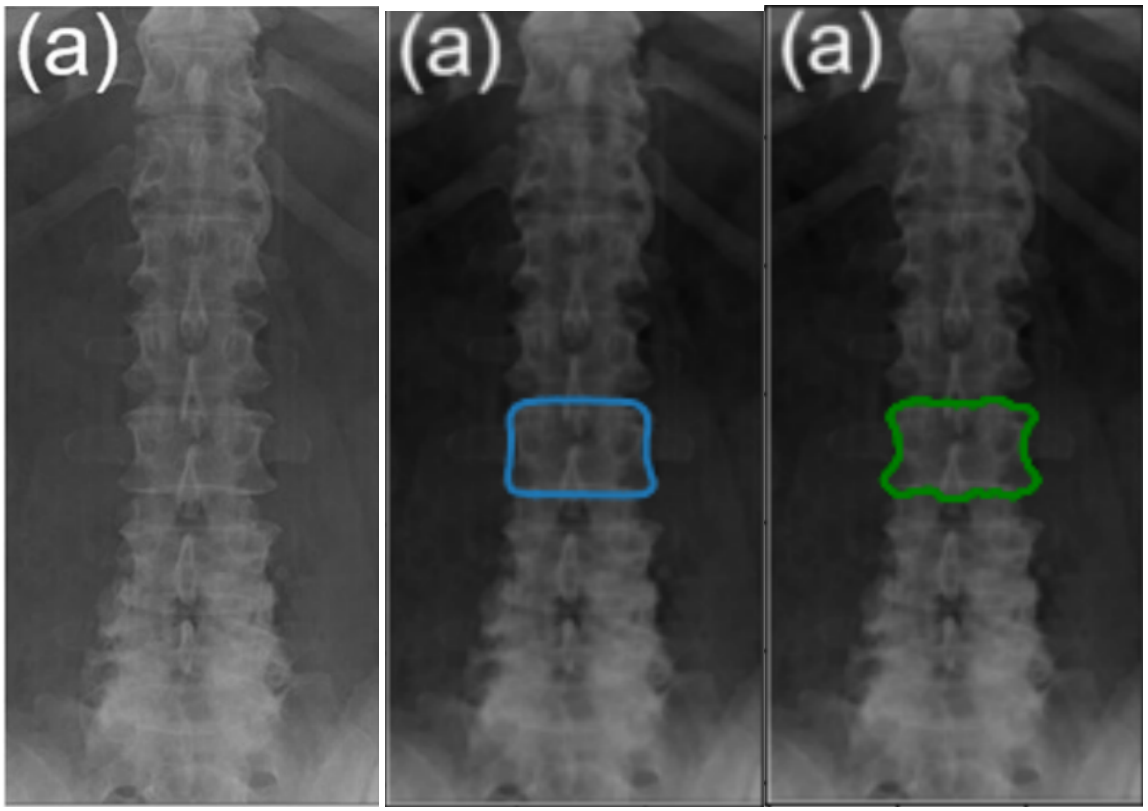

Figure 6.27: Initial level-set and segmentation result for L3 from Image 3. Image on the left: Initial level-set (blue curve) used for segmentation of that vertebra; Image on the right: Segmentation result (green) for the correspondent vertebra.

Figure 6.43 displays the corners' histograms a comparison between each corner histogram of this vertebra is shown.

6.1.5.3 T11 vertebra

The initial-level set used for the segmentation of vertebra T11, from Image 5, and the concomitant segmentation are shown in Figure 6.44.

Figure 6.45 displays the corners of vertebra T11 and the correspondent histograms.

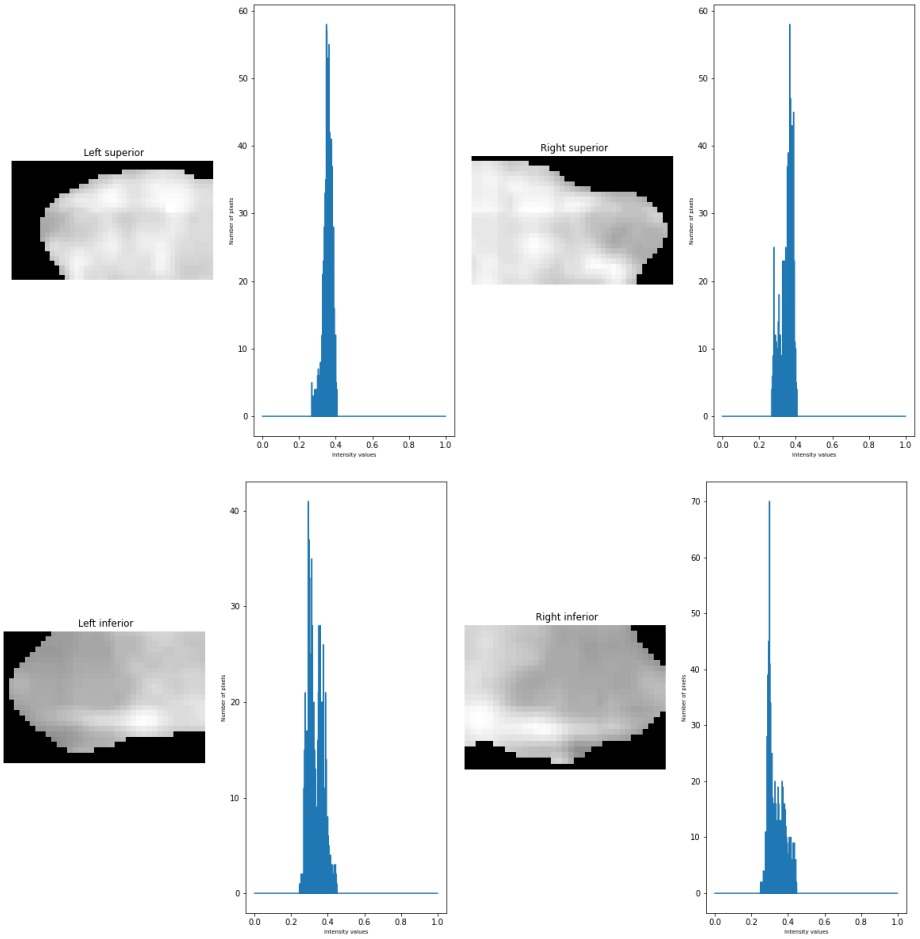

Figure 6.28: Comparison of each corner and its histograms for the L3 vertebra from Image 3.

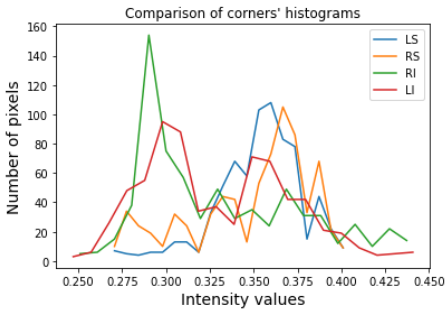

Figure 6.29: Comparison of all corners' histograms for L3 from Image 3, showing the difference between right side (green and orange curves) and left side of vertebra (red and blue curves).

Figure 6.46 displays the corners' histograms, for visual comparison.

6.1.5.4 Results for Image 5

Table 6.5 shows the intensity values for each corner as well as the correspondent ratios for this image. In this table, it is noticeable the difference between the average intensity

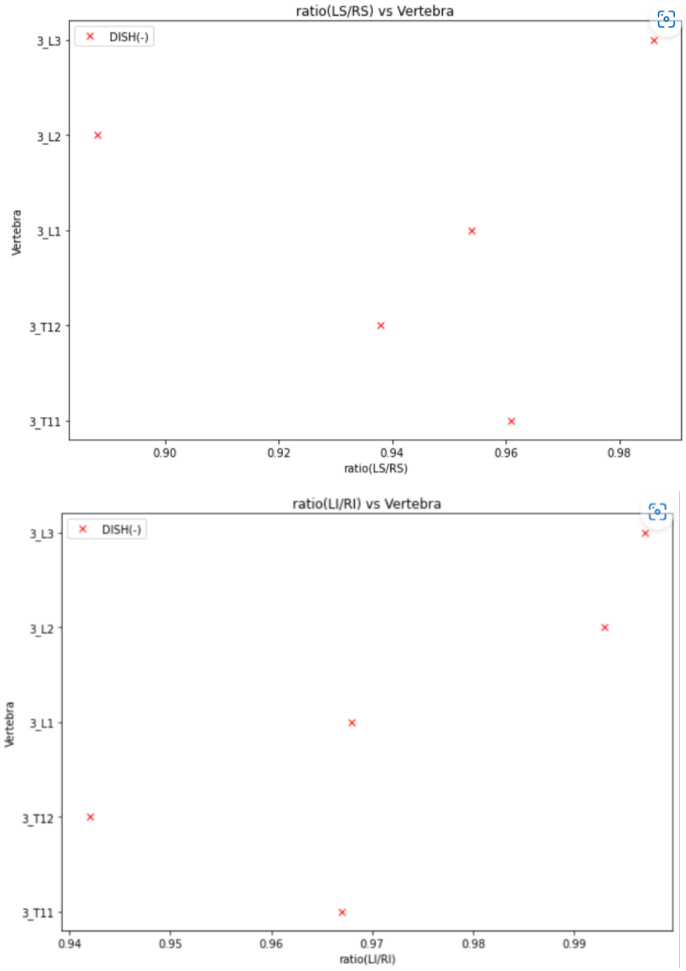

Figure 6.30: Comparison of the ratio LS/RS (figure at the left) and ratio LI/RI (figure at the right) for each vertebra from Image 3. The red points refer to the non-pathological (DISH(-)) vertebrae.

Vertebra	DISH(+/-)	LS ± σ(LS)	RS ± σ(RS)	RI ± σ(RI)	LI ± σ(LI)	ratio(LS/RS)± δ(ratio(LS/RS))	ratio(LI/RI)± δ(ratio(LI/RI))
T6	DISH(+)	0.59±0.02	0.62±0.01	0.67±0.01	0.61±0.01	0.93±0.03	0.91±0.02
T7	DISH(+)	0.64±0.01	0.69±0.01	0.71±0.02	0.66±0.02	0.92±0.02	0.93±0.04
T8	DISH(+)	0.69±0.01	0.74±0.01	0.78±0.01	0.71±0.02	0.92±0.02	0.91±0.03
T9	DISH(+)	0.74±0.02	0.80±0.01	0.83±0.01	0.78±0.02	0.93±0.02	0.94±0.03
T10	DISH(+)	0.80±0.02	0.85±0.01	0.87±0.01	0.82±0.02	0.94±0.02	0.95±0.02
T11	DISH(+)	0.85±0.01	0.88±0.01	0.91±0.01	0.90±0.02	0.96±0.02	0.98±0.02

Table 6.5: Intensity results for Image 5. In this table, it is possible to see the intensity values for each corner (LS-Left superior, RS-Right superior, RI-Right Inferior, LI-Left Inferior) and also the values of the ratios LI/RI and LR/RS.

values of left corners and correspondent right corners, where the disease manifests.

Figure 6.47 shows the ratio values (LS/RS and LI/RI) for each vertebra from Image 5 are plotted.

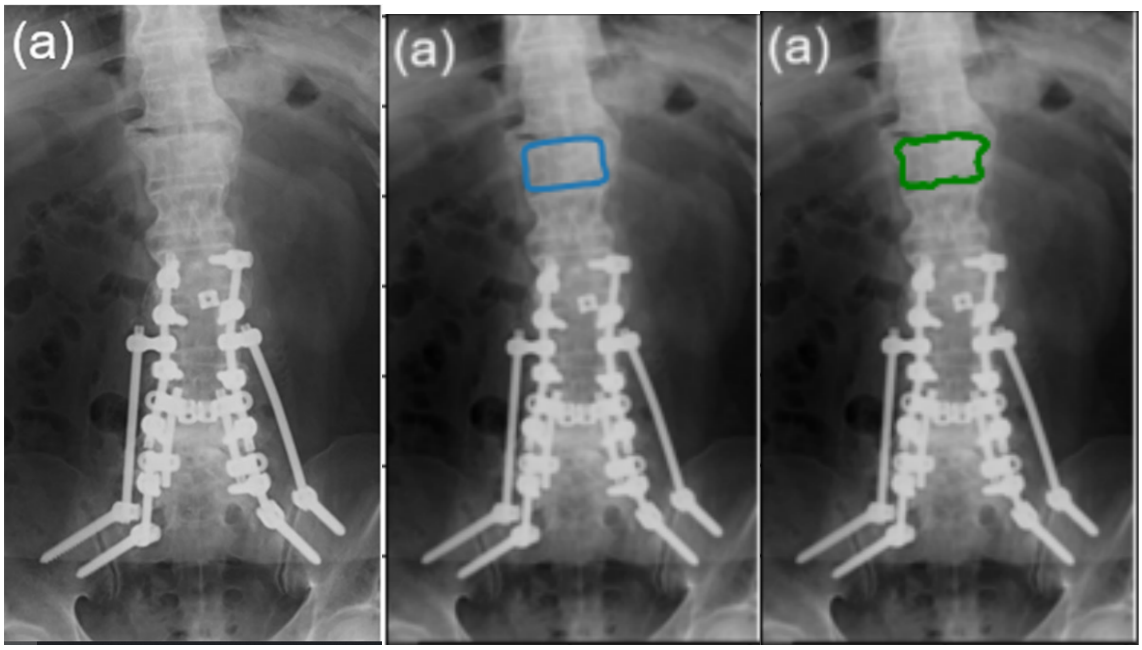

Figure 6.31: Initial level-set and segmentation result for T12 from Image 4. Image on the left: Original image; Image on the middle: Initial level-set (blue curve) used for segmentation of that vertebra; Image on the right: Segmentation result (green) for the correspondent vertebra.

6.1.6 Overview of all vertebrae

In this section, it will be provided the graphical representation of the ratios LR/RS, seen in Figure 6.48, and LI/RS, seen in Figure 6.49, denoting which vertebrae are DISH(+) and DISH(-). In the graph presenting the values for ratio LI/RI, it is noticeable a difference between DISH(+) (blue) and DISH(-) (red) ratio values.

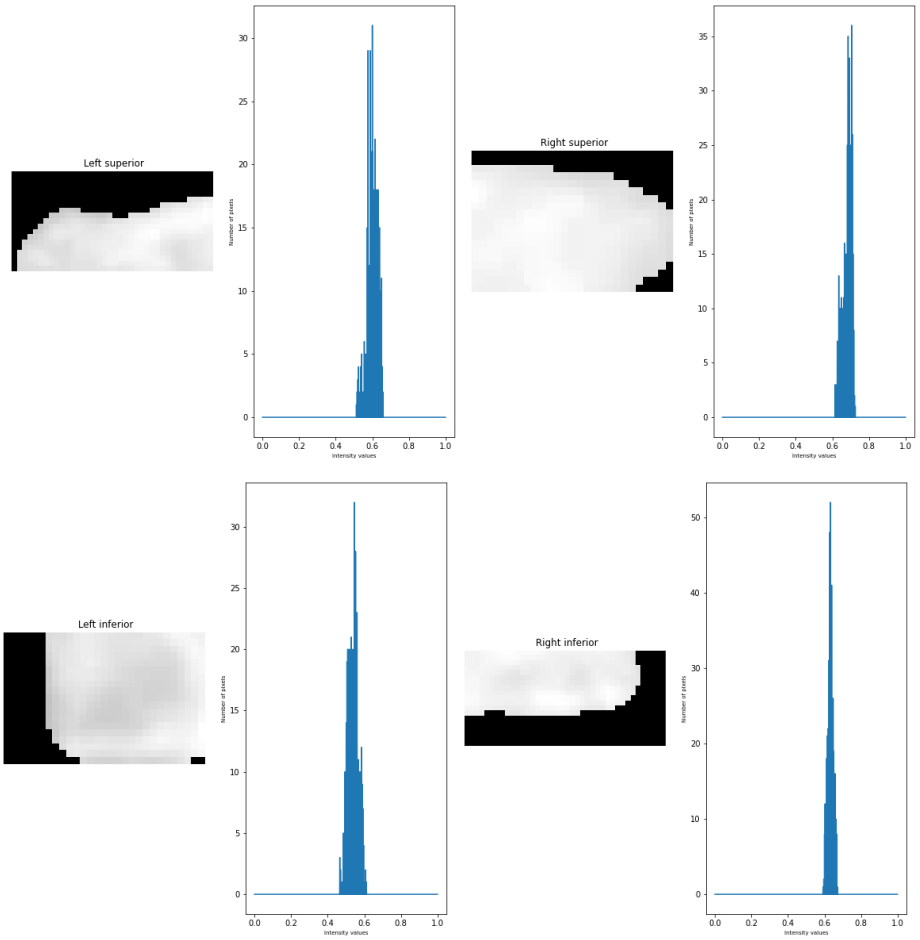

Figure 6.32: Comparison of each corner and its histograms for the T12 vertebra from Image 4.

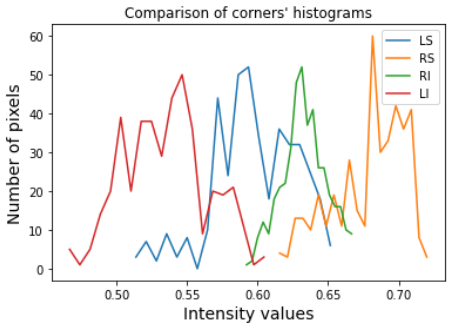

Figure 6.33: Comparison of all corners' histograms for T12 from Image 4, showing the difference between right side (green and orange curves) and left side of vertebra (red and blue curves).

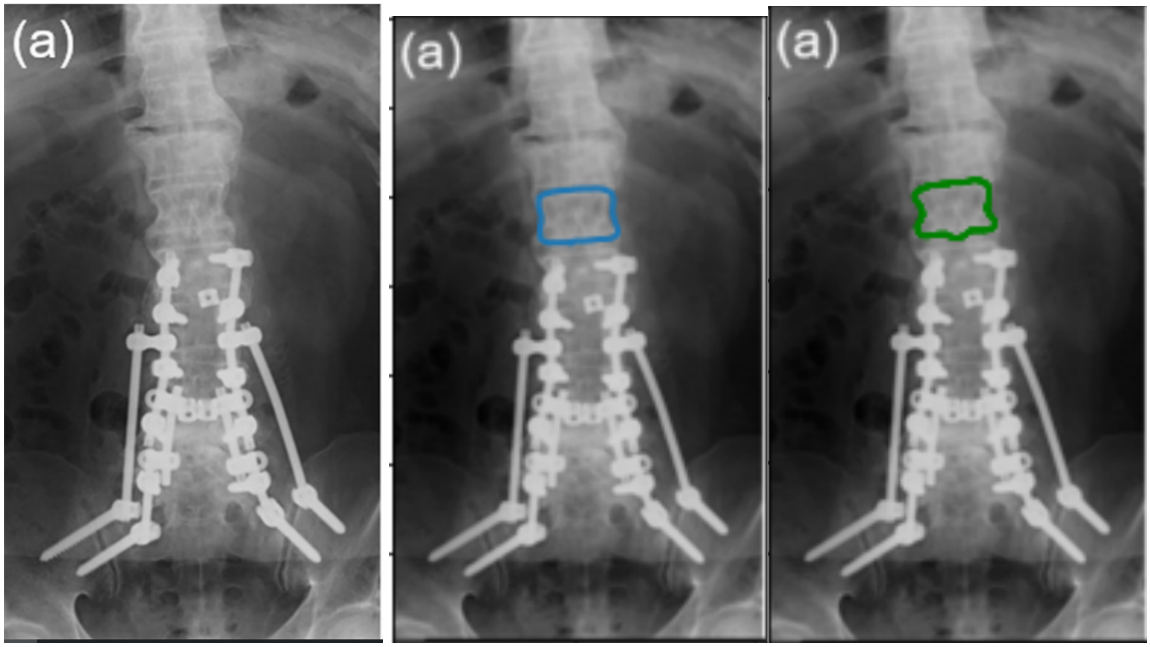

Figure 6.34: Initial level-set and segmentation result for L1 from Image 4. Image on the left: Original image; Image on the middle: Initial level-set (blue curve) used for segmentation of that vertebra;Image on the right: Segmentation result (green) for the correspondent vertebra.

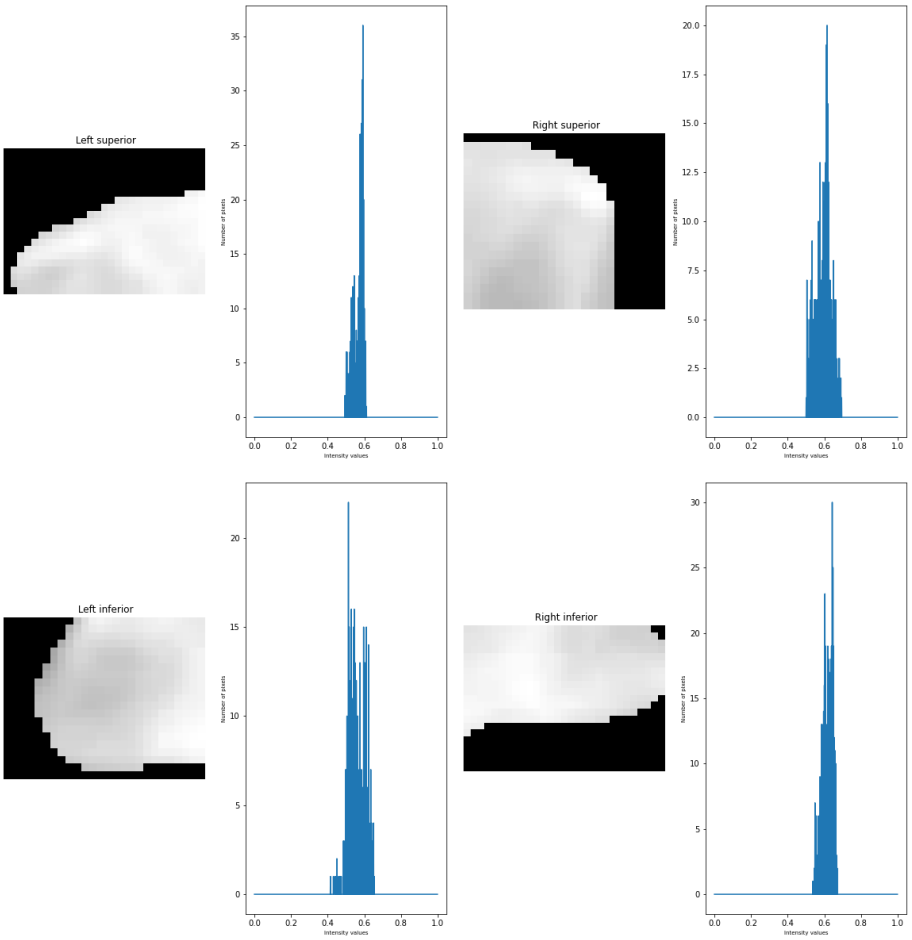

Figure 6.35: Comparison of each corner and its histograms for the L1 vertebra from Image 4.

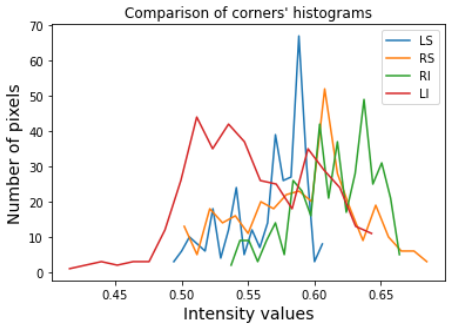

Figure 6.36: Comparison of all corners' histograms for L1 from Image 4, showing the difference between right side (green and orange curves) and left side of vertebra (red and blue curves).

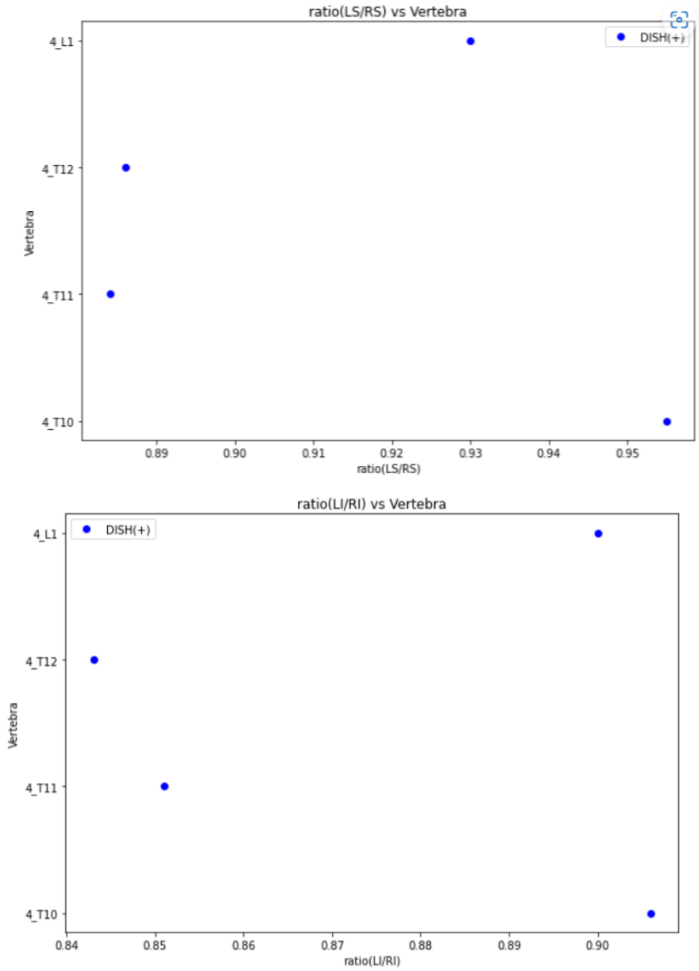

Figure 6.37: Comparison of the ratio LS/RS (figure at the top) and ratio LI/RI (figure at the bottom) for each vertebra from Image 4. The blue points refer to the pathological (DISH(+)) vertebrae.

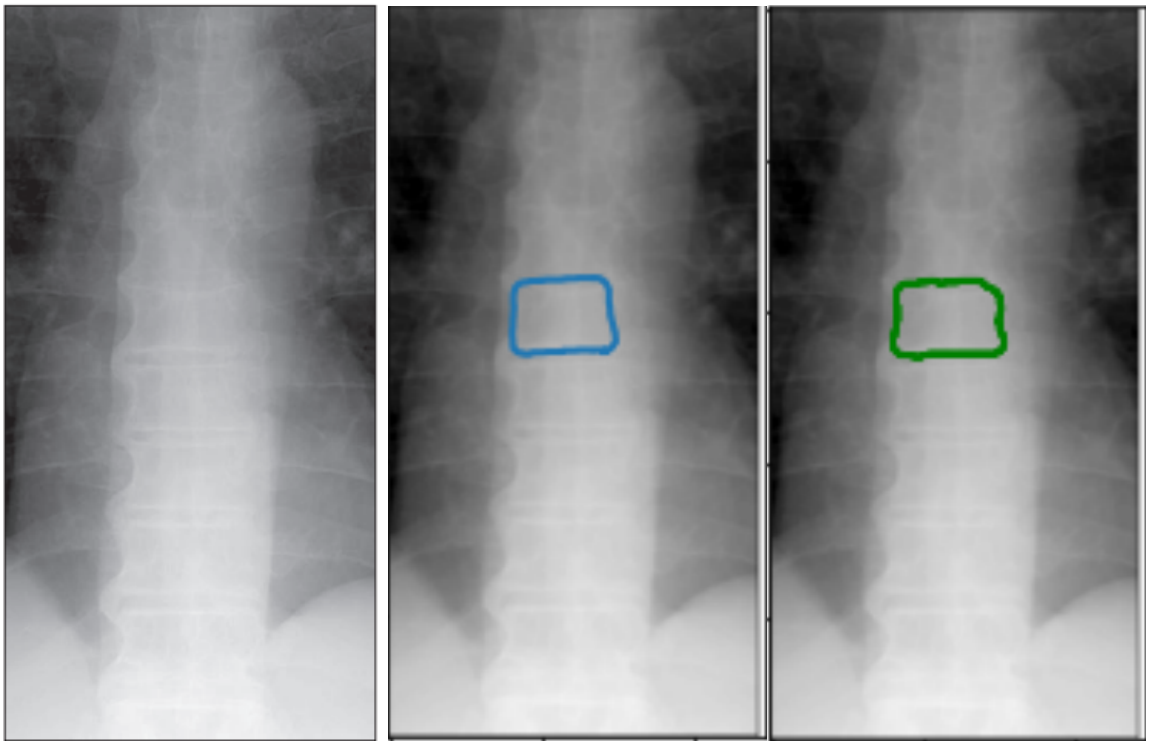

Figure 6.38: Initial level-set and segmentation result for T7 from Image 5. Image on the left: Initial level-set (blue curve) used for segmentation of that vertebra; Image on the right: Segmentation result (green) for the correspondent vertebra.

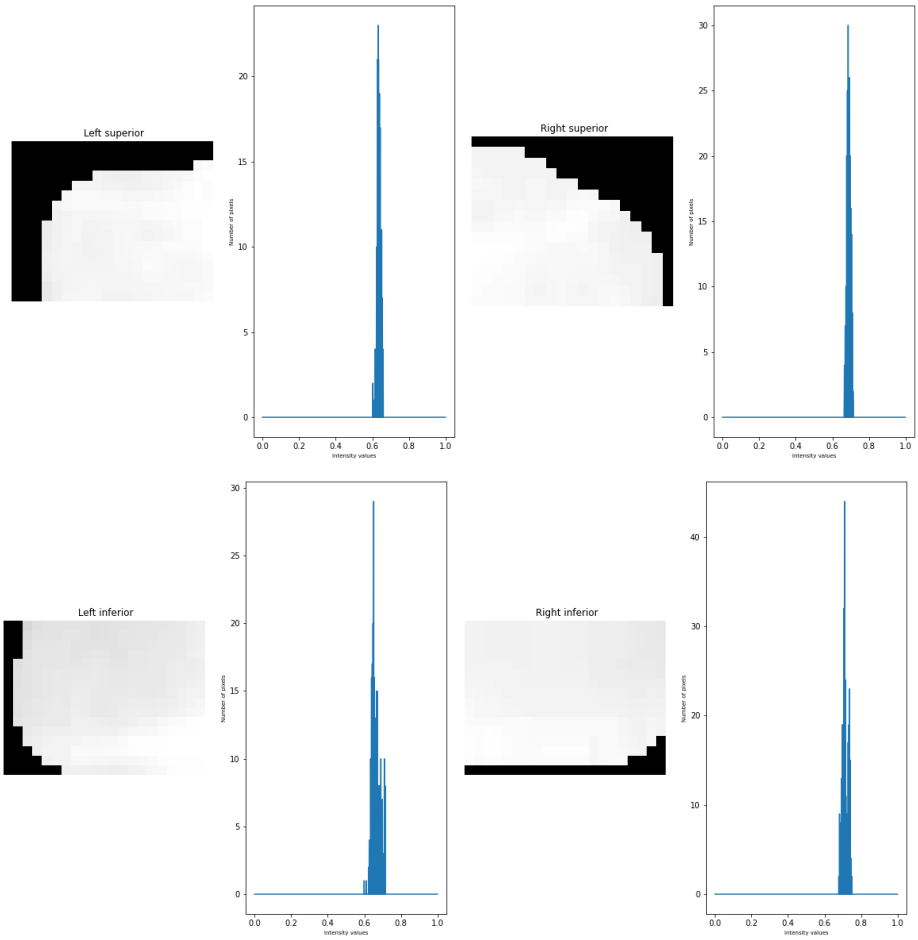

Figure 6.39: Comparison of each corner and its histograms for the T7 vertebra from Image 5.

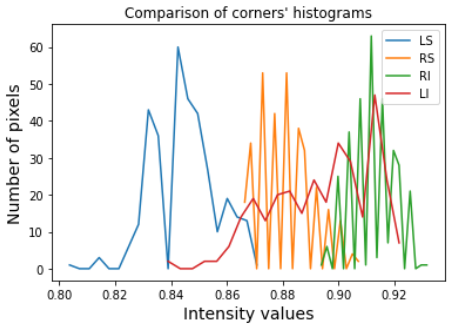

Figure 6.40: Comparison of all corners' histograms for T7 from Image 5, showing the difference between right side (green and orange curves) and left side of vertebra (red and blue curves)

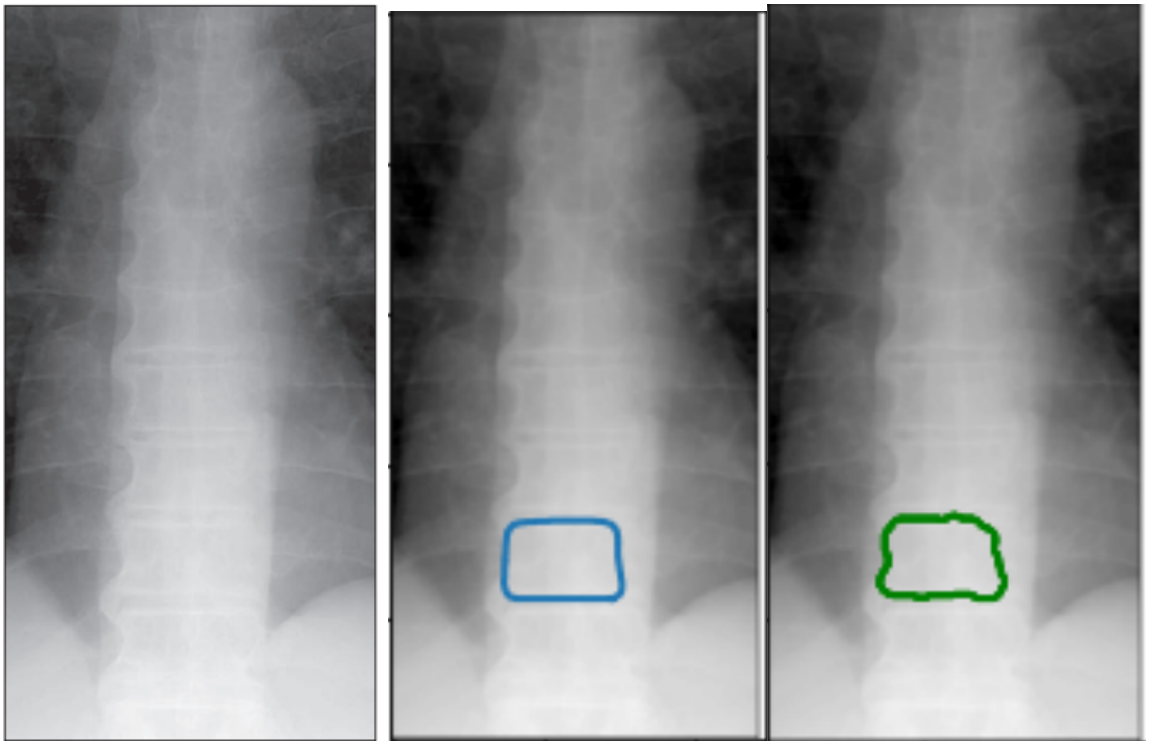

Figure 6.41: Initial level-set and segmentation result for T10 from Image 5. Image on the left: Initial level-set (blue curve) used for segmentation of that vertebra; Image on the right: Segmentation result (green) for the correspondent vertebra.

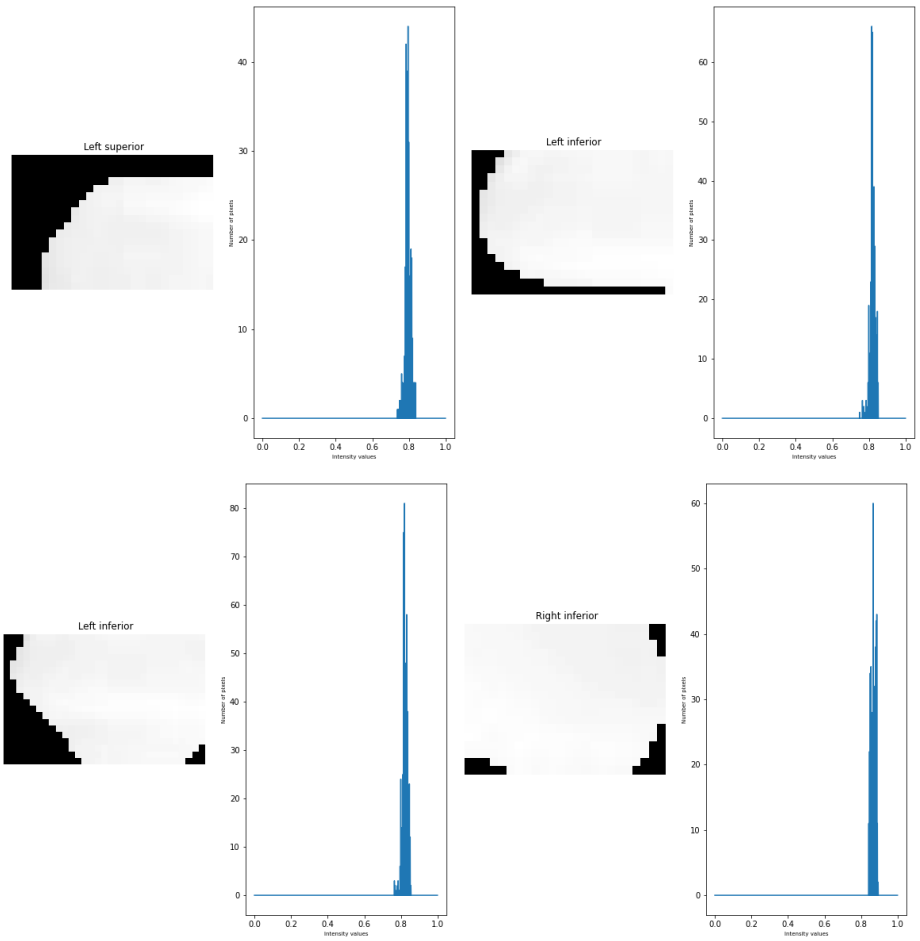

Figure 6.42: Comparison of each corner and its histograms for the T10 vertebra from Image 5.

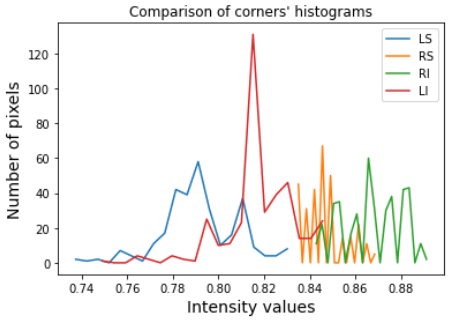

Figure 6.43: Comparison of all corners' histograms for T10 from Image 5, showing the difference between right side (green and orange curves) and left side of vertebra(red and blue curves).

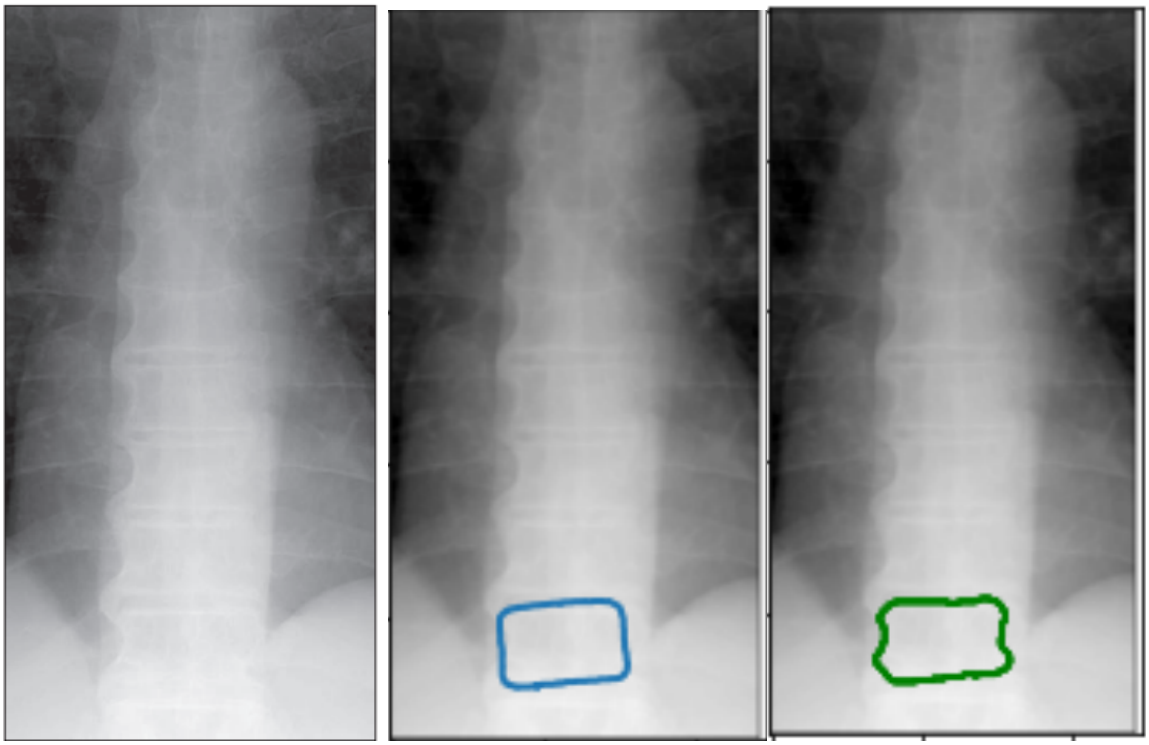

Figure 6.44: Initial level-set and segmentation result for T11 from Image 5. Image on the left: Initial level-set (blue curve) used for segmentation of that vertebra; Image on the right: Segmentation result (green) for the correspondent vertebra.

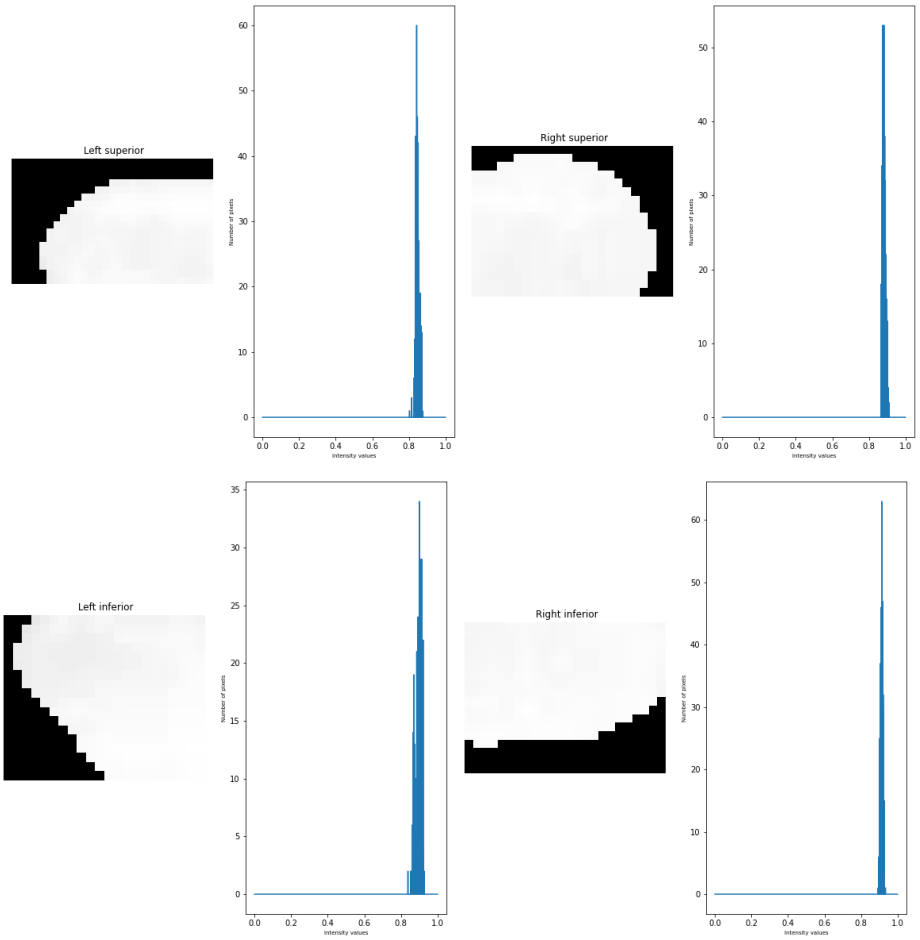

Figure 6.45: Comparison of each corner and its histograms for the T11 vertebra from Image 5.

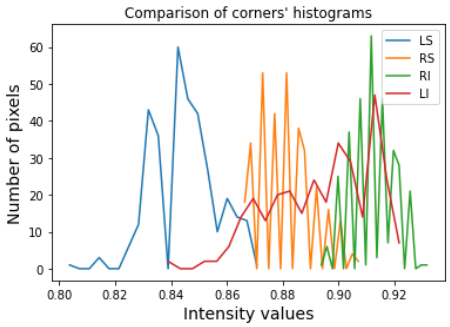

Figure 6.46: Comparison of all corners' histograms for T11 from Image 5, showing the difference between right side (green and orange curves) and left side of vertebra (red and blue curves).

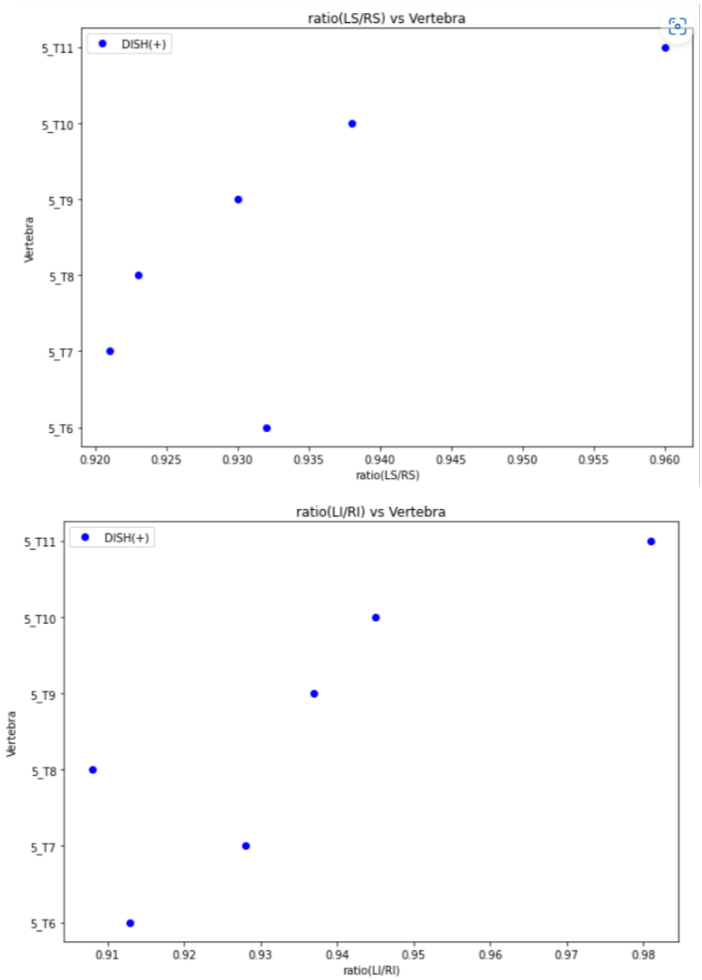

Figure 6.47: Comparison of the ratio LS/RS (figure at the top) and ratio LI/RI (figure at the bottom) for each vertebra from Image 5. The blue points refer to the pathological (DISH(+)) vertebrae.

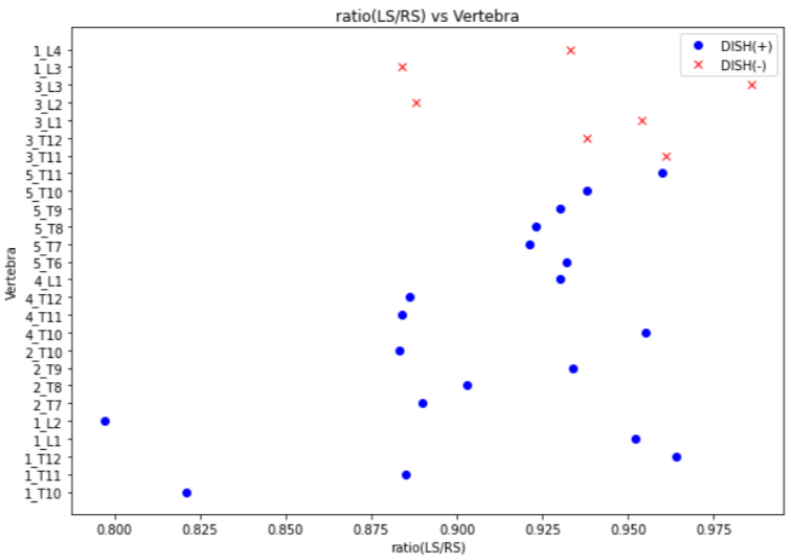

Figure 6.48: Representation of LS/RS ratio values for all vertebrae. Each vertebra is identified by the two components, according to the following example: image_numberofvertebra. Also, the vertebrae in blue correspond to pathological vertebrae and the red ones correspond to non-pathological vertebrae.

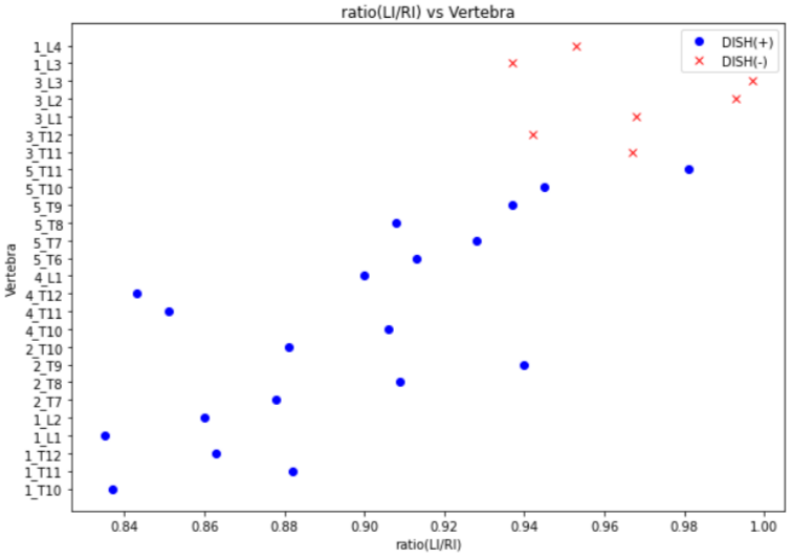

Figure 6.49: Representation of LI/RI ratio values for all vertebrae. Each vertebra is identified by the three components according to the following example: image_vertebra.Also, the vertebrae in blue correspond to pathological vertebrae and the red ones correspond to non-pathological vertebrae.

7

Discussion of DISH vertebrae segmentation and analysis results

7.1 Image 1

Regarding Image 1, in Figure 4.1, it was provided the segmentation and analysis for seven vertebrae. Five of these are pathological (vertebrae L2-T10) and the other two (vertebrae L4 and L3) are non-pathological. By visual inspection of the X-ray image, it is possible to notice a whiter appearance in the right side of the pathological vertebrae regarding the left side. This due to the ossifications originated by DISH.

By visual inspection of the segmentations results, presented in Figures 6.1,6.4, 6.7, 6.10), III.1,III.4, III.7(in the Annex III, section III.1), it is possible to conclude that the segmentation was able to capture the specific morphology of each vertebra, with slightly differences near the corners, where DISH manifests. Despite this, there were difficulties with two particular vertebrae: vertebra L1 and vertebra L4. Regarding the vertebra L1, Figure 6.4 shows the segmentation results and it is noticeable that the segmentation presents also some small errors along the contour of the vertebra. This is due to the presence of local maximum intensities, which make the contour evolution to stop in those locations. Also, the right inferior corner of this vertebra possesses a great intensity which enables the algorithm to find the right contour and, then, the segmentation is not perfect in the location. Regarding the vertebra L4, whose segmentation is found in 6.10, it was not possible to provide the segmentation for the inferior corners. Those corners display lower intensities (lower grayscale value) than other regions around, forcing the algorithm to propose erroneous convergence minima.

Regarding the histograms, it was expected that in pathological vertebrae, there would be differences in the histograms between right corners and the correspondent left corners. After analysis of the histograms, it is possible to conclude that in the pathological vertebrae, the histograms for the right corners are displaced to the right (more intensity) that the correspondent left corners. It is also important to notice that in vertebra T12, whose segmentation is present in Figure III.5, the ossifications are found, in greater extent, in

the right inferior corners. That is the reason why, in this vertebra, only the Right Inferior corner histogram is more displaced to the right. This is possible to be seen in Figure III.6.

Regarding the non-pathological vertebrae, there is no much difference between the correspondent corners' histograms, as seen in Figure 6.9, for vertebra L3, and in Figure 6.12, for vertebra L4. Nonetheless, it is possible to notice a slightly deviation in the right superior corner histogram for vertebra L3 regarding the left superior corner.

In agreement with what was observed in the previous paragraphs, the analysis of the intensities and ratios, as seen in the Table 6.1, reveal that the intensities values are bigger in pathological corners, specially the Right Inferior corner(RI), where this difference is more noticeable. These values are dependent on the severity of the disease in that corner. disease in that corner. To be more specific, more severity means higher intensity of the pixels in the image. Thus, the vertebrae with more severity are T11 and T10, since they present a higher Right inferior corner average grayscale value.

Concerning the ratios, values close to 1 reveal that correspondent corners have comparable average intensity values, which may suggest the absence of pathology. Values clearly superior to or inferior to 1 suggest that there is a corner with more intense pixels. This, in its turn, suggest an additional calcification of the corner, leading to a proposal of classification as a corner presenting signals of DISH.

The ratios values for pathological vertebrae(DISH(+)) reveal the ratio(LI/RI) is the ratio with the lesser values(range from [0.837:0.891], when comparing with ratio(LR/RS) (range [0.821:0.956]). Comparing these with the ratios from non-pathological vertebrae, DISH(-), visible at the Left of Figure 6.13, it is clear that the intensities of these latter corners present much closer levels of intensity.

Taking this into account, the ratio LI/RI seems to be a good metric to use to differentiate DISH from NON-DISH vertebrae.

7.2 Image 2

For this image, the segmentations of four pathological vertebrae (T7-T10) were provided. In this image, seen in Figure 4.2, it is possible to verify that the right side appears whiter when compared to the left side. This finding is the result of ossifications caused by DISH.

The segmentation process in this image was a little difficult. As it possible to see in Figure 4.2, there are spiny edges in the left side of vertebrae, making it difficult the segmentation. However, by visual inspection of the segmentations, presented in Figures 6.14, 6.17, III.10,III.13 (in the Annex III, section III.2), there was a good performance, although not perfect, specially in the left side, where the edges are not clearly seen.

Regarding the histograms, since this image is a pathological image, it was once again expected that in pathological vertebrae, there would be differences in the histograms between right corners and the correspondent left corners. The analysis of these histograms confirmed this expectation, because there was a displacement for the right (more intensity) of the right corners (pathological) over the left ones (non-pathological).

The analysis of intensities and the ratios, as seen in the Table 6.2, reveal that the intensities values are bigger in pathological corners, specially the Right Inferior corner(RI), where this difference is more noticeable. However, both ratios (LI/RI) and (LR/RS) are very similar with values as big as 0.94 for the former and 0.934 for the latter. Although that, most the ratios are lower than 0.91, depending on the extent of ossifications.

7.3 Image 3

Image 3, seen in Figure 4.5, is a non-pathological image and the segmentations and analysis of five vertebrae (L3-T11) were provided. The visualizations of the image shows that there is no significant difference between both sides of vertebrae.

Concerning Image 3 segmentation results, presented in Figs 6.21,6.24,6.27, III.16,III.19 (in the Annex III, section III.3), by visual inspection of them, it is possible to state that the algorithm had a very good performance, except for the vertebra T12, seen in Figure 6.22. This vertebra has a very difficult morphology and the algorithm was not able to provide the segmentation of all the contour of the vertebra, specially the inferior corners, which are very sharp.

The vertebrae of this image, except the superior corners from the T11 vertebra, don't seem present large intensity values. Thus, the results should demonstrate that there are no differences in the intensities between the two sides of vertebrae.

The analysis of the histograms showed that there was no significant difference in the histogram distributions for each pair of corners, which is in according to expected. Moreover, the values of intensities, as seen in Figure 6.3, are not very different from one corner to another, specially between the correspondent corners. The results obtained for ratios were high(>=0.89), with most of the vertebrae having values bigger than 0.95. Of the two ratios, the ratio LI/RI stood out for having values closer to 1. Here, the vertebra T12 had the smallest value, which is due to the inaccuracy of the segmentation.

These results, once gain, emphasizes the idea that there is no significant difference between the two sides, suggesting that there is no pathology.

7.4 Image 4

Image 4, seen in Figure 4.3, is a pathological image and the right side is the pathological side. It is from the same person as Image 3 but 14 years later, now aged 64. By that time, the patient had already been diagnosed with DISH. Here, four vertebrae (T10-L1) were segmented and analysed.

The segmentation results obtained for this image, presented in Figures 6.34, 6.31, III.22, III.25(in the Annex III, section III.4), were acceptable, because the algorithm was able to capture the specific morphology of each vertebrae, although, locally, the segmentation, for example, of the Figure 6.31, possesses slight deviations to the real contour.

Through the analysis of the histograms for each vertebra, similar to what was observed in other pathological vertebrae before, it was possible to verify a displacement of the right corners' histograms to the right (bigger intensities) regarding the left ones. Once again, the cause of this was the ossifications caused by DISH.

The intensities values, as seen in Figure 6.4, for each corner were also clear. The right corners have bigger average intensities when comparing to the correspondent left corners, specially the inferior ones, where this difference is more evident. In this table, it is also noticeable the values for the ratio LI/RI. These values are lower or equal to 0.90, approximately, when, in the ratio LS/RS, the range of values go from 0.88 to 0.95, approximately. Thus, once again, the ratio LI/RI stands out and it is important to highlight that the ratio LI/RI may be a good metric to differentiate the pathological vertebrae from the non-pathological ones.

7.5 Image 5

In this image, the segmentation and analysis of six pathological vertebrae (T11-T6) was provided. This image can be found in 4.4 and It is noteworthy that in this image it is not possible to exactly see the boundaries of the vertebrae in the right side, since the image is very noisy. The presence of noise had a great impact on the segmentation results, presented in Figures 6.38, 6.41, 6.44, III.31,III.28, III.34 (in the Annex III, section III.5), specially of the vertebra represented in Figure 6.44. Despite that, the segmentation results for the vertebrae showed that it was possible to capture the morphology of each one.

By comparing the histograms for each pair of correspondent corners and for each vertebrae, it is possible to conclude that, as seen in other pathological images, there is a deviation to the right for corners in a pathological state, although in T11 , the histograms distribution for the inferior corners were pretty close, as it is possible to see in Figure 6.46.

Thus, the intensities values, as seen in Figure 6.5, show that for all vertebrae, except T11, the intensity values are bigger in the pathological side (right side, in this image), empathizing the difference between the pathological and non-pathological side.

Regarding the ratios LS/RS and LI/RI, the values for the former are lower than 0.96. In the the latter, the values are lower than 0.981, but most of them are lower or equal than 0.945. Also, it is necessary to say the values 0.96 and 0.981 correspond to the vertebra T11. In this, both sides appear very similar in terms of intensity values. Since in this image, and particularly in this vertebra, the right side is very noisy, it was not possible to obtain the right segmentation of the vertebra. Thus, it explains why the value here is different from the other DISH vertebrae.

7.6 General Discussion of results

After looking into each specific image results, it is possible to retrieve some general results: From the seventeen pathological vertebrae (except one) analysed, the pathological corners

histograms were displaced to the right when comparing to the correspondent corners histograms in the left side. Regarding the six non-pathological vertebrae, there was no significant difference in the histograms between each pair of corners.

Concerning the ratios values, sixteen pathological vertebrae have values equal or lower than 0.945 and only one have a value of 0.981, for ratio LI/RI. The same ratio for the seven non-pathological vertebrae have values closer to 1. This is graphically represented in Figure 6.49.

Then, it is possible to conclude that the ratio LI/RI may be a good indicator of the presence of ossifications caused by DISH, due to it's capacity of differentiating DISH corners from NON-DISH corners.

8

Conclusion

8.1 Main conclusions

One of objectives of this work was to develop a algorithm to provide a patient specific segmentation of vertebrae and, then, compare its performance on two radiographs with the previous work [18] and the mannual annotations of experts.

Then, use this algorithm to provide the segmentation of DISH vertebrae, in order to analyse them, based on the pattern of ossifications on them, with goal of finding a metric capable of differentiating pathological from non-pathological vertebrae.

The ultimate goal of this work is to contribute to the construction of diagnosing tool of DISH based on coronal spine radiographs.

In this work, it was developed an algorithm which allows the segmentation of pathological and non-pathological vertebrae. This algorithm follows the morphological geodesic active contour formulation and, comparing with the traditional active contour formulation, it is faster and requires less number of iterations. Also, the initial level-set curve used in this approach comprises the region of interest, that is, the vertebrae, and, as it evolves, the curve changes it's morphology, in order to adapt to the specific morphology of the vertebrae, which was quite important for this work.

The segmentation performance evaluation, whose results are shown in chapter 5, revealed that this algorithm has brought an improvement to the segmentations originated by the algorithm developed by [18]. Also, the segmentation performance is comparable to the ones done by experts, that is, *Annot 1* e *Annot2*.

Regarding the results obtained for DISH images showed in chapter 7, the algorithm developed in this work has a good performance on providing the segmentation of pathological vertebrae, even for very low- quality images, such as the radiographs presented in Figures 4.2 and 4.4. The algorithm provided specific vertebrae segmentation and this was of utmost importance for the posterior analysis, which was accomplished by dividing each vertebra in nine squares, and considering only the corners for evaluation, based on the characteristics of DISH in vertebrae.

This evaluation was accomplished by analysing the histograms of the corners and

making a comparison between the correspondent ones. The histograms assessment clearly show that there is a significant difference between the non-pathological corners and the correspondent pathological, in pathological vertebrae. The contrary is found in the non-pathological vertebrae.

Although the histogram-based results show promising abilities to differentiate pathological from non pathological corners, this finding was not enough to provide this differentiation. Thus, it was necessary to use a different metric to emphasize this difference. To do so, it was necessary to take into account the approximate symmetry between the two sides of the vertebrae (Left and Right) and the shape of the histograms distributions. Since the histogram in all vertebrae follow, approximately, a Gaussian distribution, it was reasonable to use the average value in each corner to represent the intensity value in those areas. It was proposed to compute two ratios: Left Superior corner mean value / Right Superior corner mean value (LS/RS) and Left Superior corner mean value / Right Superior corner mean value (LI/RI). The results were very promising, showing that the ratio LI/RI seems to have a good performance on making this differentiation more noticeable, as seen in Figure 6.49.

The introduction of this measure is clearly innovative, since no work was found, in the literature, with a similar approach. Despite this, it would be necessary to confirm it in a higher extent the viability of this metric by segmenting more vertebrae with DISH and non-DISH vertebrae.

Despite these results, the segmentation evaluation was performed only in two images and, to confirm the improvement this algorithm has brought to the segmentation of vertebrae, it would be necessary to prove it in more images.

Also, regarding the segmentation results, some vertebrae features, for example, spiny edges, make it hard to segment. Also, the presence of noise, such as in Figure 8.1, where the boundaries, on the right side, are ambiguous, difficult this process. These issues have also been reported in other works such as in [82] and [48].

Besides that, although the promissing results concerning the analysis of vertebrae, it would be as well necessary to confirm the promissing ability of the ratio LI/RI in differentiating pathological from non pathological vertebrae in more images.

8.2 Limitations

The work presented in this Dissertation came across with some limitations Firstly, it was not possible to generate the initial contours, by using the algorithm created by [18], specific for each image of the dataset. A possible explanation is that the generic models created by Viegas are from non-pathological images and, therefore, the algorithm is not ideal for. Thus, to accomplish this work, it was used a vector of contours provided by the same algorithm, however, from a non-pathological image with a different size. This led to the need of applying affine transformations, such as scaling and translations, in order to set the contours in the surroundings of each vertebra.

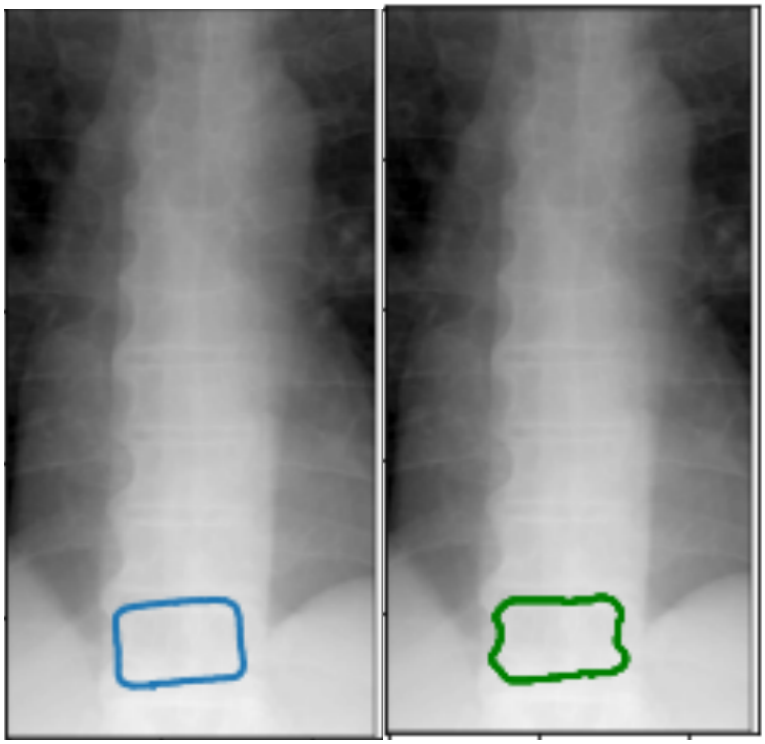

Figure 8.1: Low-quality image from dataset with ambiguous edges. Image on the left: Initial contour (blue curve) used for segmentation of that vertebra; Image on the right: Segmentation result(green) for the correspondent vertebra.

Other limitations of this work are related with the algorithm itself. This algorithm is semi-automatic with a very heavy dependence on the user. This is seen, for example, in the position of the initial level-set, as it is possible to see in Figure 4.12, where small variations of the initial level-set can lead to different segmentations. Therefore, it is a cumbersome process, since the initial level-set must be set in a certain position, in order to provide the desirable segmentation.

Moreover, this algorithm depends on the inverse edge map of the image to be segmented. The presence of noise and other non-important features, such as ribs or spiny processes, affect in great extent the final segmentation, because the initial level-set, as it evolves, can get trapped in these false edges, leading to innacurate segmentations. Hence, it is really necessary to diminish the effect of the structures, by applying noise filters or using thresholds filters. Also, it is very important to increase the contrast and visualization of vertebrae edges, by applying a local histogram equalization, for example, in order to create the inverse edge map able to provide a good segmentation.

Finally, the morphological geodesic active contours algorithm depends on three arguments: number of iterations, the smoothing parameter and the balloon force parameter. These parameters must be chosen according to the characteristics of the images: image size and the quality of the inverse edge map, for example. The first affects widely the time of computations, which is, as well, dependent on computer hardware features. Essentially, the greater the size of the image, the greater the number of iterations. Also, the better the

computer features(i.e,larger RAM or more processors) decrease the time of computation. For example, by using the computer features used in this work(described in chapter 3.1.7), images sizes with nearly 5000 by 2000 in the smaller dimension, and for 300 iterations, the time of computation can take up to 3 h for vertebra. However, the images used in this work were smaller, and for 300 iterations, the algorithm took approximately 5 minutes per vertebra. On the other side, the second parameter will affect the evolution and deformation of the initial curve because, in this image, the edges are emphasized in order to push the contour towards them. In the best situation, the edges must be the only ones emphasized, otherwise, other features, such as noise, may be enhanced and prevent the curve to fit perfectly to the object boundaries.

Other parameters the algorithm performance is dependent on are the the smoothing parameter and balloon force parameters. The first is used to to smooth the contour as it evolves, at each iteration, and is dependent the amount of noise and false edges present in the image, which can degrade the contour. On the other hand, the Balloon force must be chosen carefully, according to the image forces(inverse edge map). It cannot be either too small or too big, otherwise the contour will not be found.

8.3 Future Work

As said before, this work depends widely on the user to set the initial contour in the surroundings of the vertebra, making this process very cumbersome. Hence, in future work, it is recommended to make this algorithm fully automatic or almost fully automatic, which will pass by creating an algorithm able to find the exact position of initial level-set. To accomplish this, firstly, it would be important as well to solve the problem of obtaining the contours for the DISH images by using the algorithm by [18]. This algorithm enables the finding the Region of Interest of each vertebrae and its average contour, which can be useful in finding the initial level-set. Moreover, this algorithm provides the Cobb Angle. This parameter enables the quantification of spinal deformities and has been associated with DISH, in older patients[34]. This finding will certainly help doctors to make a better decision and possibly evaluate the progression and severity of the disease. Another problem reported in this work is the presence of spine edges in the segmentation process, making it difficult. Thus, it is also a feature which needs to be solved.

Another possible work for the future could be the differentiation of this disease from AS. These diseases are very similar since both lead to new bone growth but one difference is that AS is a inflammatory disease. Since X-ray images do not provide insight into inflammatory changes, this image modality is not the best to differentiate these two diseases. However, there is one difference between two disease, which can be assessed through radiographs. According to the Resnick Criterion, one of the criteria for DISH diagnoses is the lack of degenerative changes of intervertebral disk. AS, however, can be a risk factor for degenerative changes in the intervertebral disk, according to [83], due to the higher predispostion of to atherosclerosis. As result, the arteries supplying blood to the

disc no longer are able to provide it, leading to the degeneration of the disc. In radiographs, if there is disc degeneration, this can be seen as the narrowing of the intervertebral disc space. Thus, this feature can be possibly used for differentiating DISH from AS.

Although the present work did not aim to create a classification algorithm, possibly with a very huge dataset, a machine learning or deep learning model could be implemented to segregate DISH from NON-DISH vertebrae. One could use then Supervised learning models, such as K-means algorithm or Support Vector Machine. Also, a deep learning approach could be able to find subtle structural changes in the corners of pathological vertebrae to assess the progression and severity of the disease, like the increase of the size of ossifications, just like in the work done in [45].

Bibliography

[1] J. M. Lourenço. *The NOVAthesis LaTeX Template User's Manual*. NOVA University Lisbon. 2021. URL: https://github.com/joaomlourenco/novathesis/raw/master/template.pdf (cit. on p. iii).

[2] I. Olivieri et al. "Diffuse idiopathic skeletal hyperostosis: Differentiation from ankylosing spondylitis". In: *Current Rheumatology Reports* vol.11,no.5, (2009-10), pp.321–328. DOI: 10.1007/s11926-009-0046-9. URL: https://doi.org/10.1007/s11926-009-0046-9 (cit. on pp. 1, 4, 12).

[3] P. Kosmidou et al. "Cervical Diffuse Idiopathic Skeletal Hyperostosis: Rare Cause of Emergency Tracheostomy". In: *Cureus*, 14.1 (2022-01), pp.e20925. DOI: 10.7759/cureus.20925. URL: https://doi.org/10.7759/cureus.20925 (cit. on p. 1).

[4] R. Mader et al. "Imaging of diffuse idiopathic skeletal hyperostosis (DISH)". In: *RMD Open* vol.6,no.1, (2020-02), pp.e001151. DOI: 10.1136/rmdopen-2019-001151. URL: https://doi.org/10.1136/rmdopen-2019-001151 (cit. on pp. 2, 3, 13).

[5] J. H. Lee et al. "Swallowing Difficulty in Diffuse Idiopathic Skeletal Hyperostosis with Metabolic Syndrome". In: *Korean Journal of Neurotrauma*, vol.16.no.1 (2020-04), pp. 90–98. DOI: 10.13004/kjnt.2020.16.e4. URL: https://doi.org/10.13004/kjnt.2020.16.e4 (cit. on p. 1).

[6] Y. Yoshimatsu et al. "Management of Airway Obstruction due to Diffuse Idiopathic Skeletal Hyperostosis in the Cervical Spine: A Case Report and Literature Review". In: *Internal Medicine*, vol.58,no.2, (2019-01), pp.271–276. DOI: 10.2169/internalmedicine.1071-18. URL: https://doi.org/10.2169/internalmedicine.1071-18 (cit. on p. 1).

[7] J. J. Allensworth, K. D. O'Dell, and J. S. Schindler. "Bilateral vocal fold paralysis and dysphagia secondary to diffuse idiopathic skeletal hyperostosis". In: *Head &amp Neck* 39.1 (2016-08), E1–E3. DOI: 10.1002/hed.24569. URL: https://doi.org/10.1002/hed.24569 (cit. on p. 1).

[8] J. T. Bakker et al. "Morphological characteristics of diffuse idiopathic skeletal hyperostosis in the cervical spine". In: *PLOS ONE*, 12,11, (2017-11). Ed. by R. D. Blank, pp.e0188414. DOI: 10.1371/journal.pone.0188414. URL: https://doi.org/10.1371/journal.pone.0188414 (cit. on pp. 1, 2, 11, 13, 14).

[9] I. Bickle. *Normal lateral cervical spine radiograph*. 2016-07. DOI: 10.53347/rid-46395. URL: https://doi.org/10.53347/rid-46395 (cit. on p. 3).

[10] R. Mader et al. "Diffuse idiopathic skeletal hyperostosis (DISH): where we are now and where to go next". In: *RMD Open*, vol.3,no.1, (2017-06), pp.e000472. DOI: 10.1136/rmdopen-2017-000472. URL: https://doi.org/10.1136/rmdopen-2017-000472 (cit. on pp. 2, 3, 12).

[11] P. Ambrosino et al. "Diffuse idiopathic skeletal hyperostosis in subjects with congestive heart failure undergoing cardiac rehabilitation: A decision tree analysis". In: *Journal of Rehabilitation Medicine* vol.52,no.3 (2020), jrm00030. DOI: 10.2340/16501977-2658. URL: https://doi.org/10.2340/16501977-2658 (cit. on p. 2).

[12] G. Vezyroglou, A. Mitropoulos, and C. Antoniadis. "A metabolic syndrome in diffuse idiopathic skeletal hyperostosis. A controlled study". In: *J. Rheumatol.* vol.23,no.4, (1996-04), pp. 672–676 (cit. on p. 2).

[13] H. Julkunen et al. "The epidemiology of hyperostosis of the spine together with its symptoms and related mortality in a general population". In: *Scand. J. Rheumatol.*, vol.4,no.1, (1975), pp. 23–27. DOI: 10.1080/03009747509095610. URL: https://doi.org/10.1080/03009747509095610 (cit. on pp. 2, 11).

[14] P. D. Utsinger. "Diffuse Idiopathic Skeletal Hyperostosis". In: *Clinics in Rheumatic Diseases* 11.2 (1985-08), pp. 325–351. DOI: 10.1016/s0307-742x(21)00544-0. URL: https://doi.org/10.1016/s0307-742x(21)00544-0 (cit. on pp. 2, 12).

[15] M. Yunoki et al. "The Importance of Recognizing Diffuse Idiopathic Skeletal Hyperostosis for Neurosurgeons: A Review". In: *Neurologia medico-chirurgica*, 56,8, (2016), pp. 510–515. DOI: 10.2176/nmc.ra.2016-0013. URL: https://doi.org/10.2176/nmc.ra.2016-0013 (cit. on pp. 2, 12).

[16] D. Moore. *DISH (diffuse idiopathic skeletal hyperostosis)*. https://www.orthobullets.com/spine/2045/dish-diffuse-idiopathic-skeletal-hyperostosis. Accessed in: 2022-02-07 (cit. on pp. 3, 12).

[17] M. Dąbrowski and Ł. Kubaszewski. "Diffuse Idiopathic Skeletal Hyperostosis of Cervical Spine with Dysphagia—Molecular and Clinical Aspects". In: *International Journal of Molecular Sciences* 22.8 (2021-04), p. 4255. DOI: 10.3390/ijms22084255. URL: https://doi.org/10.3390/ijms22084255 (cit. on pp. 3, 12).

[18] R. S. Viegas. "Development of a model of the spinal vertebral bodies based on x-ray images". Dissertation to obtain the Masters Degree in Biomedical Engineering. MA thesis. 2021 (cit. on pp. 3, 4, 12, 19, 20, 47, 52–54, 61, 62, 105, 106, 108).

[19] N. Nishida et al. "Biomechanical Analysis of the Spine in Diffuse Idiopathic Skeletal Hyperostosis: Finite Element Analysis". In: *Applied Sciences*, 11,19, (2021-09), pp.8944. DOI: 10.3390/app11198944. URL: https://doi.org/10.3390/app11198944 (cit. on pp. 3, 12, 15).

[20] M. G. Popova. ""Importance of Conventional Radiography in the Diagnosis of Diffuse Idiopathic Skeletal Hyperostosis"". In: *Biomedical Journal of Scientific &amp Technical Research*, vol.35,no.3, (2021-04). DOI: 10.26717/bjstr.2021.35.005705. URL: https://doi.org/10.26717/bjstr.2021.35.005705 (cit. on p. 3).

[21] D. T. D. V. Lopes. "Segmentação semiautomática de imagens com vista ao estudo da Hiperostose Esquelética Idiopática Difusa". Dissertation to obtain the Masters Degree in Biomedical Engineering. MA thesis. 2019 (cit. on pp. 4, 19, 20).

[22] B. Frost, S. Camarero-Espinosa, and E. Foster. "Materials for the Spine: Anatomy, Problems, and Solutions". In: *Materials* vol.12,no.2, (2019-01), pp.253. DOI: 10.3390/ma12020253. URL: https://doi.org/10.3390/ma12020253 (cit. on p. 7).

[23] F. Netter. *Atlas of human anatomy*. Philadelphia, PA: Saunders/Elsevier, 2006. ISBN: 9781416033851 (cit. on pp. 8, 10).

[24] *The vertebral collumn*. https://teachmeanatomy.info/back/bones/vertebral-column/. (Accessed in: 2022-01-20) (cit. on pp. 8, 9).

[25] A. Waugh. *Ross and Wilson anatomy & physiology in health and illness*. Edinburgh New York: Churchill Livinstone Elsevier, 2014. ISBN: 978-0-7020-5326-9 (cit. on p. 9).

[26] P. D. Ross et al. "A new method for vertebral fracture diagnosis". In: *Journal of Bone and Mineral Research*, vol.8,no.2, (2009-12), pp.167–174. DOI: 10.1002/jbmr.5650080207. URL: https://doi.org/10.1002/jbmr.5650080207 (cit. on p. 9).

[27] C. Daniel and M. Elliott. *The Intervertebral Disc: Overview of Disc Mechanics*. Vienna, Austria: Springer, 2014. ISBN: 978-3-7091-1534-3 (cit. on p. 10).

[28] *Intervertebral Disc*. https://www.physio-pedia.com/Intervertebral_disc. Accessed: 2022-01-17 (cit. on p. 9).

[29] *Anatomy of Spine*. https://mayfieldclinic.com/pe-anatspine.htm. Accessed in: 2022-01-17 (cit. on p. 10).

[30] M.-H. Horng et al. "Cobb Angle Measurement of Spine from X-Ray Images Using Convolutional Neural Network". In: *Computational and Mathematical Methods in Medicine*, 2019 (2019-02), pp.1–18. DOI: 10.1155/2019/6357171. URL: https://doi.org/10.1155/2019/6357171 (cit. on p. 11).

[31] J. Bushberg. *The essential physics of medical imaging*. Philadelphia: Wolters Kluwer Health/Lippincott Williams & Wilkins, 2012. ISBN: 978-0-7817-8057-5 (cit. on p. 11).

[32] J. Prince. *Medical imaging signals and systems*. Upper Saddle River, NJ: Pearson Education, 2015. ISBN: 9780132145183 (cit. on p. 11).

[33] D. C. Quintero-González, Á. Arbeláez-Cortés, and J. M. Rueda. "Clinical and radiological characteristics of diffuse idiopathic skeletal hyperostosis in two medical centers in Cali, Colombia: Report of 24 cases". In: *Revista Colombiana de Reumatología (English Edition)* 27.2 (2020-04), pp. 80–87. DOI: 10.1016/j.rcreue.2020.01.005. URL: https://doi.org/10.1016/j.rcreue.2020.01.005 (cit. on pp. 11, 12).

[34] L. Nardo et al. "Diffuse Idiopathic Skeletal Hyperostosis Association With Thoracic Spine Kyphosis". In: *Spine*, 39.24 (2014-11), pp.1418–1424. DOI: 10.1097/brs.0000000000000615. URL: https://doi.org/10.1097/brs.0000000000000615OsYa (cit. on pp. 13, 16, 108).

[35] M. Østergaard and R. G. Lambert. "Imaging in ankylosing spondylitis". In: *Therapeutic Advances in Musculoskeletal Disease* 4.4 (2012-02), pp. 301–311. DOI: 10.1177/1759720x11436240. URL: https://doi.org/10.1177/1759720x11436240 (cit. on pp. 14, 15).

[36] M. S. Taljanovic et al. "Imaging characteristics of diffuse idiopathic skeletal hyperostosis with an emphasis on acute spinal fractures: *review*". In: *AJR Am. J. Roentgenol.*, vol.193,no.3, (2009-09), pp.10–19. DOI: doi:10.2214/AJR.07.7102. URL: https://doi.org/10.2214/AJR.07.7102 (cit. on pp. 15, 16, 42–44, 46, 58).

[37] L. Westerveld et al. "Clinical outcome after traumatic spinal fractures in patients with ankylosing spinal disorders compared with control patients". In: *The Spine Journal*, vol.14,no.5, (2014-05), pp.729–740. DOI: 10.1016/j.spinee.2013.06.038. URL: https://doi.org/10.1016/j.spinee.2013.06.038 (cit. on p. 16).

[38] M.-H. Horng et al. "Cobb Angle Measurement of Spine from X-Ray Images Using Convolutional Neural Network". In: *Computational and Mathematical Methods in Medicine* 2019 (2019-02), pp. 1–18. DOI: 10.1155/2019/6357171. URL: https://doi.org/10.1155/2019/6357171 (cit. on p. 16).

[39] X. Huo et al. "An integrative framework for 3D cobb angle measurement on CT images". In: *Computers in Biology and Medicine* 82 (2017-03), pp. 111–118. DOI: 10.1016/j.compbiomed.2017.01.007. URL: https://doi.org/10.1016/j.compbiomed.2017.01.007 (cit. on p. 17).

[40] K. Yamada et al. "Spinopelvic alignment of diffuse idiopathic skeletal hyperostosis in lumbar spinal stenosis". In: *European Spine Journal*, 23.6 (2014-01), pp.1302–1308. DOI: 10.1007/s00586-013-3154-1. URL: https://doi.org/10.1007/s00586-013-3154-1 (cit. on p. 16).

[41] S. Mata et al. "Comprehensive radiographic evaluation of diffuse idiopathicskeletal hyperostosis: Development and interrater reliability of a scoring system". In: *Seminars in Arthritis and Rheumatism* 28.2 (1998-10), pp. 88–96. DOI: 10.1016/s0049-0172(98)80041-3. URL: https://doi.org/10.1016/s0049-0172(98)80041-3 (cit. on p. 17).

[42] H. Misaki et al. "Can Diffuse Idiopathic Skeletal Hyperostosis Be Diagnosed by Plain Lumbar Spine X-Ray Findings Alone?" In: *Global Spine Journal*, vol.12,no.2, (2020-08), pp.198–203. DOI: 10.1177/2192568220948038. URL: https://doi.org/10.1177/2192568220948038 (cit. on p. 17).

[43] J. S. Kuperus et al. "Criteria for Early-Phase Diffuse Idiopathic Skeletal Hyperostosis: Development and Validation". In: *Radiology* 291.2 (2019-05), pp. 420–426. DOI: 10.1148/radiol.2019181695. URL: https://doi.org/10.1148/radiol.2019181695 (cit. on p. 17).

[44] S. Tan et al. "Computer Aided Evaluation of Ankylosing Spondylitis Using High-Resolution CT". In: *IEEE Transactions on Medical Imaging*, 27,9, (2008-09), pp.1252–1267. DOI: 10.1109/tmi.2008.920612. URL: https://doi.org/10.1109/tmi.2008.920612 (cit. on p. 18).

[45] B. S. Koo et al. "A pilot study on deep learning-based grading of corners of vertebral bodies for assessment of radiographic progression in patients with ankylosing spondylitis". In: *Therapeutic Advances in Musculoskeletal Disease*, vol.14, (2022-01). DOI: 10.1177/1759720x221114097. URL: https://doi.org/10.1177/1759720x221114097 (cit. on pp. 18, 109).

[46] T. A. Sardjono, A. F. H. Chozin, and M. Nuh. "Semi-Automatic Image Segmentation on X-ray Image of Spine using Active Contour Method". In: *JAREE (Journal on Advanced Research in Electrical Engineering)*, 5,2, (2021-10). DOI: 10.12962/jaree.v5i2.166. URL: https://doi.org/10.12962/jaree.v5i2.166 (cit. on p. 18).

[47] S. H. Shaikh, A. K. Maiti, and N. Chaki. "On Creation of Reference Image for Quantitative Evaluation of Image Thresholding Method". In: *Communications in Computer and Information Science*. Springer Berlin Heidelberg, 2011, pp. 161–169. DOI: 10.1007/978-3-642-27245-5_21. URL: https://doi.org/10.1007/978-3-642-27245-5_21 (cit. on p. 18).

[48] J. Huang et al. "An improved level set method for vertebra CT image segmentation". In: *BioMedical Engineering OnLine*, vol.12.no.1, (2013-05), pp.48–63. DOI: 10.1186/1475-925x-12-48. URL: https://doi.org/10.1186/1475-925x-12-48 (cit. on pp. 19, 38, 39, 106).

[49] P. Chinmayi, L. Agilandeeswari, and M. Prabukumar. "Survey of Image Processing Techniques in Medical Image Analysis: Challenges and Methodologies". In: *Advances in Intelligent Systems and Computing*. Vol. 614, Springer International Publishing, 2017-08, pp.460–471. DOI: 10.1007/978-3-319-60618-7_45. URL: https://doi.org/10.1007/978-3-319-60618-7_45 (cit. on p. 21).

[50] K. V. Thakur, O. H. Damodare, and A. M. Sapkal. "Poisson Noise Reducing Bilateral Filter". In: *Procedia Computer Science* 79 (2016), pp. 861–865. DOI: 10.1016/j.procs.2016.03.087. URL: https://doi.org/10.1016/j.procs.2016.03.087 (cit. on p. 21).

[51] N. Kumar and M. Nachamai. "Noise Removal and Filtering Techniques used in Medical Images". In: *Oriental journal of computer science and technology* 10.1 (2017-03), pp. 103–113. DOI: 10.13005/ojcst/10.01.14. URL: https://doi.org/10.13005/ojcst/10.01.14 (cit. on p. 22).

[52] R. Srisha and A. Khan. "Morphological Operations for Image Processing : Understanding and its Applications". In: 2013-12 (cit. on pp. 24–26).

[53] V. A. Mardiris and V. Chatzis. "A Configurable Design for Morphological Erosion and Dilation Operations in Image Processing using Quantum-dot Cellular Automata". In: *Journal of Engineering Science and Technology Review,* vol.9.no.2, (2016-05), pp.25–30. DOI: 10.25103/jestr.092.05. URL: http://dx.doi.org/10.25103/jestr.092.05 (cit. on p. 25).

[54] P. K. Biswal and S. Banerjee. "A parallel approach for affine transform of 3D biomedical images". In: *2010 International Conference on Electronics and Information Engineering*. Vol. vol.1, IEEE, 2010-08, pp.329–332. DOI: 10.1109/iceie.2010.5559864. URL: https://doi.org/10.1109/iceie.2010.5559864 (cit. on pp. 26, 27).

[55] D. Forsberg et al. "Model-based registration for assessment of spinal deformities in idiopathic scoliosis". In: *Physics in Medicine and Biology,* 59,2. (2013-12), pp.311–326. DOI: 10.1088/0031-9155/59/2/311. URL: https://doi.org/10.1088/0031-9155/59/2/311 (cit. on p. 26).

[56] A. Kaushik, P. C. Mathpal, and V. Sharma. "Edge Detection and Level Set Active Contour Model for the Segmentation of Cavity Present in Dental X-Ray Images". In: *International Journal of Computer Applications* vol.96,no.9, (2014-06), pp.24–29. DOI: 10.5120/16822-6576. URL: https://doi.org/10.5120/16822-6576 (cit. on p. 27).

[57] A. Kundu. "Local segmentation of biomedical images". In: *Computerized Medical Imaging and Graphics* 14.3 (1990-05), pp. 173–183. DOI: 10.1016/0895-6111(90)90057-i. URL: https://doi.org/10.1016/0895-6111(90)90057-i (cit. on p. 27).

[58] R. Hemalatha et al. "Active Contour Based Segmentation Techniques for Medical Image Analysis". In: *Medical and Biological Image Analysis,* InTech, 2018-07. Chap. 2. DOI: 10.5772/intechopen.74576. URL: https://doi.org/10.5772/intechopen.74576 (cit. on pp. 28–32).

[59] A. Histace et al. "Statistical region based active contour using a fractional entropy descriptor: Application to nuclei cell segmentation in confocal microscopy images". In: *Annals of The British Machine Vision Association* 2013 (2013-04), pp. 1–15. URL: http://www.bmva.org/annals/2013/2013-0005.pdf (cit. on p. 29).

[60] C. Xu and J. Prince. "Gradient vector flow: a new external force for snakes". In: *Proceedings of IEEE Computer Society Conference on Computer Vision and Pattern Recognition*. IEEE Comput. Soc. DOI: 10.1109/cvpr.1997.609299. URL: https://doi.org/10.1109/cvpr.1997.609299 (cit. on pp. 30, 33).

[61] V. Caselles, R. Kimmel, and G. Sapiro. "Geodesic Active Contours". In: *International Journal of Computer Vision*, vol.22.no.1 (1997-02), pp.61–79. DOI: 10.1023/a:1007979827043. URL: https://doi.org/10.1023/a:1007979827043 (cit. on pp. 30, 33).

[62] P. Marquez-Neila, L. Baumela, and L. Alvarez. "A Morphological Approach to Curvature-Based Evolution of Curves and Surfaces". In: *IEEE Transactions on Pattern Analysis and Machine Intelligence* vol.36,no.1, (2014-01), pp.2–17. DOI: 10.1109/tpami.2013.106. URL: https://doi.org/10.1109/tpami.2013.106 (cit. on p. 30).

[63] L. D. Cohen. "On active contour models and balloons". In: *CVGIP: Image Understanding* 53.2 (1991-03), pp. 211–218. DOI: 10.1016/1049-9660(91)90028-n. URL: https://doi.org/10.1016/1049-9660(91)90028-n (cit. on p. 30).

[64] A. Chopra and B. R. Dandu. "A Comprehensive Active Contour Model". In: *International Journal of Computer Applications* 49.13 (2012-07), pp. 35–39. DOI: 10.5120/7689-1005. URL: https://doi.org/10.5120/7689-1005 (cit. on pp. 31–33).

[65] M. Ciecholewski. "An edge-based active contour model using an inflation/deflation force with a damping coefficient". In: *Expert Systems with Applications* 44 (2016-02), pp. 22–36. DOI: 10.1016/j.eswa.2015.09.013. URL: https://doi.org/10.1016/j.eswa.2015.09.013 (cit. on p. 31).

[66] L. Alvarez et al. "Morphological snakes". In: *2010 IEEE Computer Society Conference on Computer Vision and Pattern Recognition*, IEEE, 2010-06, pp. 2197–2202. DOI: 10.1109/cvpr.2010.5539900. URL: https://doi.org/10.1109/cvpr.2010.5539900 (cit. on pp. 34, 35, 37, 38).

[67] J. Ma et al. "A Characteristic Function-Based Algorithm for Geodesic Active Contours". In: *SIAM Journal on Imaging Sciences*, vol.14,no.3, (2021-01), pp.1184–1205. DOI: 10.1137/20m1382817. URL: https://doi.org/10.1137/20m1382817 (cit. on p. 34).

[68] M. E.-M. Zelmat. "Image Segmentation Using Active Contour Model and Level Set Method Applied to Detect Oil Spills". In: 2009 (cit. on p. 35).

[69] J. N. Mlyahilu et al. "Morphological geodesic active contour algorithm for the segmentation of the histogram-equalized welding bead image edges". In: *IET Image Processing*, vol.16,no.10, (2022-04), pp.2680–2696. DOI: 10.1049/ipr2.12517. URL: https://doi.org/10.1049/ipr2.125177 (cit. on p. 35).

[70] P. Marquez-Neila, L. Baumela, and L. Alvarez. "A Morphological Approach to Curvature-Based Evolution of Curves and Surfaces". In: *IEEE Transactions on Pattern Analysis and Machine Intelligence* 36,1, (2014-01), pp.2–17. DOI: 10.1109/tpami.2013.106. URL: https://doi.org/10.1109/tpami.2013.106 (cit. on p. 35).

[71] A. Vondráček. "Image Segmentation Using a Morphological Operator for Curvature-Driven Motion". In: (2018) (cit. on p. 36).

[72] A. G. Medeiros et al. "An Automatic Left Ventricle Segmentation on Echocardiogram Exams via Morphological Geodesic Active Contour with Adaptive External Energy". In: *Journal of Artificial Intelligence and Systems* vol.1,no.1, (2019-10), pp.77–95. DOI: 10.33969/ais.2019.11005. URL: https://doi.org/10.33969/ais.2019.11005 (cit. on p. 37).

[73] X.-X. Yin et al. "Automatic breast tissue segmentation in MRIs with morphology snake and deep denoiser training via extended Stein's unbiased risk estimator". In: *Health Information Science and Systems* 9,1, (2021-04), pp.16. DOI: 10.1007/s13755-021-00143-x. URL: https://doi.org/10.1007/s13755-021-00143-x (cit. on p. 37).

[74] M. Fouladivanda et al. "Morphological active contour driven by local and global intensity fitting for spinal cord segmentation from MR images". In: *Journal of Neuroscience Methods* vol.308 (2018-10), pp.116–128. DOI: 10.1016/j.jneumeth.2018.07.015. URL: https://doi.org/10.1016/j.jneumeth.2018.07.015 (cit. on p. 37).

[75] D. Karimi and S. E. Salcudean. "Reducing the Hausdorff Distance in Medical Image Segmentation With Convolutional Neural Networks". In: *IEEE Transactions on Medical Imaging* 39.2 (2020-02), pp. 499–513. DOI: 10.1109/tmi.2019.2930068. URL: https://doi.org/10.1109/tmi.2019.2930068 (cit. on pp. 38, 39).

[76] P. Cheng et al. "Automatic vertebrae localization and segmentation in CT with a two-stage Dense-U-Net". In: *Scientific Reports*, vol.11,no.1, (). DOI: 10.1038/s41598-021-01296-1. URL: https://doi.org/10.1038/s41598-021-01296-1 (cit. on p. 38).

[77] B. Naneria, G. Yeotikar, and A. Wadhwani. "Diffuse Idiopathic Skeletal Hyperostosis". In: Coithram Hospital Research Center, Indore, India. 2013-09 (cit. on p. 42).

[78] K. Matsumoto, H. Uei, and Y. Tokuhashi. "Progressive diffuse idiopathic spinal hyperostosis: a case report". In: *Journal of International Medical Research* 47,8, (2019-07), pp.3955–3962. DOI: 10.1177/0300060519861451. URL: https://doi.org/10.1177/0300060519861451 (cit. on pp. 43–45).

[79] S. van der Walt et al. "scikit-image: image processing in Python". In: *PeerJ* 2 (2014-06), pp.453. DOI: 10.7717/peerj.453. URL: https://doi.org/10.77172Fpeerj.453 (cit. on pp. 44, 45).

[80] J. VanderPlas. *Python Data Science Handbook*. Sebastopol, CA: O'Reilly Media, 2016-12 (cit. on p. 45).

[81] Y. Gong. "Decompose X-ray Images for Bone and Soft Tissue". In: *ArXiv*, vol.abs/2007.14510 (2020-07) (cit. on p. 55).

[82] K. C. Kim et al. "Automatic detection and segmentation of lumbar vertebra from X-ray images for compression fracture evaluation". In: (2019). arXiv: 1904.07624 [physics.med-ph] (cit. on p. 106).

[83] M. Resorlu et al. "Association between apparent diffusion coefficient and intervertebral disc degeneration in patients with ankylosing spondylitis". In: *International Journal of Clinical and Experimental Medicine* 8 (2015-01), pp. 1241–1246 (cit. on p. 108).

I

Dimensions of images

In Table I.1 is possible to find information about the size of each image used for evaluation of DISH.

Image	Size
Image 1	594x255
Image 2	586x387
Image 3	460x246
Image 4	618x292
Image 5	700x414

Table I.1: Dimensions of images used for DISH evaluation.

II

Annotations 1 and 2

In this Annex, it will be provided the annotations 1 and 2 for both images used for segmentation evaluation.

II.1 Image 6

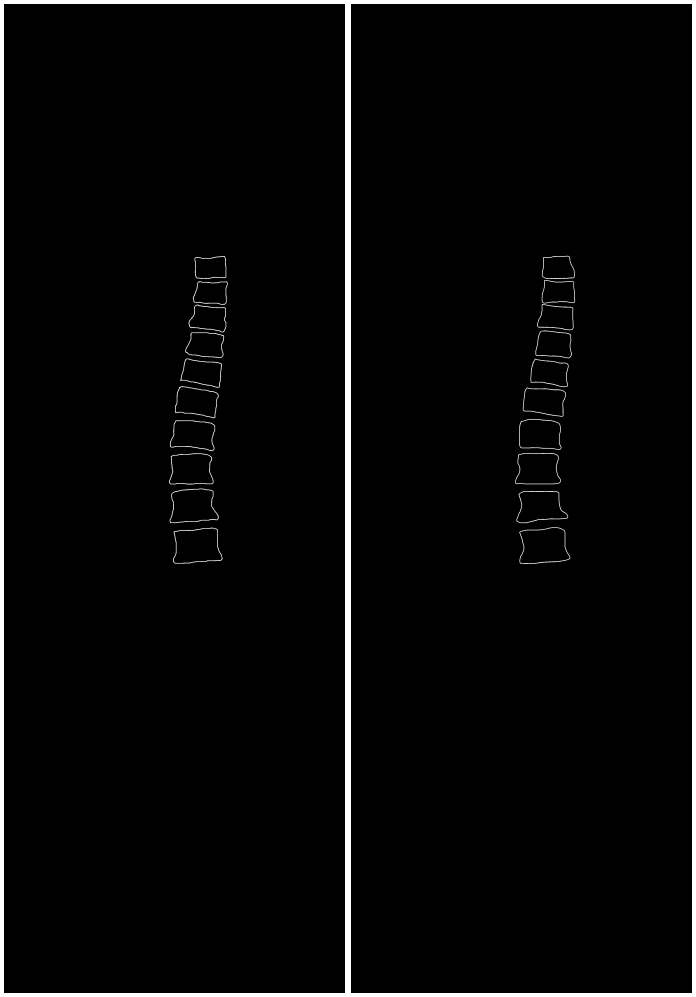

Figure II.1: Annotations 1 (Left) and 2 (Right) for Image 6.

II.2 Image 7

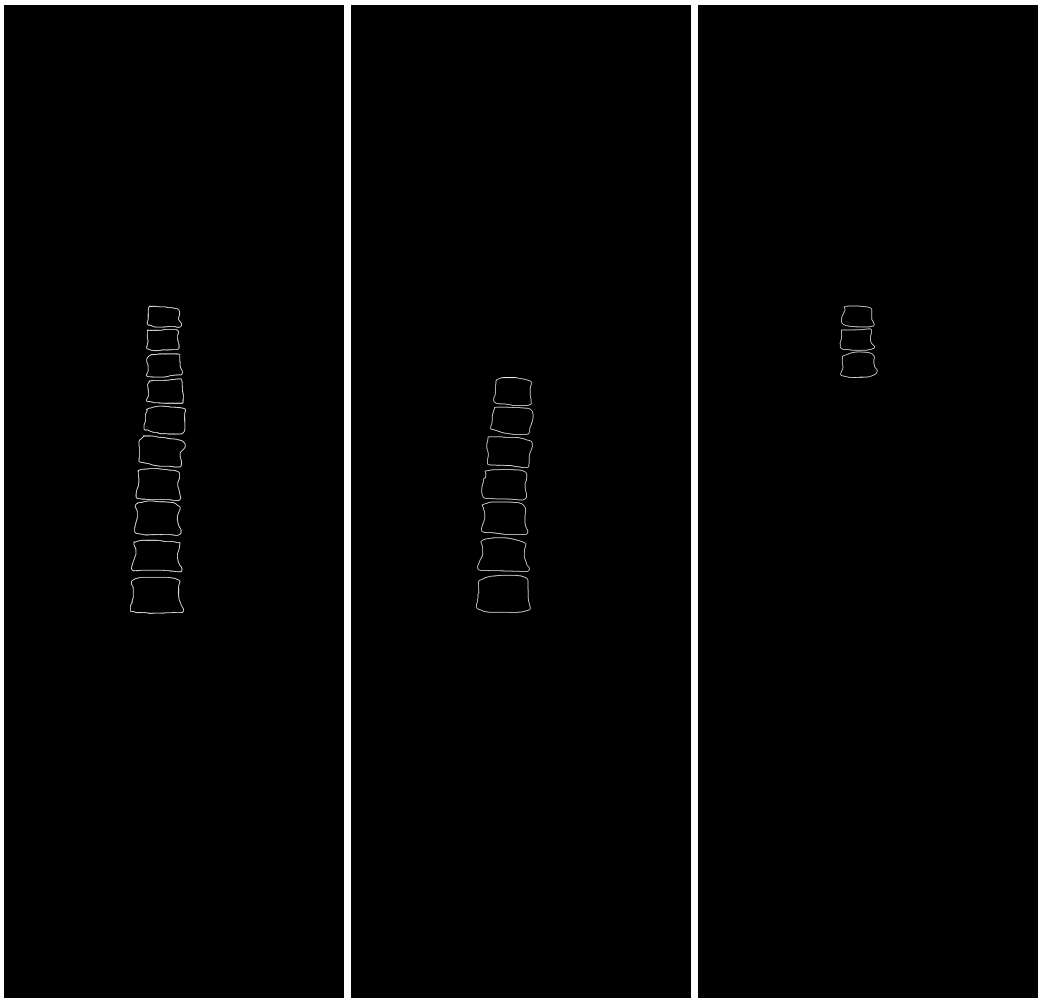

Figure II.2: Annotations 1 (Left) and 2 (Middle and Right) for Image 7.

III

Segmentation Results

In this Annex, the remaining segmentations from each image used in this work will be presented.

III.1 Image 1

In this section, the remainder of segmentations for Image 1 are presented.

III.1.0.1 T11 vertebra

The initial-level set used for the segmentation of the T11 from Image 1 and the concomitant segmentation are represented in Figure III.1.

Figure III.2 displays the corners of vertebra T11 and the correspondent histograms.

Figure III.3 displays all four corners' histograms, for visual comparison.

III.1.0.2 T12 vertebra

As done for the previous vertebra, all results. presented in Figures III.4 to III.6, for T12 vertebra are presented here.

The initial-level set used for the segmentation of the T12 vertebra and the concomitant segmentation are shown in Figure III.4.

Figure III.5 displays all the corners of vertebra T12 vertebra and the correspondent histograms.

Figure III.6 displays all four corners' histograms, for visual comparison.

III.1.0.3 L2 vertebra

As done for the previous vertebra, all results, presented in Figures III.7 to III.9, for L2 vertebra, are presented here.

The initial-level set used for the segmentation of the L2 vertebra from Image 1 and the concomitant segmentation are represented in Figure III.7.

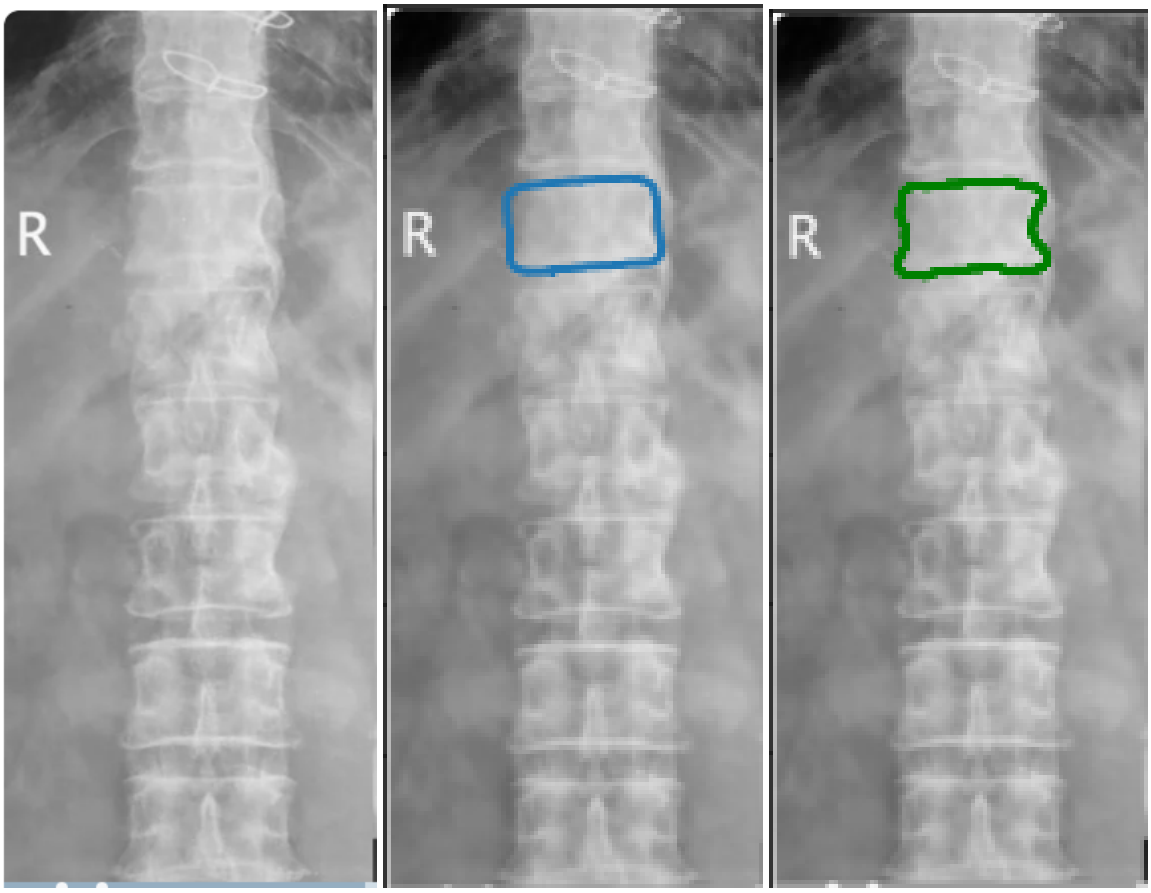

Figure III.1: Initial level-set and segmentation result for T11 from Image 1. Image on the left: Original image; Image on the middle: Initial level-set (blue curve) used for segmentation of that vertebra; Image on the right: Segmentation result (green) for the correspondent vertebra.

Figure III.8 displays all the corners of vertebra L2 vertebra and the correspondent histograms.

Figure III.9 displays all corners' histograms, for visual comparison.

III.2 Image 2

As done for Image 1, In this section, the remainder of segmentations for Image 2 are presented.

III.2.0.1 T7 vertebra

The initial-level set used for the segmentation of the T7 vertebra from Image 2 and the concomitant segmentation are represented in Figure III.10.

Figure III.11 displays the corners of vertebra T7 and the correspondent histograms.

Figure III.12 displays all corners' histograms, for visual comparison.

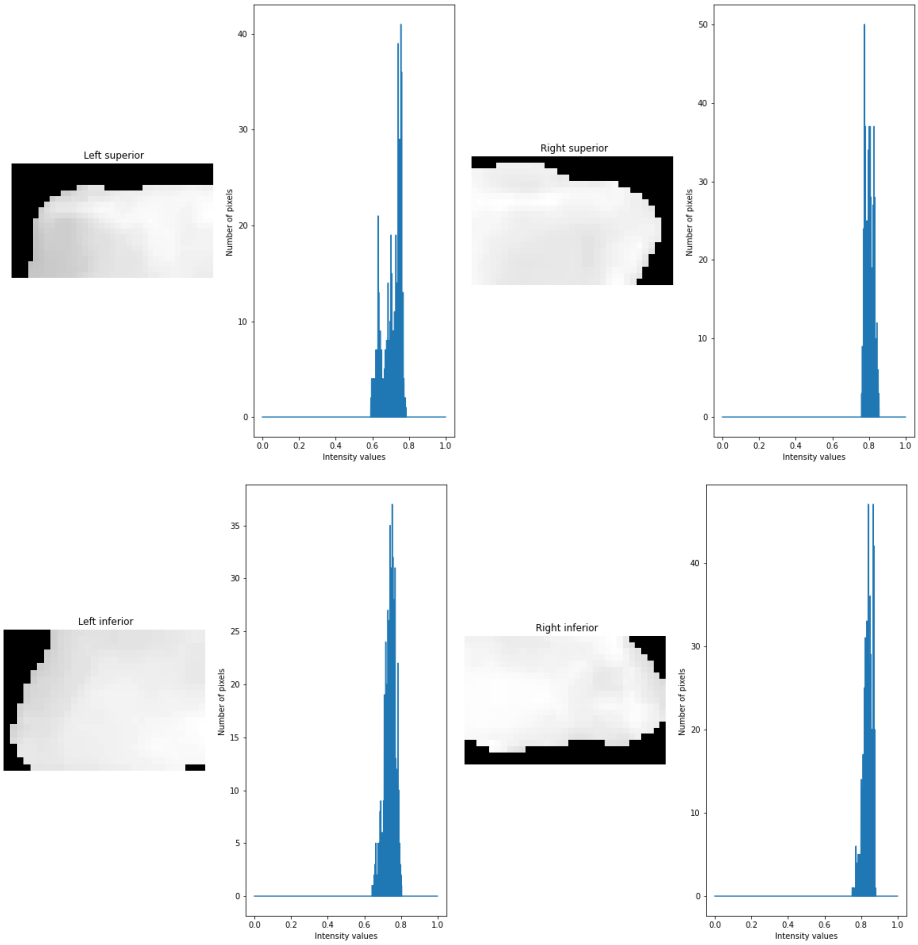

Figure III.2: Comparison of each corner and its histograms for T11 vertebra from Image 1.

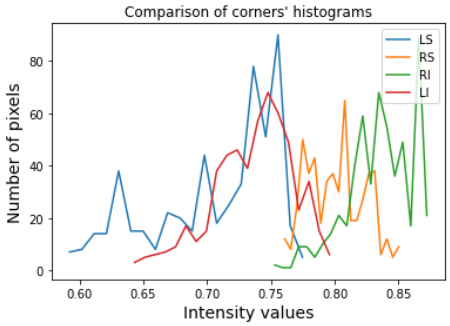

Figure III.3: Comparison of all corners' histograms for T11 from Image 1, showing the difference between right side (green and orange curves) and left side of vertebra (red and blue curves).

III.2.0.2 T10 vertebra

As done for the previous vertebra, all results, presented in Figures III.13 to III.15, for vertebra T10, are presented here.

The initial-level set used for the segmentation of the T10 vertebra from Image 2 and the concomitant segmentation are represented in Figure III.13.

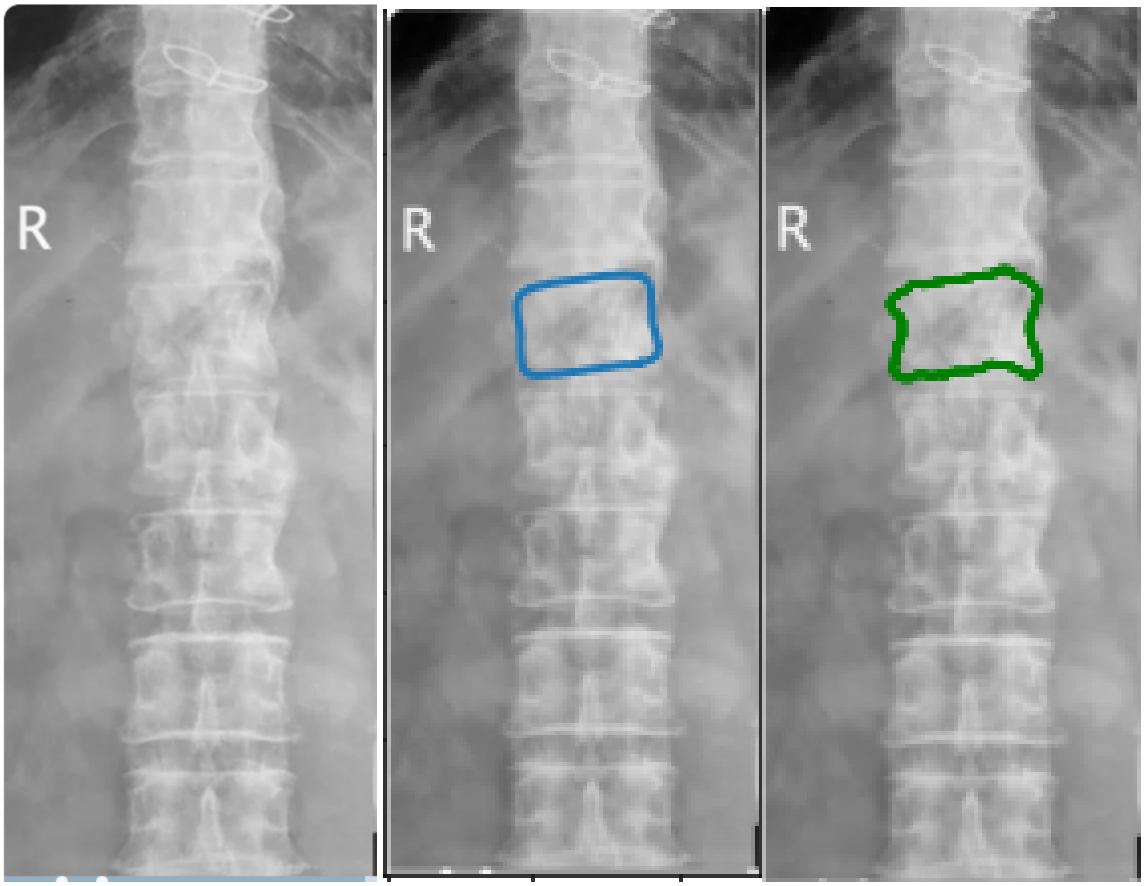

Figure III.4: Initial level-set and segmentation result for T12 from Image 1. Image on the left: Original image; Image on the middle: Initial level-set (blue curve) used for segmentation of that vertebra; Image on the right: Segmentation result (green) for the correspondent vertebra.

Figure III.14 displays the corners of vertebra T10 and the correspondent histograms.
Figure III.15 displays all corners' histograms, for visual comparison.

III.3 Image 3

III.3.0.1 T11 vertebra

The initial-level set used for the segmentation of the T11 vertebra and the concomitant segmentation are represented in Figure III.16.

Figure III.17 displays the corners of vertebra T11 and the correspondent histograms.
Figure III.18 displays all corners' histograms, for visual comparison.

III.3.0.2 L1 vertebra

As done for the previous vertebra, the results for the vertebra L1, from image 3, are presented here in Figures III.19 to III.21. The initial-level set used for the segmentation of the L1 vertebra and its concomitant segmentation are represented in Figure III.19.

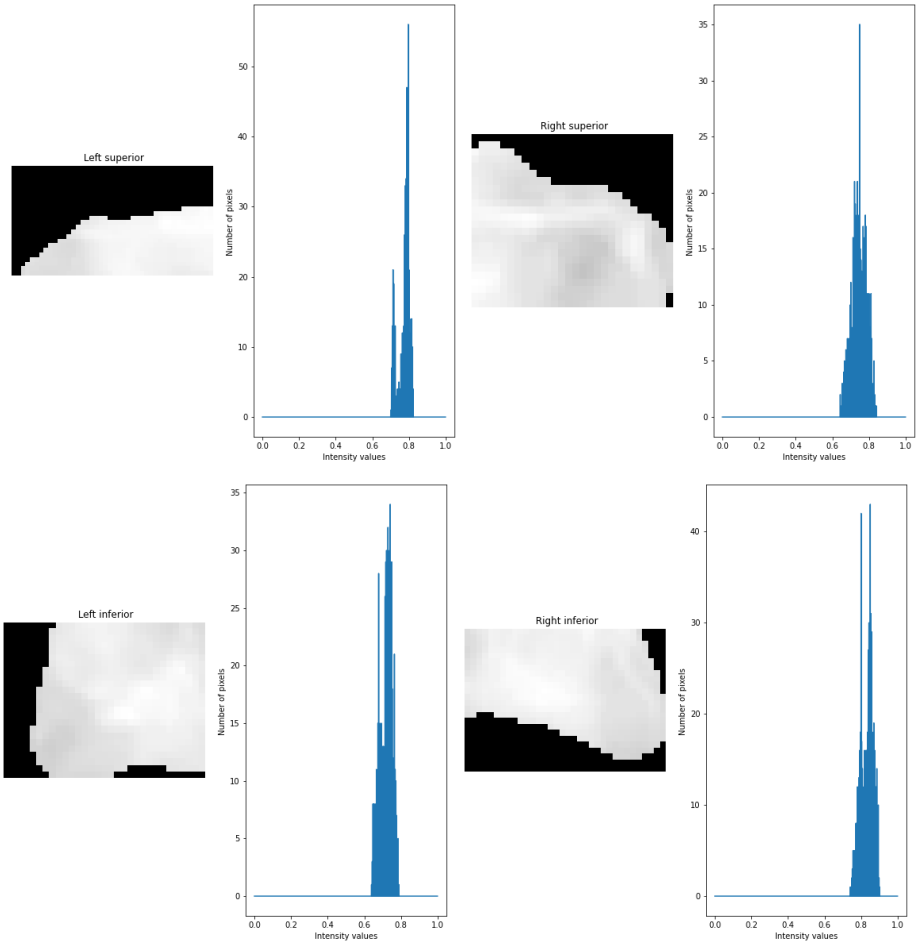

Figure III.5: Comparison of each corner and its histograms for the T12 vertebra from Image 1.

Figure III.20 displays the corners of vertebra L1 and the correspondent histograms.

Figure III.21 displays all corners' histograms, for visual comparison.

III.4 Image 4

III.4.0.1 T10 vertebra

The initial-level set used for the segmentation of the T10 vertebra from Image 4 and the concomitant segmentation are represented in Figure III.22.

Figure III.23 displays the corners of vertebra T10 and the correspondent histograms.

Figure III.24 displays all corners' histograms, for visual comparison.

III.4.0.2 T11 vertebra

As done for the previous vertebra, all results, presented in Figures III.25 to III.27, for vertebra T11 are presented here.

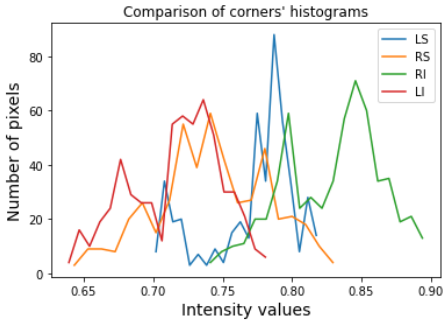

Figure III.6: Comparison of all corners' histograms for T12 from Image 1, showing the difference between right side (green and orange curves) and left side of vertebra (red and blue curves).

The initial-level set used for the segmentation of the T11 vertebra from Image 4 and the concomitant segmentation are represented in Figure III.25.

Figure III.26 displays the corners of vertebra T11 and the correspondent histograms.

Figure III.27 displays all corners' histograms, for visual comparison.

III.5 Image 5

In this section, the remainder of segmentations for Image 5 are presented.

III.5.0.1 T8 vertebra

The initial-level set used for the segmentation of the vertebra T8 from Image 5 and the concomitant segmentation are represented in Figure III.28.

Figure III.29 displays the corners of vertebra T8 and the correspondent histograms.

Figure III.30 displays all corners' histograms, for visual comparison.

III.5.0.2 T9 vertebra

As done for the previous vertebra, all results, presented in Figures III.31 to III.33, for vertebra T9 are presented here.

The initial-level set used for the segmentation of the vertebra T9 from Image 5 and the concomitant segmentation are represented in Figure III.31.

Figure III.32 displays the corners of vertebra T9 and the correspondent histograms.

Figure III.33 displays all corners' histograms, for visual comparison.

III.5.0.3 T6 vertebra

The initial-level set used for the segmentation of vertebra T6, from Image 5, and the concomitant segmentation are shown in Figure III.34.

Figure III.35 displays the corners of vertebra T6 and the correspondent histograms.

Figure III.36 displays the corners' histograms, for visual comparison.

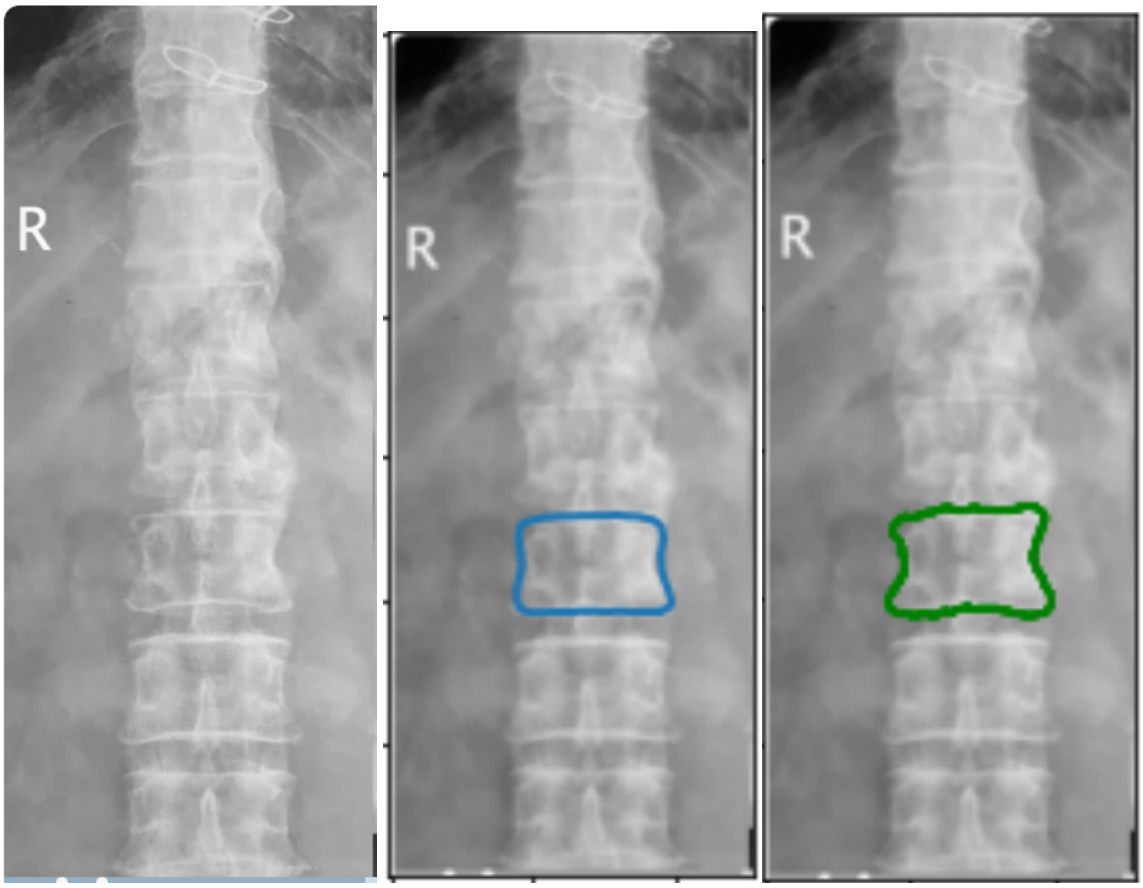

Figure III.7: Initial level-set and segmentation result for L2 from Image 1. Image on the left: Original image; Image on the middle: Initial level-set (blue curve) used for segmentation of that vertebra; Image on the right: Segmentation result (green) for the correspondent vertebra.

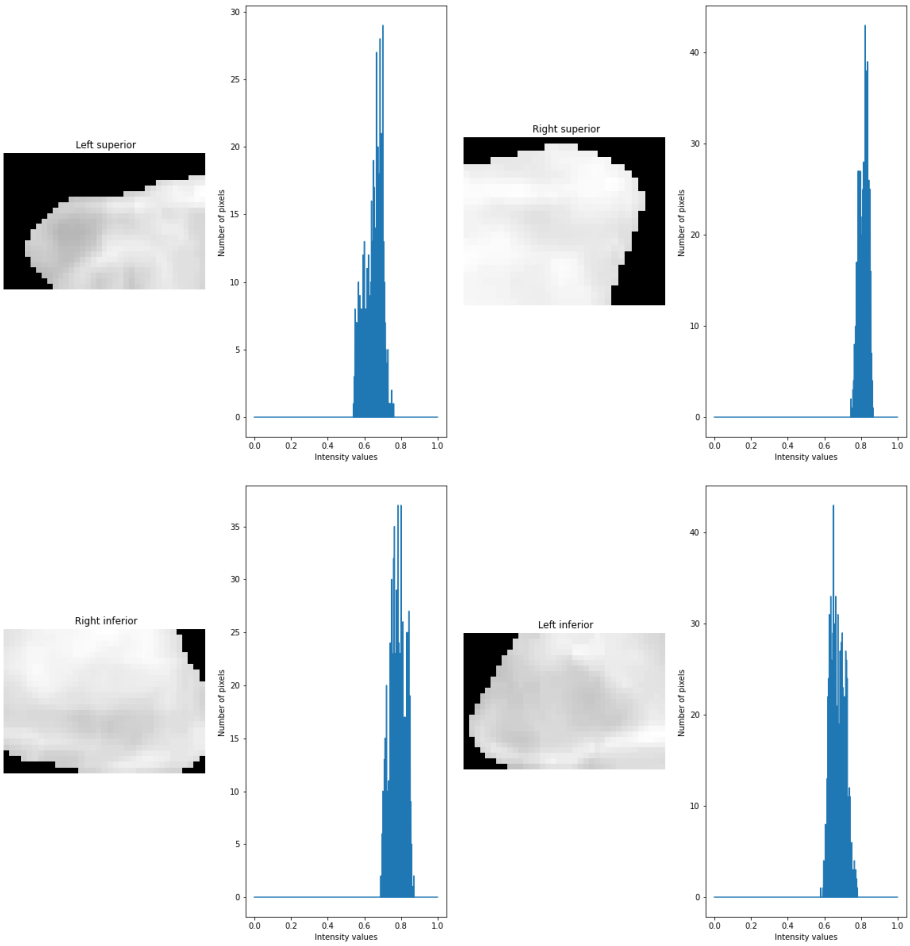

Figure III.8: Comparison of each corner and its histograms for the L2 vertebra from Image 1.

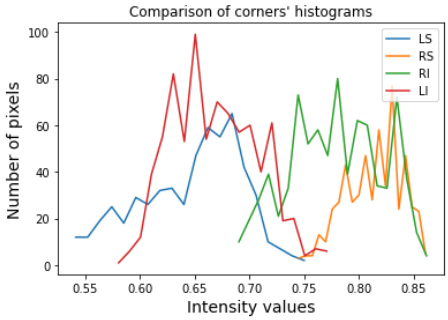

Figure III.9: Comparison of all corners' histograms for L2 from Image 1, showing the difference between right side (green and orange curves) and left side of vertebra (red and blue curves).

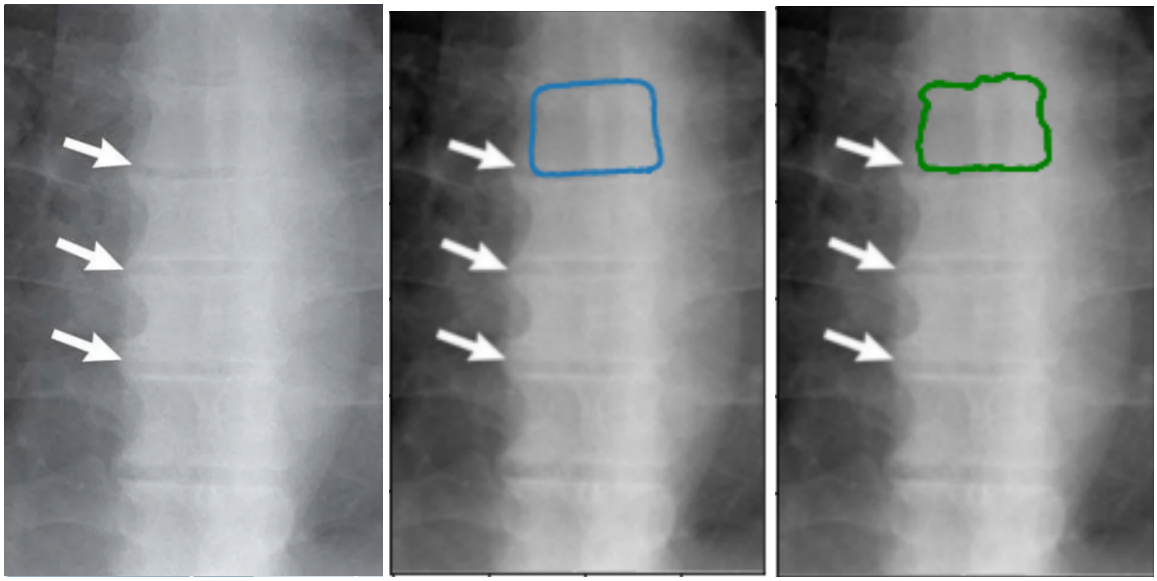

Figure III.10: Initial level-set and segmentation result for T7 from Image 2. Image on the left: Original image; Image on the middle: Initial level-set (blue curve) used for segmentation of that vertebra; Image on the right: Segmentation result (green) for the correspondent vertebra.

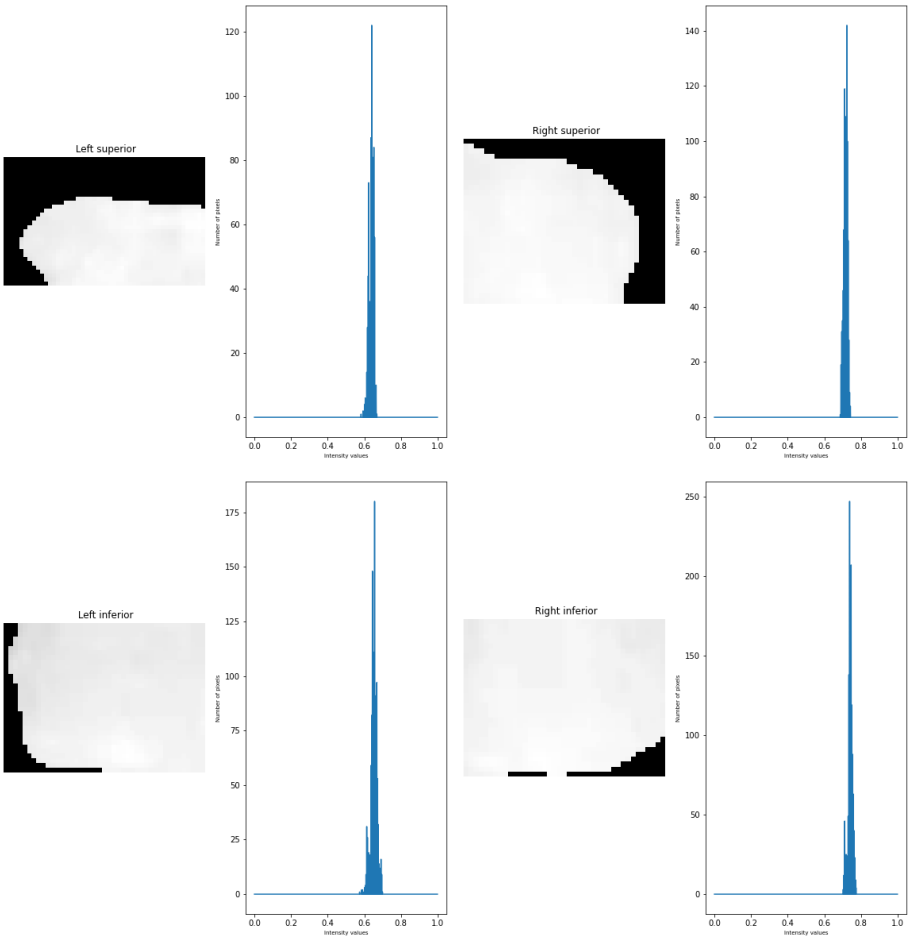

Figure III.11: Comparison of each corner and its histograms for the T7 vertebra from Image 2.

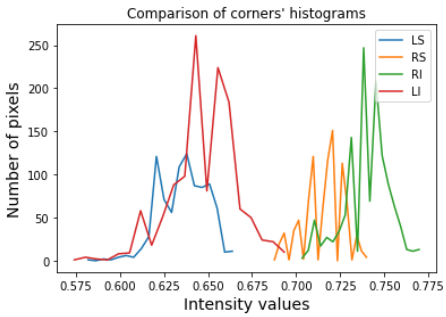

Figure III.12: Comparison of all corners' histograms for T7 from Image 2, showing the difference between right side (green and orange curves) and left side of vertebra (red and blue curves).

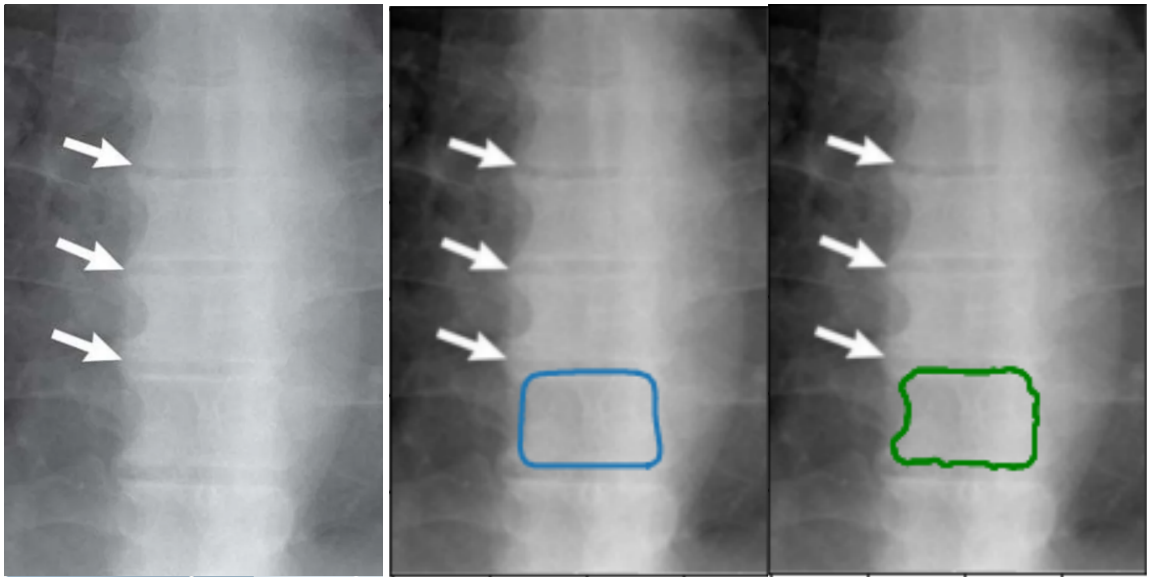

Figure III.13: Initial level-set and segmentation result for T10 from Image 2. Image on the left: Original image; Image on the middle: Initial level-set (blue curve) used for segmentation of that vertebra; Image on the right: Segmentation result (green) for the correspondent vertebra.

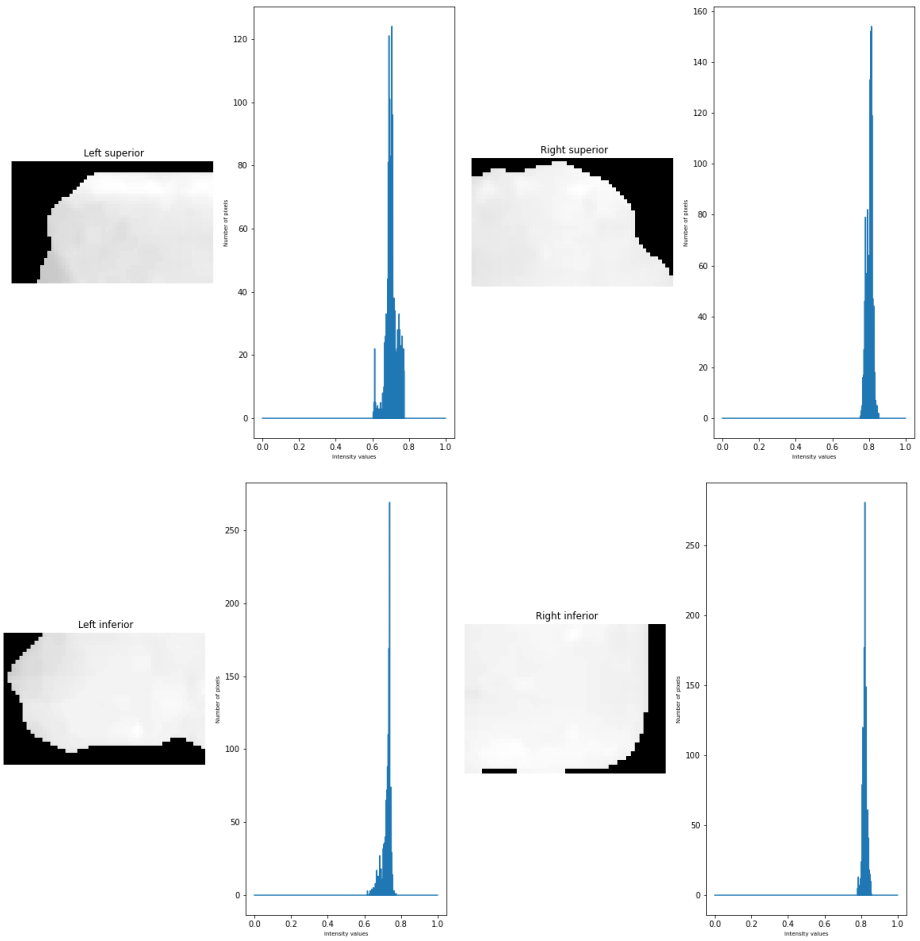

Figure III.14: Comparison of each corner and its histograms for the T10 vertebra from Image 2.

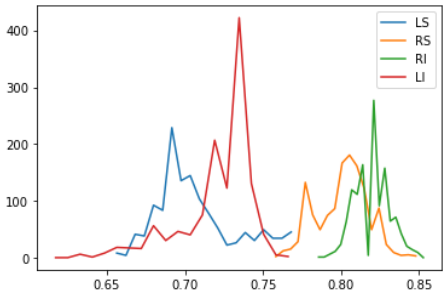

Figure III.15: Comparison of all corners' histograms for T10 from Image 2, showing the difference between right side (green and orange curves) and left side of vertebra (red and blue curves).

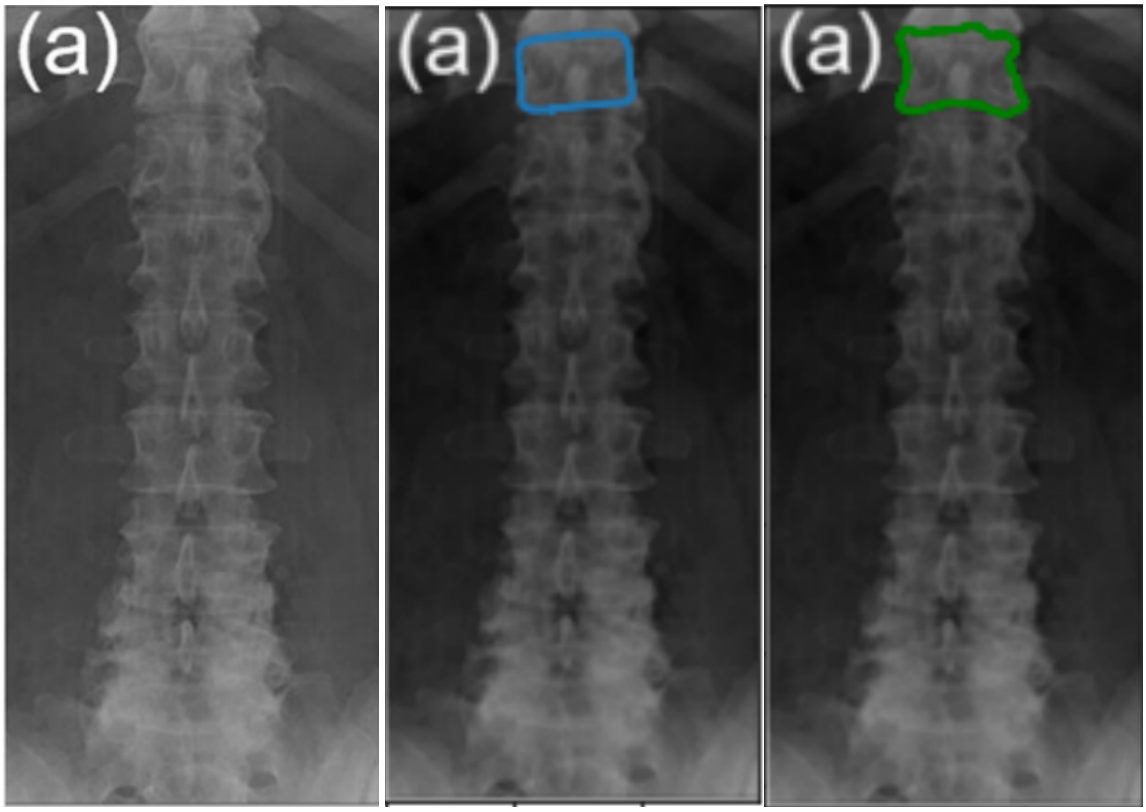

Figure III.16: Initial level-set and segmentation result for T11 from Image 3. Image on the left: Original image;Image on the middle: Initial level-set (blue curve) used for segmentation of that vertebra; Image on the right: Segmentation result (green) for the correspondent vertebra.

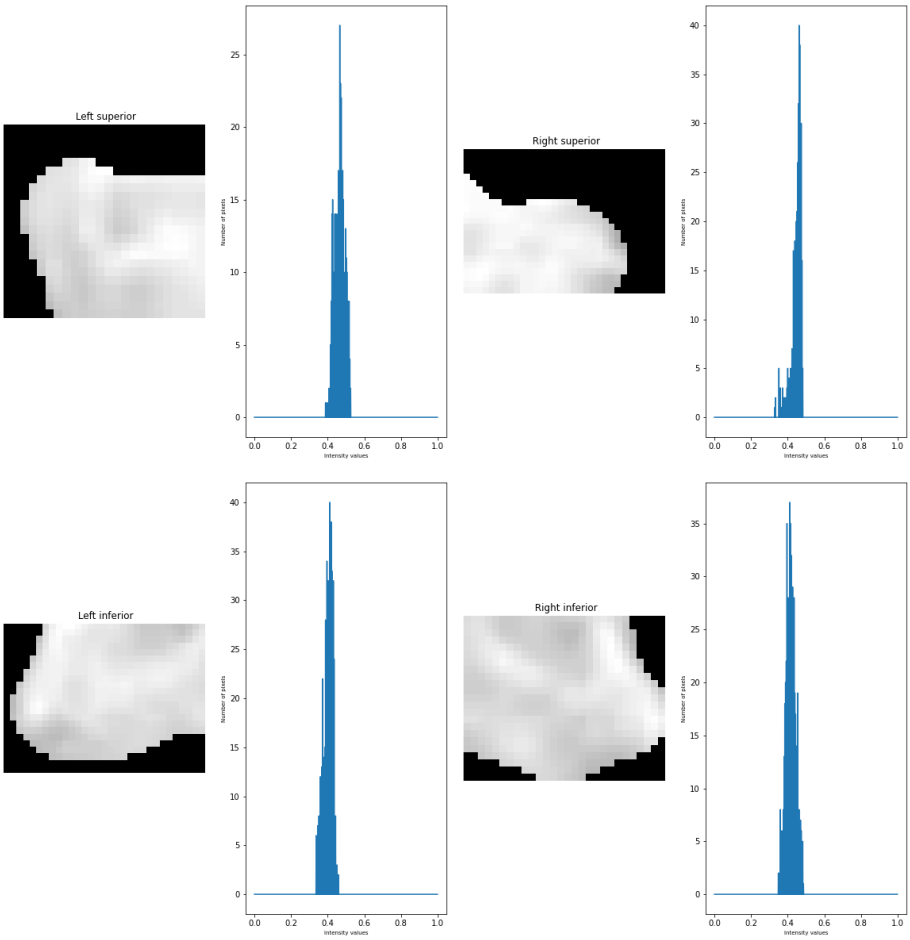

Figure III.17: Comparison of each corner and its histograms for the T11 vertebra from Image 3.

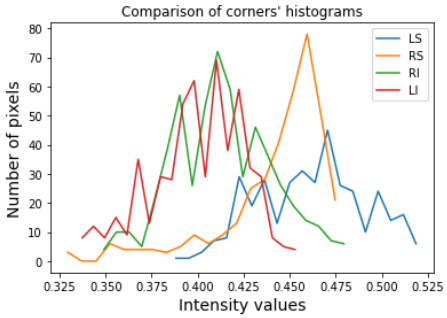

Figure III.18: Comparison of all corners' histograms for T11 from Image 3, showing the difference between right side (green and orange curves) and left side of vertebra (red and blue curves).

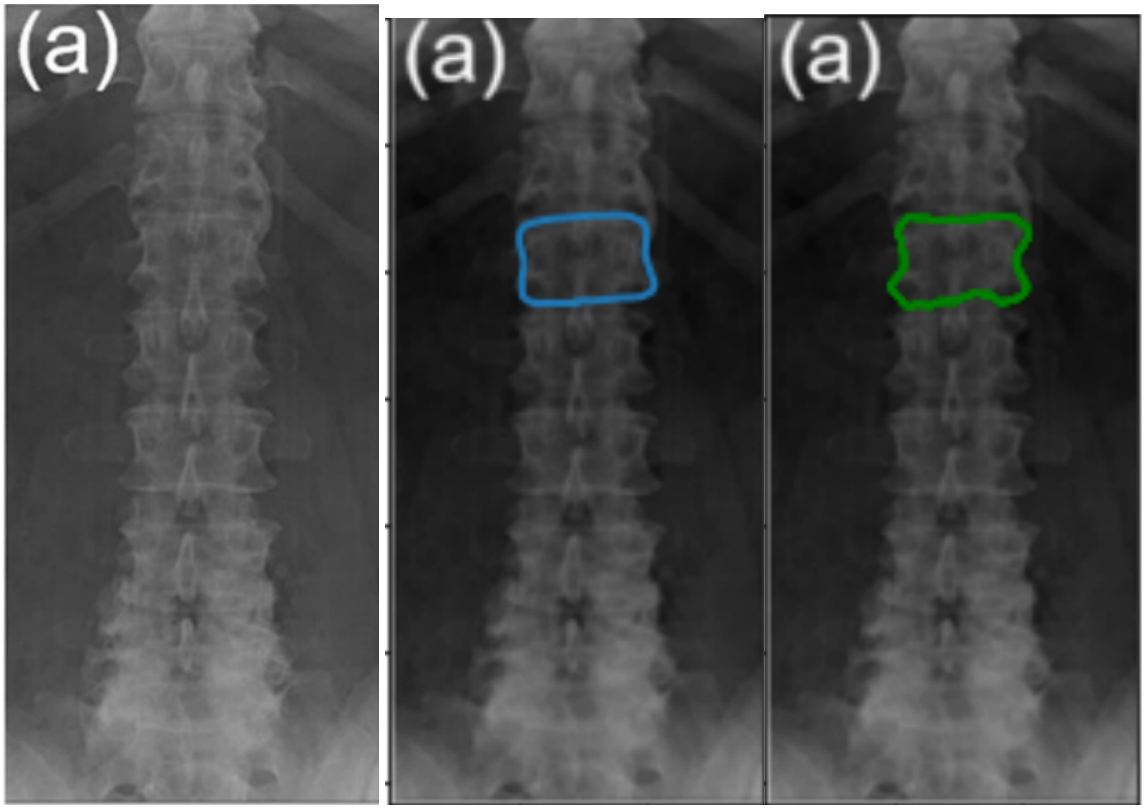

Figure III.19: Initial level-set and segmentation result for L1 from Image 3. Image on the left: Original image; Image on the middle: Initial level-set (blue curve) used for segmentation of that vertebra; Image on the right: Segmentation result (green) for the correspondent vertebra.

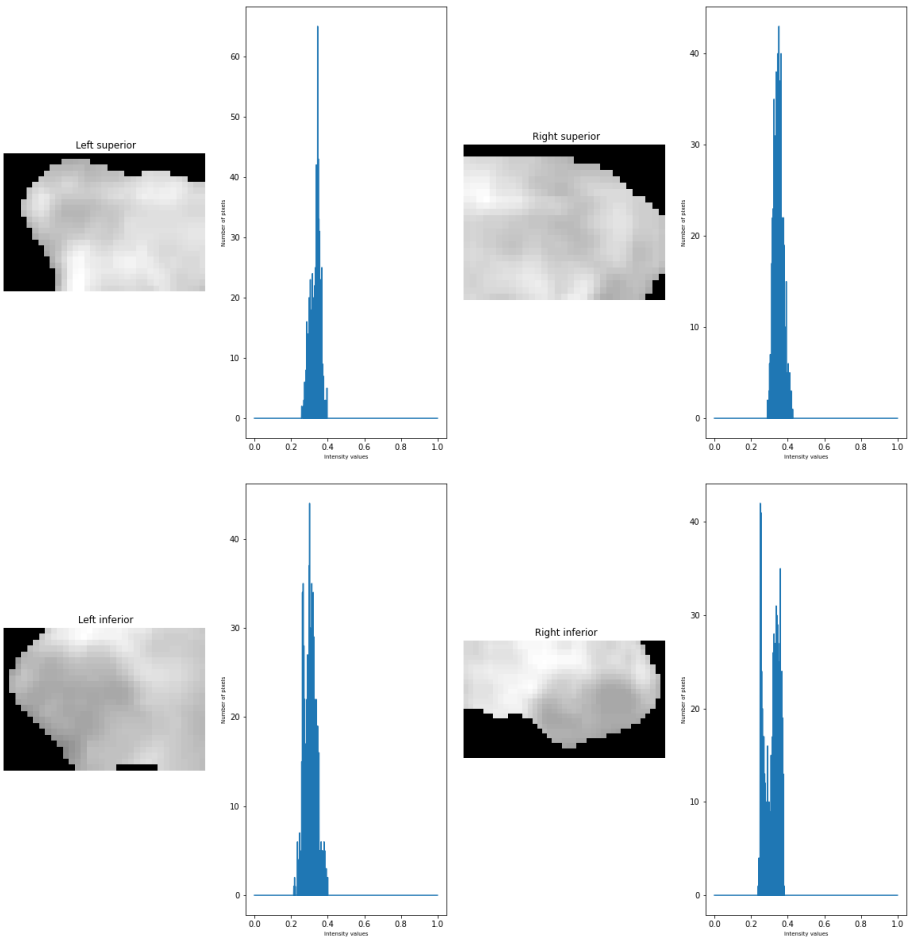

Figure III.20: Comparison of each corner and its histograms for the vertebra L1 from Image 3.

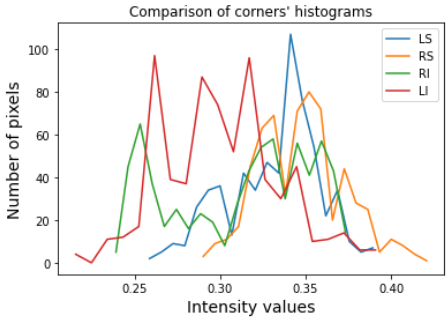

Figure III.21: Comparison of all corners' histograms for L1 from Image 3, showing the difference between right side (green and orange curves) and left side of vertebra (red and blue curves).

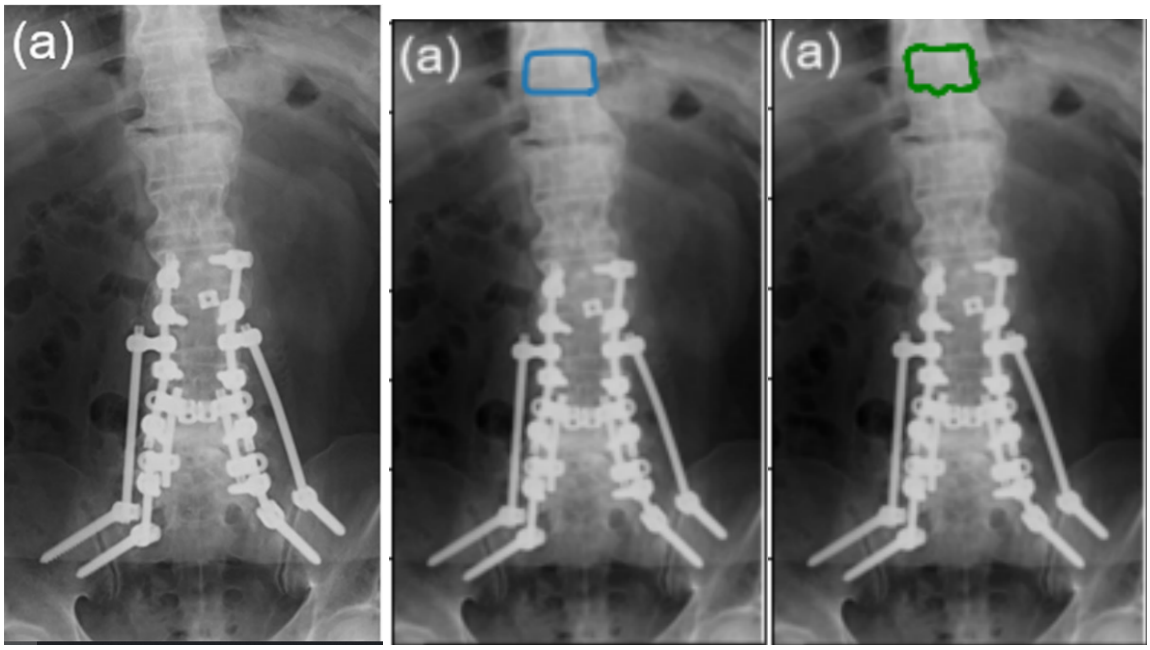

Figure III.22: Initial level-set and segmentation result for T10 from Image 4. Image on the left: Original image; Image on the middle: Initial level-set(blue curve) used for segmentation of that vertebra; Image on the right: Segmentation result (green) for the correspondent vertebra.

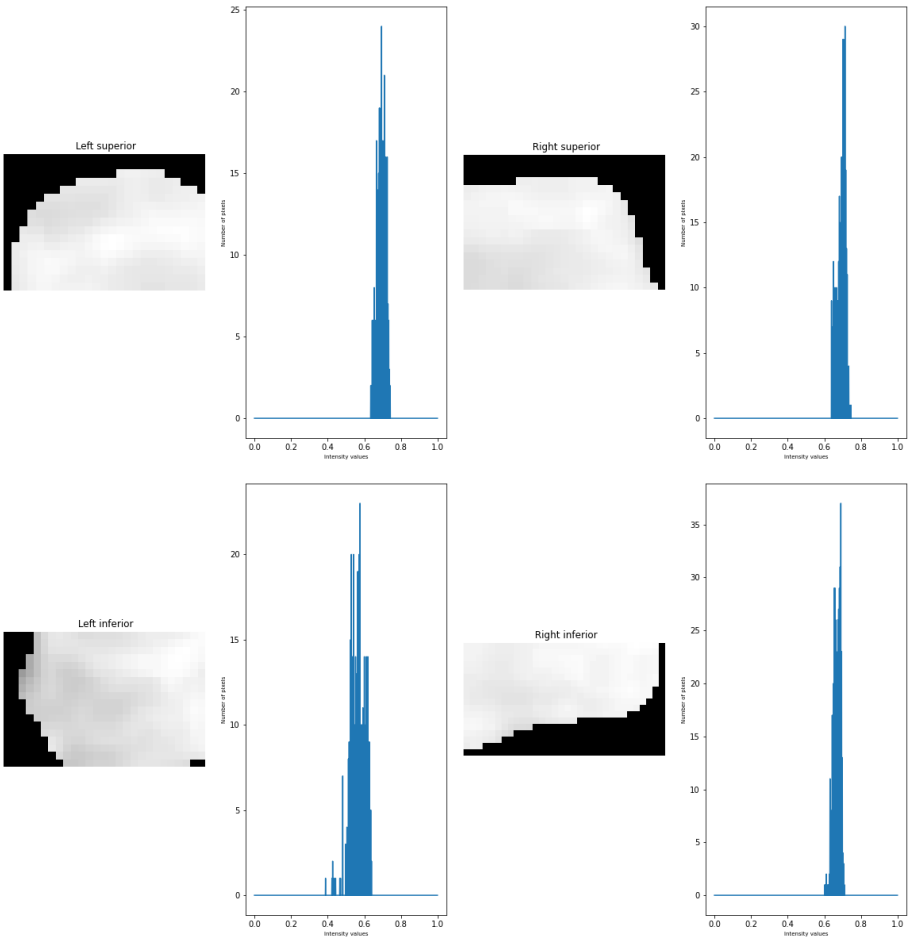

Figure III.23: Comparison of each corner and its histograms for the T10 vertebra from Image 4.

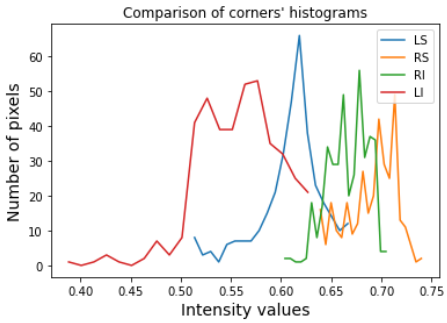

Figure III.24: Comparison of all corners' histograms for T10 from Image 4, showing the difference between right side (green and orange curves) and left side of vertebra (red and blue curves).

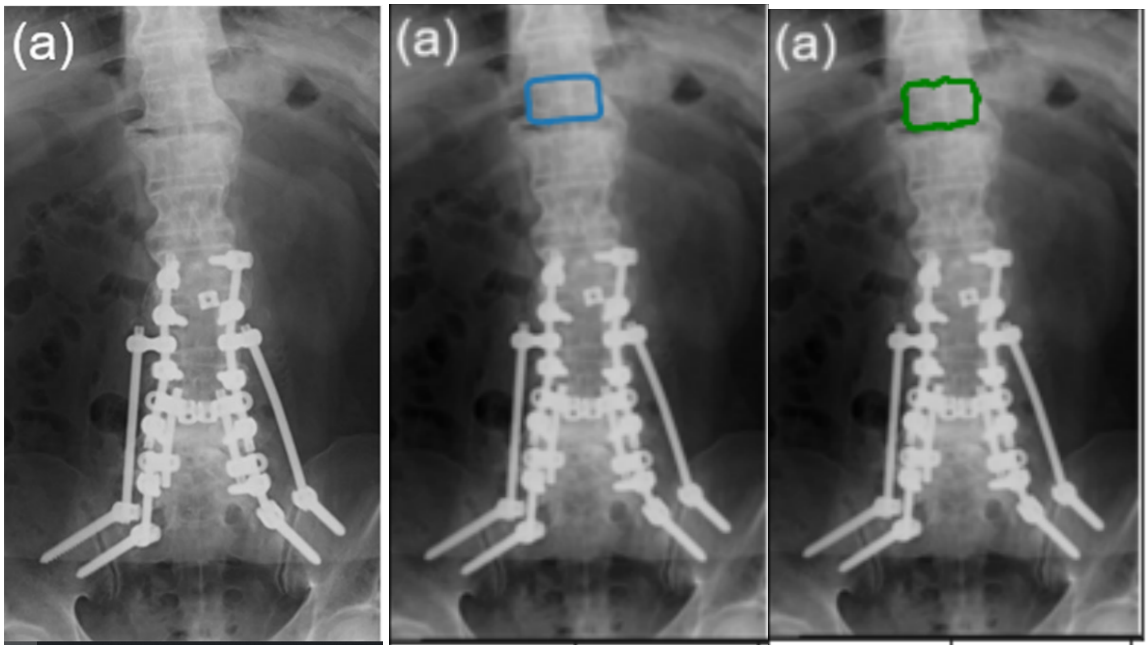

Figure III.25: Initial level-set and segmentation result for T11 from Image 4. Image on the left: Original image;Image on the middle: Initial level-set (blue curve) used for segmentation of that vertebra; Image on the right: Segmentation result (green) for the correspondent vertebra.

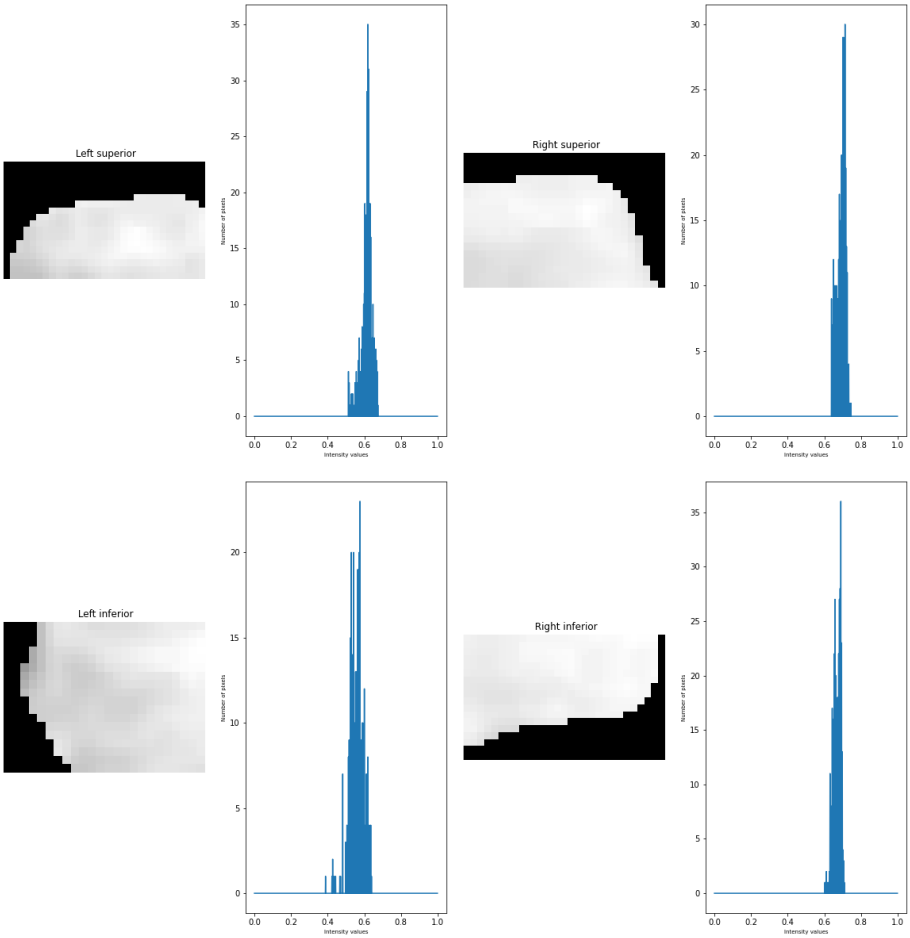

Figure III.26: Comparison of each corner and its histograms for the T11 vertebra from Image 4.

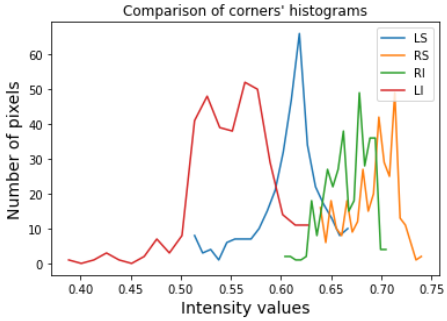

Figure III.27: Comparison of all corners' histograms for T11 from Image 4, showing the difference between right side (green and orange curves) and left side of vertebra (red and blue curves).

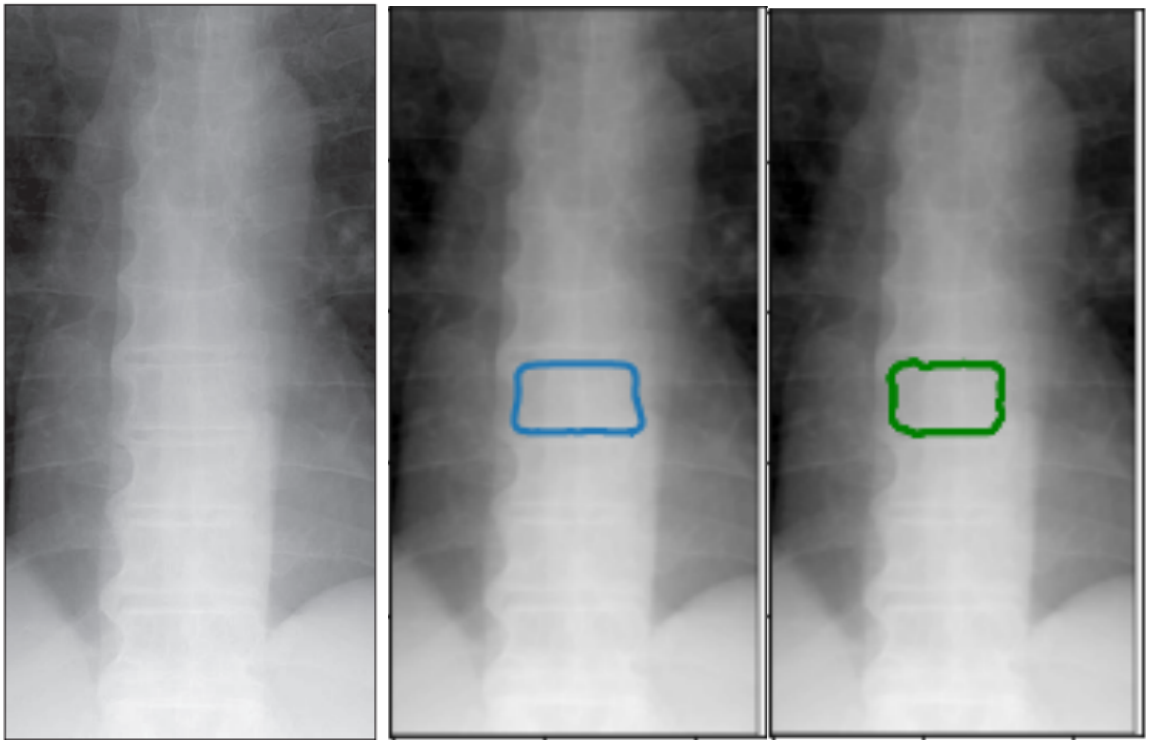

Figure III.28: Initial level-set and segmentation result for T8 from Image 5. Image on the left: Original image;Image on the middle: Initial level-set (blue curve) used for segmentation of that vertebra; Image on the right: Segmentation result (green) for the correspondent vertebra.

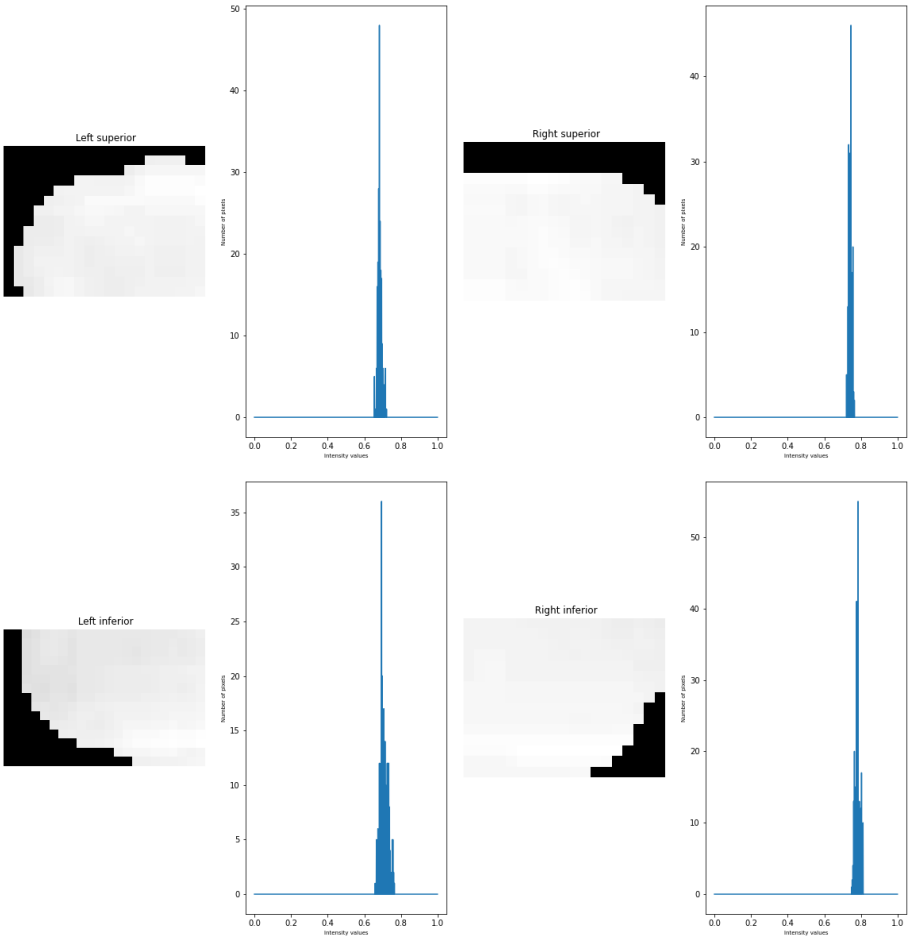

Figure III.29: Comparison of each corner and its histograms for the T8 vertebra from Image 5.

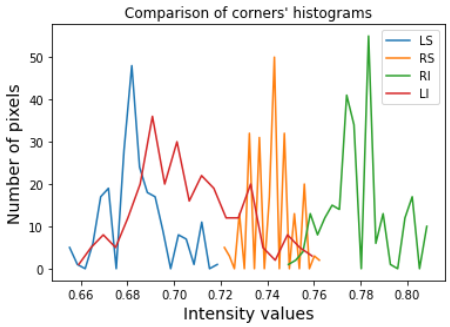

Figure III.30: Comparison of all corners' histograms for T8 from Image 5, showing the difference between right side (green and orange curves) and left side of vertebra (red and blue curves).

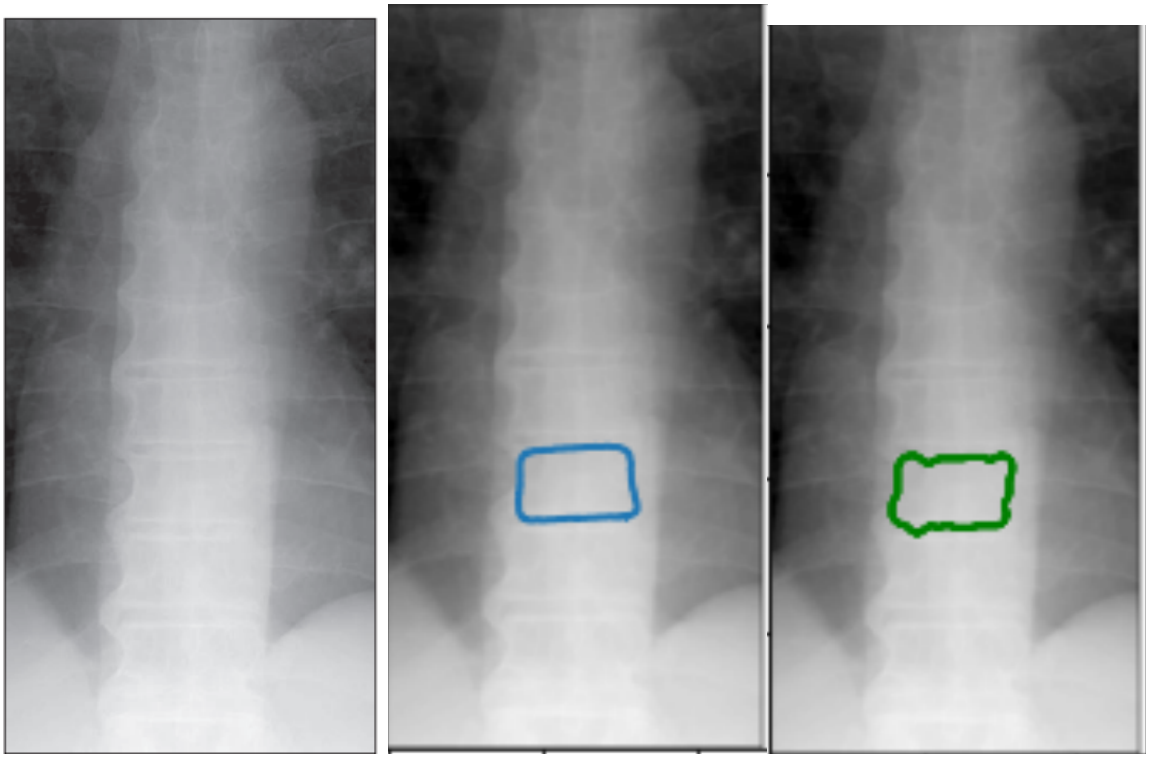

Figure III.31: Initial level-set and segmentation result for T9 from Image 5. Image on the left: Original image;Image on the middle: Initial level-set (blue curve) used for segmentation of that vertebra; Image on the right: Segmentation result (green) for the correspondent vertebra.

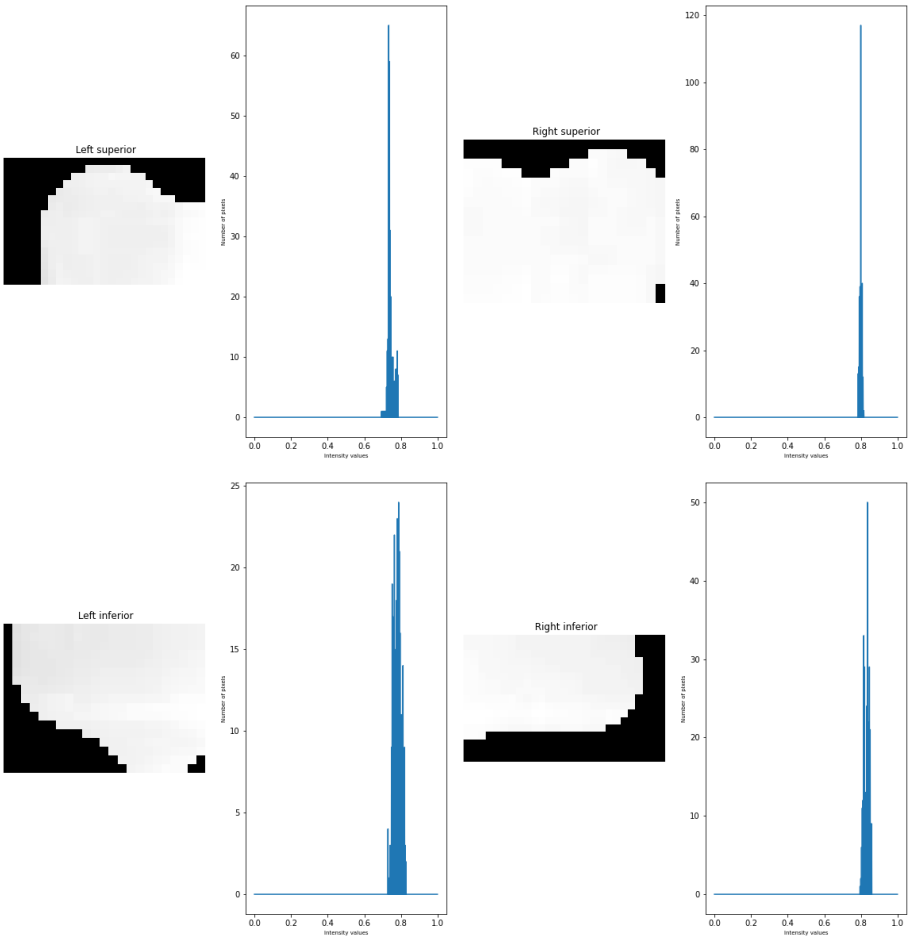

Figure III.32: Comparison of each corner and its histograms for the T9 from Image 5.

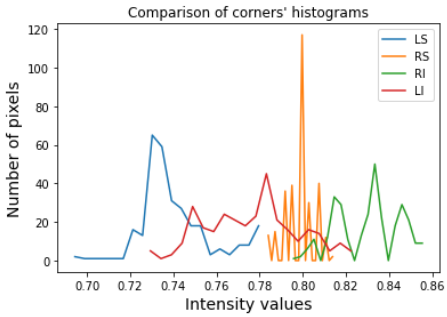

Figure III.33: Comparison of all corners' histograms for T9 from Image 5, showing the difference between right side (green and orange curves) and left side of vertebra (red and blue curves).

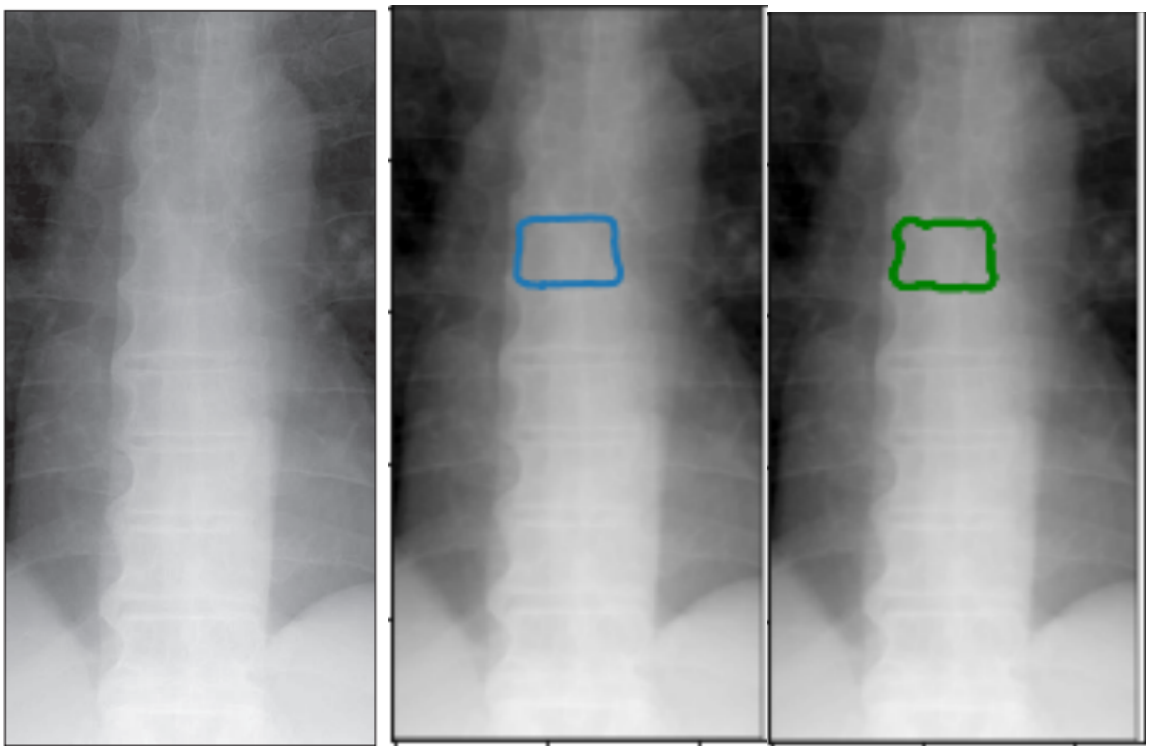

Figure III.34: Initial level-set and segmentation result for L6 from Image 5. Image on the left: Initial level-set (blue curve) used for segmentation of that vertebra; Image on the right: Segmentation result (green) for the correspondent vertebra.

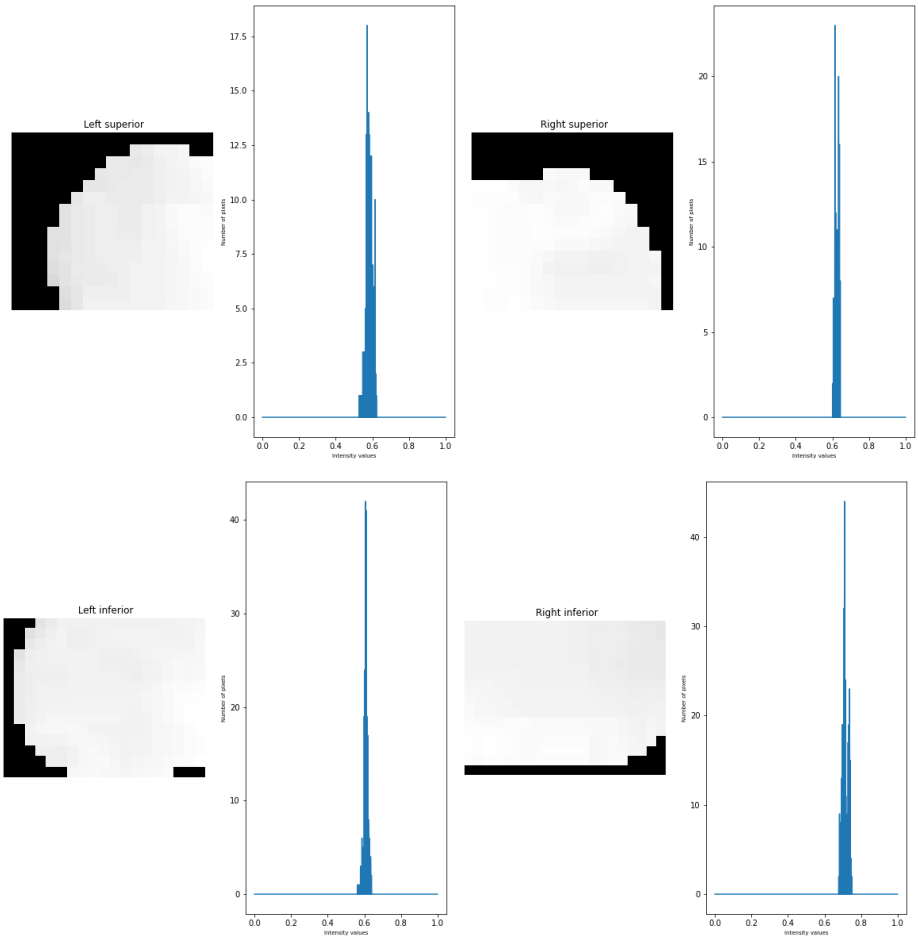

Figure III.35: Comparison of each corner and its histograms for the T6 vertebra from Image 5.

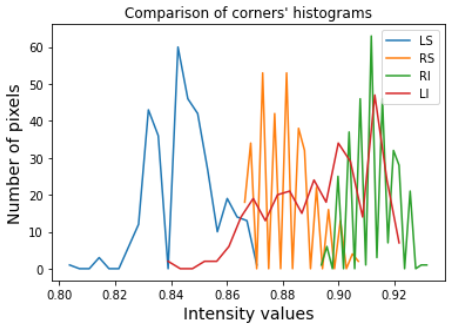

Figure III.36: Comparison of all corners' histograms for T6 from Image 5, showing the difference between right side (green and orange curves) and left side of vertebra (red and blue curves).

2022 Characterization of structural changes in spinal vertebrae based on Perturbations to an ac

Duarte Bernardo

NOVA SCHOOL OF
SCIENCE & TECHNOLOGY